

# Micromachined Tunable Devices Based on Silicon Integrated $\text{Ba}_x\text{Sr}_{1-x}\text{TiO}_3$ Thin Films: Concepts, Fabrication and Characterization

THÈSE N° 4284 (2009)

PRÉSENTÉE LE 6 FÉVRIER 2009

À LA FACULTE SCIENCES ET TECHNIQUES DE L'INGÉNIEUR

LABORATOIRE DE CÉRAMIQUE

PROGRAMME DOCTORAL EN SCIENCE ET GÉNIE DES MATÉRIAUX

ÉCOLE POLYTECHNIQUE FÉDÉRALE DE LAUSANNE

POUR L'OBTENTION DU GRADE DE DOCTEUR ÈS SCIENCES

PAR

Andreas NÖTH

acceptée sur proposition du jury:

Prof. N. Baluc, présidente du jury

Prof. N. Setter, Dr A. Tagantsev, directeurs de thèse

Prof. S. Gevorgian, rapporteur

Prof. A. Skrivervik Favre, rapporteur

Prof. T. Yamada, rapporteur



ÉCOLE POLYTECHNIQUE  
FÉDÉRALE DE LAUSANNE

Suisse  
2009



## Acknowledgements

I would like to take the opportunity to thank the many people who supported me in whatever way during my PhD research.

I am deeply grateful to my thesis director, Prof. Nava Setter, for offering me a PhD position in the Ceramics Laboratory, where I could carry out my research work in a well-equipped laboratory and in a stimulating environment. I appreciate her support, encouragement and advice during all these years.

I am deeply thankful to my thesis co-director, Dr. Alexander Tagantsev, for all his support during my thesis, for being an excellent and patient teacher explaining complicated issues in an easy way, for all the inspiring, fruitful and instructive discussions, and all his efforts in reading and correcting my articles, project reports, and my thesis manuscript.

I would like to thank my supervisor, Prof. Tomoaki Yamada, for teaching me about thin film processing and other experimental techniques, for guiding me during my PhD thesis, for being a constant source of inspiration, for all his support, ideas, suggestions, and his interest in my work.

I would like to thank the jury members for my thesis defense: Prof. N. Baluc, Prof. S. Gevorgian, and Prof. A. Skrivervik.

I am grateful to Prof. Paul Muralt and Prof. Dragan Damjanovic for all useful discussions and suggestions for my thesis. I want to thank Dr. Vladimir Sherman for teaching me the electrical characterization of devices (especially at high frequencies) and this support for the experimental work. Thanks to Claudia Cancellieri for the deposition of the YBCO films by off-axis PLD. I would like to thank Dr. Cosmin Sandu and Dr. Zhanbing He for the TEM investigations. I am thankful to Dominik Borner and Carl Lindberg for doing an excellent job during their semester projects with me. Many thanks to Nicolas Leiser (EPFL-IPEQ) and the staff of CMI (Center of Micro/Nanotechnology) and CIME (Interdisciplinary Centre of Electron Microscopy) for training, support and advice.

I would like to acknowledge the financial support by the EU-Project NANOS-TAR and the good and instructive collaboration with all the project partners.

I would like to thank the LC's "technician group", Lino Olivetta, Jacques Castano and Julien Maret, for all their support, assistance, etc. Particulièrement, un grand merci à Lino pour sa patience de réparer l'alpha-step plusieurs fois et pour les moments bien rigolos. I am thankful to our office secretaries, Eva Favre and Yuko Kagata Spitteler, for the help concerning administrative issues and for the friendly atmosphere. I would like to thank the staff at the workshop of the Materials Institute for the support and the quick fabrication of various parts.

I would like to express a very big thanks to my former and present officemates, Dr. Brahim Belgacem, Dr. Florian Calame, Dr. Scott Harada, Evgeny Milyutin and Monica Ivanowska for the nice atmosphere in and outside the office, their support during the thesis, the interesting – and fortunately not always scientific – discussions.

I would like to thank all former and present LC colleagues and friends: Dr. Roman Gysel, Dr. Guido Gerra, Dr. Samuel Rey-Mermet, Alvaro Artieda, Naama Klein, Janine Conde, Sebastian Riester, Dr. Sandrine Gentil, Dr. Guochu Deng, Dr. Lisa Malin, Dr. Yongli Wang, Dr. Matthew Davis, Dr. Evelyn Hollenstein, Christine Leroy, Dr. Viktor Porokhonsky, Dr. Igor Stolitchnov, Dr. Fabrice Martin, Maxim Gureev, Jin Li, Jin Wang, Dr. Dong Su, Yan Yan, Dr. Arsen Sukiasyan, ... Thank you all for the stimulating and instructive discussions and the nice atmosphere – not only at work.

Many thanks to all my friends, no matter where you are, for all the nice moments I shared with you.

I would like to thank Steffi for her love, support, patience, and understanding during these PhD years.

I would like to express my deep gratefulness to my family for all the love, support, confidence, and energy during all the years of my education and PhD research.



# Abstract

Thin Film Bulk Acoustic Wave Resonators (TFBARs) had been developed a decade ago and since then were implemented extensively in mobile communications devices. The “heart” of a TFBAR consists of a piezoelectric film that operates as an acousto-electric transducer, stabilizing the transmission at a given predetermined frequency. For reasons such as space economy in hand-held devices, it is of interest to make these TFBARs tunable, so that a single TFBAR is multi-band responsive. This thesis demonstrates for the first time electrically tunable, single-component TFBARs.

A theory describing the tuning behavior of dc bias induced acoustic resonances was developed. Then we made the hypothesis that dc bias induced piezoelectric  $\text{Ba}_x\text{Sr}_{1-x}\text{TiO}_3$  (BST) thin films – namely, paraelectric, non-piezoelectric films operating under dc bias – can be used to make electrically tunable TFBARs and that the devices can be switched on or off depending on the dc bias state. The devices were then fabricated: We integrated BST films onto silicon substrates, micromachined the substrate to create the TFBARs and a new type of suspended planar capacitor which were then characterized, analyzed, and modeled, demonstrating successfully the new concept:

We developed a theory describing the electrical tuning behavior of the dc bias induced acoustic resonances in paraelectric thin films in terms of material parameters. The field dependent constitutive piezoelectric equations were derived from the Landau free energy  $P$ -expansion by taking the linear and nonlinear electrostrictive terms as well as the background permittivity into account. We considered two modes of excitation for the tuning of the acoustic resonances, namely the thickness excitation (TE) mode and the lateral field excitation (LFE) mode. The tuning behavior of the two types of resonators based on BST thin films was modeled and discussed. For the modeling we calculated the relevant tensor components controlling the tuning of the BST resonators from the available literature data.

The fabrication of the membrane-type TFBARs was realized by integrating BST thin films onto silicon substrates and using micromaching technologies. We showed that the developed TFBARs can be switched on or off with a dc bias. At a dc electric field of 615 kV/cm we observed a tuning of -2.4% (-66 MHz) and -0.6% (-16 MHz) for the resonance and antiresonance frequencies of the device, while the resonance frequency at a dc electric field extrapolated to 0 kV/cm was 2.85 GHz. The effective electromechanical coupling factor  $k_{eff}^2$  of the device increased up to 4.4%. The tuning was non-hysteretic. The

Quality-factor (Q-factor) of the device was about 200. The developed micromaching processes for the TFBARs were used to fabricate coplanar BST capacitors on silicon. Micromaching was used to remove the Si substrate under the active area of the device. Comparing this new micromachined coplanar capacitor with conventional non-micromachined capacitors, we demonstrated that the removal of the substrate from the active device area resulted in a reduction of parasitic effects. The micromachined coplanar capacitor showed an increased tunability and a reduced loss tangent in comparison to the non-micromachined capacitor. The micromachined capacitor showed a relative tunability of 37% at a dc electric field of 1100 kV/cm. The loss tangent was 0.08 and 0.06 at zero and maximum dc bias, respectively, at a measurement frequency of 20 GHz.

The integration of epitaxial BST thin films on silicon was studied as well because of its potential improvement of the device performance in comparison to devices based on polycrystalline films. Two different electrode/buffer layer systems,  $\text{YBa}_2\text{Cu}_3\text{O}_{7-x}$  (YBCO) /  $\text{CeO}_2$  /  $\text{Y}_x\text{Zr}_{1-x}\text{O}_{2-x/2}$  (YSZ) and TiN were used for the integration. Epitaxial BST thin films were grown with both structures. For the BST / YBCO /  $\text{CeO}_2$  / YSZ / Si structure, the BST unit cell was rotated by  $45^\circ$  in the in-plane dimension with respect to the substrate. The BST layer exhibited good structural quality as indicated by a Full Width at Half Maximum (FWHM) of  $0.5^\circ$  of the rocking curve of the BST(002) diffraction peak. For the BST / TiN / Si structure, the BST layer was grown with a cube-on-cube epitaxial relationship on the silicon substrate, thus demonstrating epitaxially grown BST on silicon using conventional bottom electrode that is easily acceptable by the microelectronic industry. However, in this case, the structural quality of the BST layer was reduced in comparison to the BST / YBCO /  $\text{CeO}_2$  / YSZ / Si structure. The FWHM of the rocking curve of the BST(002) diffraction peak was  $2.2^\circ$ . We established the temperature ( $T=550$  to  $600^\circ\text{C}$ ) and pressure ( $p \approx 10^{-7}$  to  $5 \times 10^{-4}$  Torr) conditions for the growth of epitaxial BST thin films on TiN-buffered Si. At too high temperatures and/or oxygen pressures epitaxial BST thin film growth was impeded due to the oxidation of the TiN layer.

By introducing experimental results from the electrical characterization of the micromachined devices with the polycrystalline BST into our developed theory, we could successfully model the tuning behavior of our fabricated TFBARs. The modeling allowed us to de-embed the intrinsic electromechanical properties of a freestanding BST layer. The effect of increasing mechanical load on the tuning performance of the device was modeled and studied experimentally. Under strong mechanical load, the tuning of both resonance and antiresonance frequency was reduced. The effect was attributed to a reduction

in the tuning of  $k_{eff}^2$  of the device and of the sound velocity of the BST layer.

**Keywords:** tunable, bulk acoustic wave, thin film bulk acoustic wave resonator, TFBAR, barium strontium titanate, pulsed laser deposition, MEMS, rf-MEMS.

# Kurzfassung

Akustische Raumwellen-Dünnschichtresonatoren (TFBARs) wurden vor einem Jahrzehnt entwickelt und werden seitdem in Geräten zur mobilen Kommunikation intensiv eingesetzt. Das “Herzstück” eines TFBAR ist eine piezoelektrische Dünnschicht, welche als ein akusto-elektrischer Wandler fungiert und so die Signalübertragung bei einer bestimmten Frequenz stabilisiert. Wegen verschiedener Gründe wie beispielsweise die effiziente Nutzung des Raumes in mobilen Kommunikationsgeräten besteht ein Interesse diese TFBARs abstimmbar zu machen, so dass ein einzelner TFBAR für verschiedene Frequenzbänder eingesetzt werden kann. Diese Arbeit demonstriert zum ersten Mal elektrisch abstimbare TFBARs, welche aus lediglich einem Bauelement bestehen.

Es wurde eine Theorie entwickelt, welche das Abstimmverhalten von gleichspannungsinduzierten akustischen Raumwellen beschreibt. Dann stellten wir die Hypothese auf, dass der gleichspannungsinduzierte piezoelektrische Effekt in  $\text{Ba}_x\text{Sr}_{1-x}\text{TiO}_3$  (BST) genutzt werden kann, um elektrisch abstimbare TFBARs herzustellen, und dass die Bauelemente über ein Gleichspannungsfeld an- oder ausgeschaltet werden können. Anschließend wurden diese Bauelemente hergestellt: Wir integrierten die BST Schichten auf Siliziumsubstraten, mikrobearbeiteten die Substrate, um so die TFBARs und einen neuartigen, freistehenden planaren Kondensator zu verwirklichen, welche dann charakterisiert, analysiert und modelliert wurden. Dabei konnten wir dieses neue Konzept erfolgreich demonstrieren:

Wir entwickelten eine Theorie, die das Abstimmverhalten der gleichspannungsinduzierten akustischen Resonanzen beschreibt. Die feldabhängigen, piezoelektrischen Gleichungen wurden ausgehend von der  $P$ -Erweiterung der freien Landauenergie hergeleitet. Dabei wurden Terme für die lineare und nichtlineare Elektrostriktion, sowie die Hintergrundpermittivität mit einbezogen. Es wurden zwei verschiedene Modi der Anregung, der Dickenanregungs- (TE) und der Seitfeldanregungsmodus (LFE), untersucht. Das Abstimmverhalten von BST Resonatoren, die im TE and LFE Modus arbeiten, wurde modelliert und diskutiert. Für die Modellierungen haben wir die relevanten Tensorkomponenten, die die Abstimmbarkeit der BST Resonatoren kontrollieren, ausgehend von vorhandenen Literaturdaten berechnet.

Die Herstellung der Membran-TFBARs wurde durch die Integration der BST Dünnschichten auf Siliziumsubstrate und durch den Einsatz von Mikrobearbeitungsverfahren verwirklicht. Wir zeigten, dass die entwickelten TFBARs mit einem Gleichspannungsfeld an- oder ausgeschaltet werden können. Für

ein Gleichspannungsfeld von 615 kV/cm wurde eine Abstimmbarkeit von -2.4% (-66 MHz) und -0.6% (-16 MHz) für die Resonanz- und Antiresonanzfrequenz beobachtet. Die Resonanzfrequenz für ein gegen 0 kV/cm gehendes Gleichspannungsfeld lag bei 2.85 GHz. Der effektive elektromechanische Kopplungsfaktor  $k_{eff}^2$  des Bauteils stieg auf 4.4% an. Die Abstimmbarkeit zeigte keine Hysterese. Der Qualitätsfaktor (Q-factor) des Bauteils lag bei circa 200. Die für die TFBARs entwickelten Mikrobearbeitungsverfahren wurden benutzt, um koplanare BST Kondensatoren auf Silizium herzustellen. Mit Hilfe der Mikrobearbeitungsverfahren wurde das Siliziumsubstrat unter dem aktiven Bereich des Bauteils entfernt. Durch den Vergleich mit einem nicht-mikrobearbeiteten Kondensator konnten wir zeigen, dass durch das Entfernen des Substrats unter dem aktiven Bereich des Bauelements eine Verringerung von parasitischen Effekten erzielt werden kann. Der mikrobearbeitete Kondensator zeigte eine erhöhte Abstimmbarkeit und einen verringerten Verlustfaktor im Vergleich zum nicht-mikrobearbeiteten Kondensator. Die Abstimmbarkeit des mikrobearbeiteten Kondensators betrug 37% für ein Gleichspannungsfeld von 1100 kV/cm. Bei einer Frequenz von 20 GHz war der Verlustfaktor des Bauteils 0.08 bei 0 kV/cm, beziehungsweise 0.06 bei 1100 kV/cm.

Die Integration von epitaktischen BST Dünnschichten wurde wegen einer möglichen Verbesserung der Bauteile im Vergleich zu Bauteilen, die auf polykristallinen Schichten basieren, ebenfalls untersucht. Zwei verschiedene Elektroden / Pufferschichtsysteme,  $\text{YBa}_2\text{Cu}_3\text{O}_{7-x}$  (YBCO) /  $\text{CeO}_2$  /  $\text{Y}_x\text{Zr}_{1-x}\text{O}_{2-x/2}$  (YSZ) und TiN, wurden für die Integration untersucht. Epitaktische BST Dünnschichten konnten auf beiden Strukturen aufgebracht werden. Bei der BST / YBCO /  $\text{CeO}_2$  / YSZ / Si Struktur war die BST Einheitszelle im Vergleich zum Substrat um  $45^\circ$  in der Ebene rotiert. Die BST Schicht zeigte eine gute strukturelle Qualität. Die Halbwertsbreite (FWHM) der Rockingkurve der BST(002) Diffraktionslinie betrug  $0.5^\circ$ . Bei der BST / TiN / Si Struktur wurde die BST Schicht mit einer sogenannten epitaktischen Würfel-auf-Würfel Beziehung auf das Siliziumsubstrat aufgebracht. Dabei konnten wir die Integration von epitaktischen BST Schichten auf Silizium mit einer Grundlektrode demonstrieren, welche kompatibel mit den Anforderungen der Mikroelektronikindustrie ist. Die strukturelle Qualität war jedoch im Vergleich zu der der BST / YBCO /  $\text{CeO}_2$  / YSZ / Si Struktur vermindert. Die FWHM der Rockingkurve der BST(002) Diffraktionslinie betrug  $2.2^\circ$ . Wir bestimmten die Temperatur- und Druckbedingungen ( $T=550$  bis  $600^\circ\text{C}$ ;  $p \approx 10^{-7}$  bis  $5 \times 10^{-4}$  Torr), bei denen ein epitaktisches Wachstum von BST auf TiN / Si beobachtet werden konnte. Bei zu hohen Temperaturen und/oder Sauerstoffdrücken wurde das epitaktische BST Dünnschichtwachstum durch die Oxidation der TiN Schicht verhindert.

Durch die Einführung der experimentellen Daten der elektrischen Charakterisierung der Bauelemente in unsere entwickelte Theorie konnten wir das Abstimmverhalten unserer hergestellten TFBARs erfolgreich modellieren. Die Modellierungen ermöglichten es die intrinsischen elektromechanischen Eigenschaften einer freistehenden BST Schicht zu extrahieren. Der Effekt einer erhöhten mechanischen Last auf das Abstimmvermögen unserer Bauteile wurde ebenfalls modelliert und experimentell untersucht. Eine große mechanische Last führte zu einer geringeren Abstimmbarkeit der Resonanz- und Antiresonanzfrequenz. Der Effekt kann mit einer geringeren Abstimmbarkeit von  $k_{eff}^2$  des Bauteils, sowie der Schallgeschwindigkeit in der BST Schicht erklärt werden.

**Stichwörter:** abstimmbar, akustische Raumwelle, akustischer Raumwellen-Dünnschichtresonator, TFBAR, Barium-Strontium-Titanat, pulsed laser deposition, MEMS, rf-MEMS.

# Contents

<b>1</b>	<b>Introduction</b>	<b>1</b>
1.1	Aims of the thesis . . . . .	2
1.2	Outline of the thesis . . . . .	3
<b>2</b>	<b>State of the art - Literature review</b>	<b>5</b>
2.1	BST thin films for tunable applications . . . . .	5
2.1.1	The BST solid solution . . . . .	5
2.1.2	Tunability and dielectric loss . . . . .	7
2.1.3	Dielectric response of BST thin films . . . . .	9
2.1.4	Integration of epitaxial BST thin films on silicon . . . . .	16
2.1.5	Applications . . . . .	19
2.2	Piezoelectricity induced by a dc bias through the electrostrictive effect . . .	20
2.3	Introduction to TFBAR technology . . . . .	21
2.3.1	1-dimensional model for acoustic resonances in piezoelectric plates .	23
2.3.2	Tuning of TFBARs . . . . .	26
<b>3</b>	<b>Theory of electrical tuning of dc bias induced acoustic resonances in paraelectric thin films</b>	<b>31</b>
3.1	Introduction . . . . .	31
3.2	Derivation of the field dependent piezoelectric constitutive equations . . . .	32
3.3	Field dependence of the acoustic resonances (TE mode) . . . . .	35
3.4	Field dependence of the acoustic resonances (LFE mode) . . . . .	38
3.5	Relation between the electromechanical coupling factors and the relative tunability . . . . .	40
3.6	Modeling and Discussion . . . . .	41
3.7	Summary and Conclusions . . . . .	48
<b>4</b>	<b>Growth and characterization of <math>\text{Ba}_x\text{Sr}_{1-x}\text{TiO}_3</math> thin films on platinized silicon</b>	<b>51</b>
4.1	Introduction . . . . .	51
4.2	Film growth and fabrication of test devices . . . . .	51

## CONTENTS

---

4.2.1	Pulsed Laser Deposition method . . . . .	52
4.2.1.1	The ablation process . . . . .	53
4.2.1.2	Film growth by PLD . . . . .	54
4.2.2	Film growth and annealing conditions . . . . .	55
4.2.3	Fabrication of test structures . . . . .	56
4.3	Results and Discussion . . . . .	57
4.3.1	Structural characterization . . . . .	57
4.3.2	Electrical characterization . . . . .	59
4.4	Summary and Conclusions . . . . .	62
<b>5</b>	<b>Fabrication, characterization and modeling of BST-based TFBARs</b>	<b>65</b>
5.1	Introduction . . . . .	65
5.2	Experimental details . . . . .	66
5.2.1	Device fabrication . . . . .	66
5.2.1.1	Silicon wafers . . . . .	66
5.2.1.2	SiO <sub>2</sub> deposition . . . . .	66
5.2.1.3	Patterning of backside SiO <sub>2</sub> layer - hard mask fabrication	67
5.2.1.4	Bottom electrode deposition and patterning . . . . .	67
5.2.1.5	BST film deposition . . . . .	68
5.2.1.6	Top electrode deposition . . . . .	68
5.2.1.7	Membrane liberation - The Bosch process . . . . .	68
5.2.2	Electrical characterization . . . . .	71
5.3	Results and Discussion . . . . .	71
5.3.1	Properties of BST-based TFBARs . . . . .	71
5.3.2	Modeling of BST-based TFBARs . . . . .	78
5.3.3	Effect of mechanical load on TFBAR characteristics . . . . .	82
5.4	Summary and Conclusions . . . . .	87
<b>6</b>	<b>Integration of micromachined coplanar capacitors on silicon</b>	<b>89</b>
6.1	Introduction . . . . .	89
6.2	Experimental details . . . . .	91
6.2.1	Fabrication of the devices . . . . .	91
6.2.2	Electrical characterization . . . . .	92
6.3	Results and Discussion . . . . .	92
6.4	Summary and Conclusions . . . . .	100
<b>7</b>	<b>Integration of epitaxial BST thin films on silicon</b>	<b>103</b>
7.1	Introduction . . . . .	103
7.2	Experimental details . . . . .	104
7.2.1	Processing of BST thin films and electrode/buffer layers . . . . .	104
7.2.1.1	BST/YBCO/CeO <sub>2</sub> /YSZ/Si system . . . . .	104



## CONTENTS

---

7.2.1.2	BST/TiN/Si system . . . . .	105
7.2.2	Structural characterization . . . . .	105
7.3	Results and Discussion . . . . .	106
7.4	Summary and Conclusions . . . . .	118
<b>8</b>	<b>Conclusions and outlook</b>	<b>119</b>
<b>A</b>	<b>Calculation of relevant tensor components for BST thin films</b>	<b>123</b>
	<b>References</b>	<b>125</b>



# List of Figures

2.1	Unit cell of BST. . . . .	6
2.2	Temperature dependence of the permittivity for different $x$ values of the $\text{Ba}_x\text{Sr}_{1-x}\text{TiO}_3$ solid solution. The graph is based on the data of Smolenskii et al. [19] and was adapted from Ref. [10]. . . . .	6
2.3	Dependence of dc electric field $E_{dc}$ needed to achieve a tunability $n$ of 2 for a given zero-bias permittivity $\varepsilon(0)$ of the BST thin film as calculated with Eq. (2.3). . . . .	8
2.4	Comparison of the temperature dependence of the permittivity of a BST thin film and a corresponding bulk sample with the same composition [23].	10
2.5	Thickness dependence of the permittivity of BST( $x=0$ ) thin films [28]. . . .	11
2.6	Dependence of inverse capacitance density ( $A/C$ ) on the thickness of BST( $x=0.7$ ) thin films measured at different temperatures [31]. . . . .	11
2.7	Temperature (a) and electric field (b) dependence of the permittivity of BST thin films with different thermal strains due to differences in the thermal expansion coefficients of films and substrates [36]. . . . .	13
2.8	Grain size dependence of the permittivity in BST( $x=1$ ) thin films and ceramics. The data was adapted from Waser [46]. . . . .	15
2.9	Coplanar (a) and parallel-plate (b) capacitor geometries. . . . .	20
2.10	Cross sections of piezoelectric plates resonating in the TE mode (a) and the LFE mode (b). . . . .	24
2.11	Equivalent circuit of a resonator with an in-series connected tunable capacitor. The dashed rectangle shows the equivalent circuit of a resonator. .	27
2.12	Dependence of the resonance frequency (a) and the Q-factor (b) of a ZnO TFBAR on the capacitance $C_s$ of an in-series connected varactor [115]. . .	28
3.1	Schematic drawings of the considered resonator geometries. For the TE mode a parallel-plate capacitor geometry as shown in (a) is considered. In this case the polarization $P^{dc}$ is parallel to the direction of the traveling acoustic wave indicated by the wave vector $k$ . The coplanar capacitor shown in (b) corresponds to the LFE mode. Here, the polarization $P^{dc}$ is perpendicular to the direction of the traveling acoustic wave. . . . .	35

## LIST OF FIGURES

---

3.2	Modeled dependence of the tuning of the resonance and antiresonance frequencies on the relative tunability $n_r$ of a BST( $x=0.3$ ) thin film with (111) orientation in the TE mode. If the sum $\gamma_t + \mu/2$ is positive the antiresonance frequency (filled circle) and the resonance frequency (filled triangle) shift down to lower frequencies. If the sum $\gamma_t + \mu/2$ is negative the antiresonance frequency (open circle) shifts up whereas the resonance frequency (open triangle) shifts down. In any case the resonance frequency shifts down and shows a much stronger dependence on the dc bias than the antiresonance frequency. The values used in the modeling were taken from Tab. 3.2: $q_{33} = 1.1 \times 10^{10}$ m/F; $\varepsilon_{33}^r = 300$ ; $\varepsilon^b = 7$ ; $A_t = 0.178$ . The value of $m_{333} = +7.5 \times 10^{10}$ m/F was used for $\gamma_t + \mu/2$ being positive. For a negative sign of the sum $\gamma_t + \mu/2$ the value of $m_{333} = -7.5 \times 10^{10}$ m/F was used in the modeling. . . . .	43
3.3	Modeled dependence of the resonance and antiresonance frequencies on the relative tunability $n_r$ for a BST( $x=0.3$ ) thin film with (110) orientation in the LFE mode. The values used for the modeling were taken from Tab. 3.2: $q_{31} = 9.4 \times 10^{10}$ m/F; $m_{331} = \pm 10^{11}$ m/F; $\varepsilon_{11}^r = 300$ ; $\varepsilon^b = 7$ ; $A_{lat} = 0.11$ . For $m_{331} = +10^{11}$ m/F the antiresonance (filled triangles) frequency shows a stronger dc bias dependence than the resonance (filled circles) frequency. Both resonance and antiresonance frequencies shift down with increasing bias. For $m_{331} = -10^{11}$ m/F the tuning of the antiresonance (open triangles) and the resonance (open circles) frequency is slightly reduced but shows the same principal behavior as for $m_{331} = +10^{11}$ m/F. . . . .	45
3.4	Modeled dependence of the resonance and antiresonance frequencies on the relative tunability $n_r$ for a BST( $x=0.3$ ) thin film with (001) orientation in the LFE mode. The values used for the modeling are taken from Tab. 3.2: $q_{31} = -2.18 \times 10^9$ m/F; $m_{331} = \pm 10^{11}$ m/F; $\varepsilon_{11}^r = 300$ ; $\varepsilon^b = 7$ ; $A_{lat} = 0.00374$ . For $m_{331} = +10^{11}$ m/F both antiresonance (filled triangles) and resonance frequency (filled circles) shift down with increasing dc bias. The antiresonance frequency shows a stronger dc bias dependence than the resonance frequency. For $m_{331} = -10^{11}$ m/F both antiresonance (open triangles) and resonance frequency (open circles) shift up with increasing dc bias. . . . .	46
4.1	Schematic drawing of a PLD setup. . . . .	52
4.2	Schematic viewgraph of possible processes occurring during film nucleation. . . . .	54
4.3	Schematic drawing of a test capacitor. The large capacitor $C_{coup}$ provides capacitive coupling to the Pt bottom electrode. . . . .	56
4.4	Comparison of x-ray diffraction patterns of BST thin films with composition $x=0.3$ and $x=0.7$ . . . . .	57
4.5	TEM plane view images of BST ( $x=0.3$ ) (a) and BST ( $x=0.7$ ) (b) thin films. . . . .	58

## LIST OF FIGURES

---

4.6	Typical example of an AFM scan. The image is shown for the BST( $x=0.3$ ) thin film. . . . .	59
4.7	Temperature dependence of the permittivity (open circles) and the loss tangent (filled circles) of the BST thin films. (a) and (b) show the data for the BST films with $x=0.3$ and $x=0.7$ composition, respectively. . . . .	61
4.8	Dependence of the permittivity (solid line) and the loss tangent (filled circles) on the dc electric field. (a) and (b) show the data for the BST films with $x=0.3$ and $x=0.7$ composition, respectively. . . . .	62
5.1	Process flow for the fabrication of the BST TFBAR. . . . .	69
5.2	An example of a SEM top view image of a BST TFBAR. The floating Pt bottom electrode is centered on the membrane. The device is contacted by G-S-G (Ground-Signal-Ground) probes. The contact to the bottom electrode is realized by capacitive coupling. . . . .	70
5.3	Schematic cross-sections of the fabricated device with minimum mechanical load (a) and the device with maximum mechanical load (b). . . . .	70
5.4	Admittance against frequency for the BST( $x=0.3$ )-based TFBAR at zero and 615 kV/cm. The real and imaginary part of the admittance are shown as solid and dashed lines, respectively. . . . .	72
5.5	Conductance (real part of admittance) against frequency for the BST( $x=0.3$ )-based TFBAR at different dc electric fields. . . . .	72
5.6	Resistance (real part of impedance) against frequency for the BST( $x=0.3$ )-based TFBAR at different dc electric fields. . . . .	74
5.7	Dependence of the resonance (filled squares) and antiresonance frequency (filled triangles) on the dc electric field. . . . .	74
5.8	Tuning of resonance (filled squares) and antiresonance (filled triangles) frequency and effective electromechanical coupling factor (open diamonds) against dc electric field. . . . .	75
5.9	Dependence of the Q-factor of the BST TFBAR on the dc electric field. . .	76
5.10	Non-hysteretic dc bias dependence of the resonance and antiresonance frequencies. The resonance frequency on the forward and backward sweep of the dc bias is shown as open triangles and plus signs, respectively. The antiresonance frequency on the forward and backward sweep of the dc bias is shown as open circles and crosses, respectively. . . . .	77
5.11	Experimental and modeled values for the dc bias dependence of the resonance and antiresonance frequencies. The experimental values for the resonance and antiresonance frequencies are shown as (filled squares) and (filled circles), respectively. The modeled values of the resonance and antiresonance frequencies are shown as (open squares) and (open circles), respectively. . . . .	81

## LIST OF FIGURES

---

5.12	Dependence of the relative dielectric tunability $n_r$ and the tuning of the resonance frequency on the dc electric field for BST TFBARs with 100 and 700 nm thick SiO <sub>2</sub> layers. The relative tunabilities of the BST TFBAR with 100 nm SiO <sub>2</sub> (open triangles) and with 700 nm SiO <sub>2</sub> (filled triangles) are essentially the same at a given dc electric field. The tuning of the resonance frequency for the BST TFBAR with 100 nm SiO <sub>2</sub> (open circles) is stronger than the tuning of the resonance frequency of the BST TFBAR with 700 nm SiO <sub>2</sub> (filled circles). . . . .	83
5.13	Modeled (open squares) and experimental (filled triangles) values of the resonance frequency at $E_{dc}$ extrapolated to 0 kV/cm for different thicknesses of the SiO <sub>2</sub> layer attached to the BST TFBAR. . . . .	84
5.14	Modeled and experimental dependence of the tuning of resonance and antiresonance frequencies on the thickness of the SiO <sub>2</sub> layer. The experimental values for the tuning of the resonance and antiresonance frequencies are shown by (open triangles) and (open squares), respectively. The modeled values for the tuning of the resonance and antiresonance frequencies are shown by (filled triangles) and (filled squares), respectively. . . . .	85
6.1	Process flow for the fabrication of the micromachined coplanar BST capacitor.	93
6.2	Example of an optical micrograph of a micromachined coplanar BST capacitor. The electrode gap of the capacitor is centered on the membrane. .	94
6.3	RHEED pattern of the YSZ layer after film deposition (a) and after annealing the sample at T=1000 °C for 5h in flowing O <sub>2</sub> (b). . . . .	94
6.4	XRD pattern of the annealed YSZ/Si substrate after BST thin film deposition. The peak marked by the asterice is the Si(002) peak of the Si substrate. . . . .	95
6.5	Comparison of the frequency dependence of the capacitance of a micromachined and a non-micromachined coplanar BST capacitor under zero and 1100 kV/cm dc electric field. . . . .	96
6.6	Comparison of the dc electric field dependence of the normalized capacitance of a micromachined (open circles) and non-micromachined (open squares) coplanar BST capacitor. The data was measured at 20 GHz. . . .	97
6.7	Comparison of the frequency dependence of the loss tangent of a micromachined and a non-micromachined coplanar BST capacitor at a dc electric field of 0 kV/cm and 1100 kV/cm, respectively. . . . .	99
6.8	Electric field dependence of the capacitance and the loss tangent of the micromachined coplanar capacitor. The data shown was measured at 20 GHz.	100
7.1	XRD $\theta - 2\theta$ -scan of the BST / YBCO / CeO <sub>2</sub> / YSZ / Si multilayer structure. For the phases forming the structure only peaks of the (00l) family of lattice planes could be detected. . . . .	107

## LIST OF FIGURES

7.2	RHEED diffraction patterns of the different layers of the BST / YBCO / CeO <sub>2</sub> / YSZ / Si structure. The incident electron beam was parallel to Si[100]. . . . .	108
7.3	XRD $\phi$ -scans taking around Si(hhh) (a) and Si(hh0) (b). . . . .	108
7.4	Dependence of the FWHM of the rocking curve of the TiN(002) diffraction peak on the deposition temperature of the TiN thin film. The FWHM decreased from 2.5° at a deposition temperature of 700 °C to 0.7° at a deposition temperature of 900 °C. . . . .	110
7.5	RHEED diffraction patterns of the TiN layers deposited at T=700 °C and T=900 °C. The incident electron beam was parallel to Si[100]. With increasing deposition temperature the RHEED patterns became sharper with more intense diffraction spots indicating an improvement in the structural quality. . . . .	111
7.6	XRD $\theta - 2\theta$ -scans of BST thin films deposited under different temperature and pressure conditions. The diffraction pattern of the BST thin film deposited at $p=5 \times 10^{-4}$ Torr and T=600 °C is labeled as (a). The diffraction patterns of the BST thin films deposited at $p \leq 10^{-7}$ Torr and at 600 °C, 700 °C, and 800 °C are labeled as (b), (c), and (d), respectively. . . . .	112
7.7	RHEED diffraction patterns for BST thin films deposited under different temperature and pressure conditions. The diffraction pattern of the BST thin film deposited at $p=5 \times 10^{-4}$ Torr and T=600 °C is labeled as (a). The diffraction patterns of the BST thin films deposited at $p \leq 10^{-7}$ Torr and at 600 °C, 700 °C, and 800 °C are labeled as (b), (c), and (d), respectively. The labels are identical to Fig. 7.6 to allow direct comparison of the data. . . . .	113
7.8	Dependence of the crystalline nature of the BST thin films deposited on TiN-buffered Si on the deposition temperature and pressure. Epitaxial BST thin film growth was only observed in a narrow temperature and pressure window. . . . .	113
7.9	SEM images of the surface of BST thin films with epitaxial (a) and polycrystalline (b) structure. The epitaxial BST thin film shown in (a) was deposited at T=600 °C and $p(\text{O}_2) = 5 \times 10^{-4}$ Torr. The polycrystalline BST thin film shown in (b) was deposited at T=600 °C and $p(\text{O}_2) = 5 \times 10^{-2}$ Torr. . . . .	114
7.10	TEM cross section images of BST thin films with epitaxial (a) and polycrystalline (b) structure. The epitaxial BST thin film shown in (a) was deposited at T=600 °C and $p(\text{O}_2) = 5 \times 10^{-4}$ Torr. The polycrystalline BST thin film shown in (b) was deposited at T=600 °C and $p(\text{O}_2) = 5 \times 10^{-2}$ Torr. . . . .	115
7.11	XRD $\phi$ -scans around Si(hh0) for an epitaxial BST/TiN/Si heterostructure. The diffraction peaks of the BST and the TiN layer coincide with the peaks of the Si substrate indicating that the BST and the TiN films have the same in-plane orientation as the Si substrate. . . . .	116





# Chapter 1

## Introduction

In recent years there has been an enormous growth in wireless communication technologies including applications such as satellite, bluetooth, wireless-lan networks, mobile communication (GSM, GPRS, UMTS, CDMA), etc. All these communication systems operate in different frequency bands, while even for a given technology different frequency bands might be used over the world. The integration of different applications in handheld devices like cellular phones increases the number of circuits and components in these devices. This leads to an increase in size, weight, and cost of these devices opposing the consumers demands of reduced costs and increased functionality.

Tunable technologies offer a possibility to overcome the above mentioned problems by offering adaptive, frequency agile components and circuits. In the ideal case, the characteristics of the components can be tuned, so that a circuit can operate in different frequency bands. In this way, the number of components and circuits could be reduced, while functionality could be increased.

There are several tunable technologies that are of potential interest for wireless communication systems, all having advantages and drawbacks.

Mechanically [1] or magnetically [2; 3] tuned circuits are less suitable in this context because of their large size.

Semiconductor devices are currently dominant in tunable circuits [4; 5]. Different types of components like diodes or transistors can offer small size, fast tuning speed, high tunabilities, and easy integration in microwave monolithic integrated circuits (MMICs). Drawbacks of the technology are the rather poor power handling capabilities scaling down with device size and a degradation of the Q-factor at high frequencies.

Microelectromechanical systems (MEMS) are an interesting technology for tunable applications [6]. Tunability is achieved by the physical movements of parts induced by electrostatic, electrostrictive, piezoelectric mechanisms or thermal effects. The technology offers low losses, good power handling capabilities, and good tunabilities. Drawbacks include the slow tuning speed which is limited to the  $\mu s$  range and stringent packaging requirements which increase the costs of the devices.

## 1. INTRODUCTION

---

Ferroelectric materials, typically in thin film form, can also be used for tunable technologies [7; 8; 9; 10; 11]. Tunability is realized by applying a dc bias to the material, which reduces its dielectric permittivity. Attractive features of the technology are good tunability, fast tuning speed, good power handling capabilities, and low power consumption and losses. The components are inexpensive, of small size, and can be integrated in microelectronic circuits.

The performance of tunable ferroelectric components is controlled by the properties of the tunable material and by device design. As a tunable material  $\text{Ba}_x\text{Sr}_{1-x}\text{TiO}_3$  (BST) has been most deeply investigated. Although single crystals of BST offer good tunabilities and very low dielectric losses up to high frequencies ( $f \leq 10$  GHz) [12], BST thin films show a degraded performance in comparison. This can be attributed to various factors like size effects, material chemistry, microstructure, stress and strain effects, defects, and imperfect structural properties, all of which are intensively investigated to improve the material's properties.

Beside the optimization of material performance, the device design is also of great importance to reduce parasitic effects degrading the device performance. Examples include the loss contribution from the electrodes that has to be reduced [13; 14], inductances stemming from the metal electrodes that can lead to some frequency dependence of the capacitance and also to self-resonance effects, and parasitic effects stemming from the substrates.

The most important tunable ferroelectric component is the varactor which is a tunable capacitor. This component can be integrated with other components to build tunable devices like filters, voltage controlled oscillators, phase shifters, etc. An important requirement for the success of the ferroelectric technology for tunable applications is its integration in silicon technology offering industrial scale up, low costs, and increased functionality by combining semiconductor and ferroelectric properties.

Recently, it has been observed that the application of a dc bias to tune BST thin films leads to the induction of piezoelectricity in the material through the electrostrictive effect [15; 16; 17]. This field induced piezoelectricity might offer the possibility to fabricate new types of tunable devices based on BST thin films [18].

### 1.1 Aims of the thesis

In this thesis we are going to address the integration of BST thin films on Si for tunable devices. We are interested in studying the effect of dc bias induced piezoelectricity in paraelectric BST thin films. We want to investigate whether the dc bias induced acoustic resonances are tunable via a dc electric field, whether the effect can be used to develop a tunable Thin Film Bulk Acoustic Wave Resonator (TFBAR), which factors control the resonance tuning, and which tuning performance can be achieved. Therefore, we developed processes for the fabrication of a TFBAR based on BST thin films.

In addition, we aim to develop an appropriate theory describing the electrical tuning of the dc bias induced acoustic resonances in terms of the material parameters of the BST layer.

We are also interested in the implementation of epitaxial BST thin films on Si because of its potential improvement of the performance of tunable devices in comparison to devices based on polycrystalline films. We are going to study different electrode / buffer layer systems with the aim of realizing the growth of epitaxial BST films of high structural quality.

## 1.2 Outline of the thesis

After the introduction of this thesis in Chapter 1, in Chapter 2 we review the literature being of importance for the results obtained in this thesis.

In Chapter 3 we develop a theory on the electrical tuning of dc bias induced acoustic resonances in paraelectric thin films. We calculate the relevant tensor components controlling the tuning behavior for different BST thin film compositions and orientations from the available literature data. The tuning behavior is modeled and discussed for the case of BST thin films.

Chapter 4 deals with the structural and low frequency electrical characterization of BST thin films deposited on platinized silicon. Two different BST compositions ( $x=0.3$  and  $x=0.7$ ) are investigated.

In Chapter 5 we present the fabrication, characterization, and modeling of tunable TFBARs based on BST thin films in the paraelectric phase. We demonstrate that the TFBAR is tunable via a dc electric field. The tuning behavior and the Q-factor of the devices are investigated. The theory developed in Chapter 3 is successfully applied to model the tuning behavior of the devices. The effect of increasing mechanical load on the performance of the devices is investigated experimentally and theoretically.

In Chapter 6 we deal with the fabrication of coplanar capacitors on silicon. We use micromachining technologies to remove the Si substrate under the active area of the device. This reduces parasitic effects stemming from the substrate and enhances the performance of the device as illustrated by comparison with a non-micromachined coplanar capacitor.

In Chapter 7 we study the integration of epitaxial BST thin films on silicon. Since epitaxial BST thin film growth directly on silicon is not possible, we used two different electrode/buffer layer systems for the integration. The deposition conditions, epitaxial relationships, and the structural quality of the two heterostructures are investigated.



# Chapter 2

## State of the art - Literature review

In this chapter we present an overview of the literature relevant to this thesis. The chapter includes only references published before the start of this thesis in June 2005.

### 2.1 BST thin films for tunable applications

#### 2.1.1 The BST solid solution

$\text{Ba}_x\text{Sr}_{1-x}\text{TiO}_3$  (BST) is a solid solution between  $\text{SrTiO}_3$  (BST with  $x=0$ ) and  $\text{BaTiO}_3$  (BST with  $x=1$ ). The material crystallizes in the perovskite structure where the Ba and/or Sr atoms occupy the corners of the unit cell, the Ti atom occupies the center of the unit cell and the oxygen atoms are placed at the center of the faces of the unit cell. The perovskite crystal structure is shown in Fig. 2.1.

Regarding the tolerance factor the Ti atom is a little too small for the crystal structure. At high temperatures it has sufficient thermal energy to vibrate around its equilibrium position and forms an inversion center for the material's unit cell. In this case the material is centrosymmetric, of cubic structure, and shows paraelectric behavior. On cooling down the Ti atoms loses thermal energy and, at a certain temperature, a displacement of the Ti and O atoms occurs which results in a phase transition. The temperature at which the phase transition takes place is called the Curie temperature  $T_c$ . Below  $T_c$ , the material is non-centrosymmetric, of tetragonal symmetry, and shows ferroelectric behavior. This means that the material has a spontaneous polarization that can be switched by an electric field. The phase transition temperature depends on the Ba/Sr ratio of the material and is characterized by a pronounced peaking in the dielectric permittivity. Figure 2.2 shows the temperature dependence of the permittivity for different Ba/Sr ratios of the BST solid solution.

For tunable applications BST in the paraelectric phase is of interest. In the paraelectric phase the dc bias dependent properties are non-hysteretic and the dielectric losses are expected to be lower than in the ferroelectric state [10].

## 2. STATE OF THE ART - LITERATURE REVIEW

---

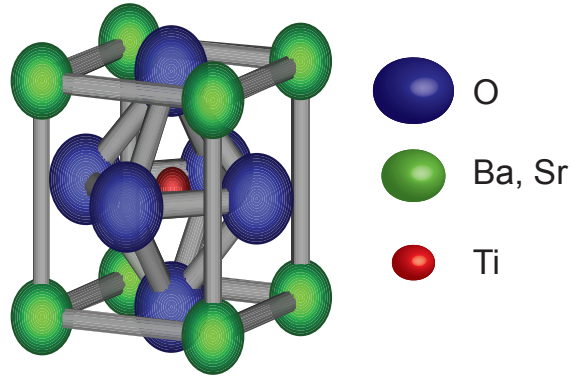


Figure 2.1: Unit cell of BST.

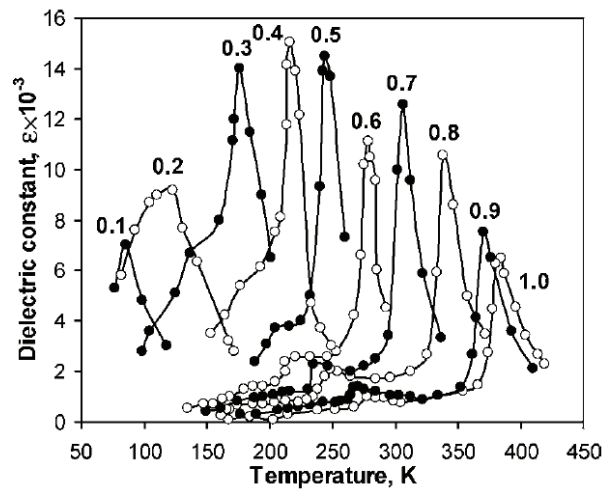


Figure 2.2: Temperature dependence of the permittivity for different  $x$  values of the  $\text{Ba}_x\text{Sr}_{1-x}\text{TiO}_3$  solid solution. The graph is based on the data of Smolenskii et al. [19] and was adapted from Ref. [10].

For BST( $x=1$ )  $T_c$  is 120 °C and shifts down by 3.4 °C for every mole percent of  $x$  [20]. BST( $x=0$ ) is a quantum paraelectric or incipient ferroelectric meaning that the material is paraelectric down to 0 K and does not support spontaneous polarization.

### 2.1.2 Tunability and dielectric loss

#### Tunability

By applying a dc electric field to the material a reduction of the permittivity of BST is observed. This defines the tunability  $n$ :

$$n = \frac{\varepsilon(0)}{\varepsilon(E_{dc})} \quad (2.1)$$

where  $\varepsilon(0)$  and  $\varepsilon(E_{dc})$  correspond to the permittivity at zero and under dc bias. Sometimes one also uses the relative tunability  $n_r$  to express the change in permittivity with the dc electric field:

$$n_r = \frac{\varepsilon(0) - \varepsilon(E_{dc})}{\varepsilon(0)} = \frac{n - 1}{n} \quad (2.2)$$

In general, a higher tunability is observed for a higher permittivity at zero bias [10]. For a given  $\varepsilon(0)$  a higher  $n$  is observed for a higher  $E_{dc}$  applied. It is instructive to give an expression for the electric field  $E_n$  needed to achieve a certain tunability  $n$ :

$$E_n = \frac{\sqrt{n-1}(2+n)}{\varepsilon_0 \sqrt{27\beta\varepsilon_0}} \frac{1}{\varepsilon(0)^{\frac{3}{2}}} \quad (2.3)$$

where  $\varepsilon_0$  is the vacuum permittivity and  $\beta$  is the coefficient of the tensor of dielectric non-linearity. Equation (2.3) clearly shows that a higher  $\varepsilon(0)$  results in a higher  $n$  for a given dc electric field. Figure 2.3 shows  $E_{dc}$  which is needed to achieve a tunability  $n = 2$  in dependence of  $\varepsilon(0)$ . The data was calculated with Eq. (2.3) taking  $\beta = 5.68 \times 10^9 \text{ Vm}^5/\text{C}^3$  which corresponds to the value for a BST( $x=0.3$ ) thin film with (001) orientation (see Chapter 3).

#### Dielectric loss

The dielectric loss is, beside the tunability, the other important property of BST for different applications. The dielectric loss describes the loss of electrical power in the material. It can be expressed in terms of the loss tangent:

$$\tan\delta = \frac{\varepsilon''}{\varepsilon'} \quad (2.4)$$

where  $\varepsilon'$  and  $\varepsilon''$  correspond to the real and the imaginary part of the permittivity.

Concerning the dielectric loss in BST, one has to distinguish between intrinsic and extrinsic contributions to the loss.

## 2. STATE OF THE ART - LITERATURE REVIEW

---

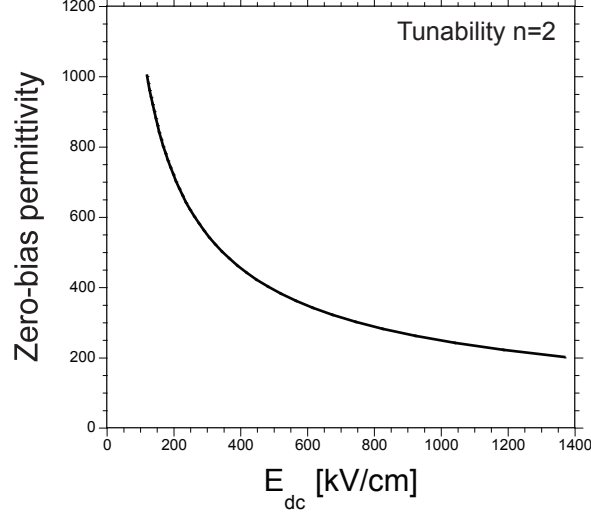


Figure 2.3: Dependence of dc electric field  $E_{dc}$  needed to achieve a tunability  $n$  of 2 for a given zero-bias permittivity  $\varepsilon(0)$  of the BST thin film as calculated with Eq. (2.3).

### Intrinsic losses

The origin of the intrinsic losses is the interaction of the microwave field with the phonons of the material. In centrosymmetric, cubic materials the three- and four-quantum mechanism determine the intrinsic contribution to the losses. If the frequency  $\omega$  is less than the damping of phonons  $\Gamma$ , the phonon transport theory gives the relation [10; 21]:

$$\tan\delta_{ph} \propto \omega T^2 \varepsilon^{1.5} \quad (2.5)$$

where  $\omega$  is the ac-field frequency,  $T$  is the temperature and  $\varepsilon$  is the dielectric permittivity. Applying a dc electric field to the material, the center of symmetry breaks which gives rise to the so-called quasi-Debye mechanism. For  $\omega < \Gamma$  the contribution of the quasi-Debye loss mechanism is given by [10]:

$$\tan\delta_{QD}(E_0) = AI(E_0)\omega n_r \quad (2.6)$$

where  $I(E_0) \rightarrow 1$  in the limit of small relative tunabilities ( $n_r \ll 1$ ) and  $A$  is a field independent constant. In the case of higher fields the simple law given in Eq. (2.6) does not hold and the behavior of  $\tan\delta_{QD}$  vs.  $E_0$  seems to be different for different materials [10].

### Extrinsic losses

The extrinsic losses originate from the interaction of the ac-field with defects. For tunable microwave materials three mechanisms are considered to contribute significantly to the losses at microwave frequencies.



**Loss due to charged defects** The coupling of the ac field with charged defects results in the generation of acoustic waves that tend to dissipate the energy of the microwave field giving rise to an additional loss mechanism. The losses due to charged defects show a nearly linear frequency and permittivity dependence ( $\tan\delta \sim \varepsilon\omega$ ) indicating that the higher the permittivity and the frequency, the higher the losses due to these types of defects.

**Universal-relaxation law** According to the universal-relaxation law mechanism the real  $\varepsilon'$  and the imaginary part  $\varepsilon''$  of the dielectric permittivity have the same frequency dependence ( $\omega^{n-1}$  with  $0 < n < 1$ ) and therefore the contribution to the loss tangent due to this mechanism is frequency independent ( $\tan\delta = \frac{\varepsilon''}{\varepsilon'}$ ).

**Impact of local polar regions** In centrosymmetric materials there may be local polar regions due to various defects or structural imperfections. For example, in the case of BST(x=0) a clear presence of grain-boundary induced polar phase has been observed [22]. Moreover, local polar regions can also appear due to random field effects [8]. In all these local polar regions the quasi-Debye mechanism is expected to be active. Although the volume fraction of these local polar regions are small, the contribution of this “defect-induced” quasi-Debye mechanism might be important due to its strong contribution to the losses in comparison to the intrinsic loss mechanisms. Although the theory of the “defect-induced” quasi-Debye mechanism is not yet developed, the contribution to the losses is expected to show a strong permittivity dependence [10]:

$$\tan\delta_{dQD} \propto \varepsilon^{4.5-d} \quad (2.7)$$

where  $d=2$  for planar defects (e.g. grain boundaries),  $d=1$  for linear defects and  $d=0$  for point defects.

### 2.1.3 Dielectric response of BST thin films

For tunable applications BST is typically used in thin film form. The use of BST in thin film form has the advantage that high dc electric fields can be realized at low to moderate voltages. Thus, high tunabilities can be achieved. For example, the application of 10 V to a 300 nm thick BST thin film results in a high  $E_{dc}$  of 300 kV/cm. Due to the larger thicknesses of bulk samples, too high voltages would be required to apply high dc electric fields to the material.

The dielectric properties of BST thin films differ significantly from the ones of bulk materials. Typically, BST thin films exhibit a much lower permittivity and a broad and diffuse phase transition in comparison to bulk samples of the same composition as shown in Fig. 2.4 [23].

## 2. STATE OF THE ART - LITERATURE REVIEW

---

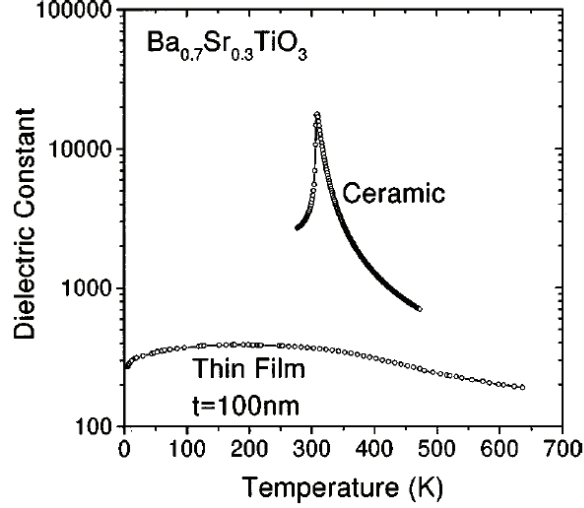


Figure 2.4: Comparison of the temperature dependence of the permittivity of a BST thin film and a corresponding bulk sample with the same composition [23].

The dielectric losses of thin films are typically one order of magnitude higher than in single crystals [10; 12]. The origins for these differences in the dielectric properties between bulk material and thin films as discussed in the literature are due to size effects, strain effects, microstructure, material chemistry, etc. Here, we will review the corresponding literature on the dielectric response of BST thin films.

### Size effects

It has been observed by many authors that BST and other high permittivity thin films characterized in the parallel-plate capacitor geometry show a thickness dependence of the film permittivity [24; 25; 26; 27]. The permittivity decreases with decreasing film thickness as illustrated in Fig. 2.5.

This thickness dependence can be described by an in-series capacitor model where low-permittivity (so-called dead or passive) layers are connected in-series with the bulk part of the high-permittivity film [27; 29; 30]. The inverse of the capacitance density ( $A/C$ ) can then be expressed as:

$$\frac{A}{C} = \frac{t - t_i}{\varepsilon_B \varepsilon_0} + \frac{t_i}{\varepsilon_i \varepsilon_0} \quad (2.8)$$

where  $A$  and  $C$  are the capacitor area and capacitance,  $t$  and  $t_i$  are the thicknesses of the film and the interfacial layer, and  $\varepsilon_B$ ,  $\varepsilon_0$ , and  $\varepsilon_i$  are the permittivities of the film bulk part, the vacuum, and the interfacial layers, respectively.

## 2.1 BST thin films for tunable applications

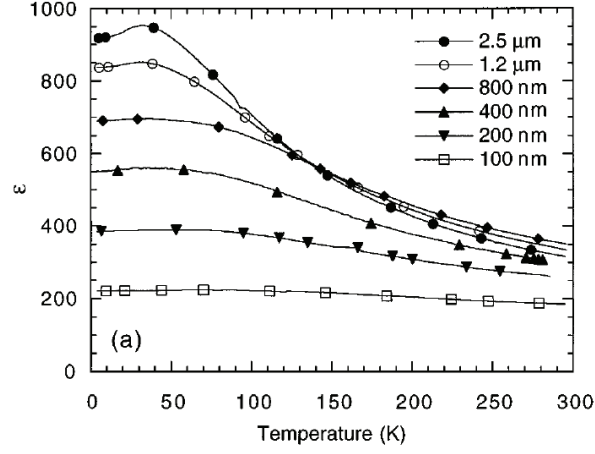


Figure 2.5: Thickness dependence of the permittivity of BST( $x=0$ ) thin films [28].

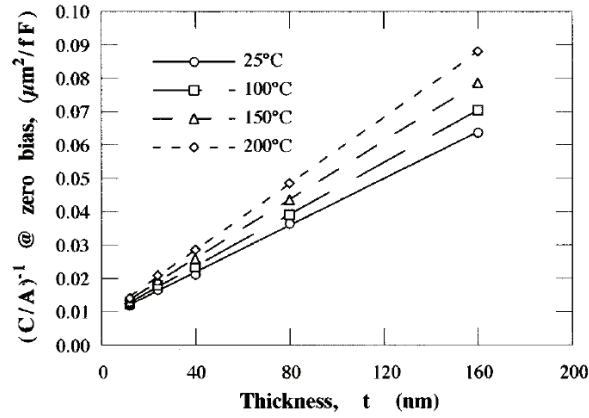


Figure 2.6: Dependence of inverse capacitance density ( $A/C$ ) on the thickness of BST( $x=0.7$ ) thin films measured at different temperatures [31].

## 2. STATE OF THE ART - LITERATURE REVIEW

---

Basceri et al. showed that a plot of  $A/C$  for BST thin films with different thicknesses resulted in straight lines with a positive intercept on the y-axis as shown in Fig. 2.6 [31]. These results indicate that, if the model is correct, the total film thickness  $t$  must be large in comparison to the thickness of the interfacial layer  $t_i$ . The data measured at different temperatures resulted in different slopes of the lines, but exhibited the same values of intercept to within the measurement precision. This means that the in-series connected interfacial capacitance must be essentially temperature independent. But, the permittivity of the film bulk changes significantly with temperature as represented from the slopes. It is believed that this temperature dependence of the bulk gives rise to the temperature dependence of the permittivity of the BST thin films. With decreasing film thickness, the influence of the interfacial layer becomes more pronounced resulting in a decrease in the permittivity and the temperature dependence of the films.

There are many potential origins for the interfacial layers discussed in the literature. These origins can be divided into intrinsic and extrinsic ones. The extrinsic origins include film/surface contamination [31], defects, nucleation layers, and heterogeneous stresses near the electrode [31], etc. The intrinsic origins include incomplete polarization screening by the metallic electrodes [32], depletion layers [10] or a near-by reduction of the polarization at the interface [33], etc.

### Strain and stress effects

The BST thin films considered for tunable applications typically exhibit a certain degree of strain. Normally, there are several factors contributing to the film strain. The most important factors are strain resulting from film crystallization, lattice mismatch, and thermal expansion mismatch between the film and the substrate. Strain effects can significantly alter the dielectric response of BST thin films. An example is the induction of ferroelectricity in paraelectric BST( $x=0$ ) thin films at room temperature due to strain effects [34].

The effect of strain on the dielectric properties of ferroelectric thin films has been addressed by Pertsev et al. [35]. They considered a (001) epitaxial film in paraelectric phase deposited on a dissimilar substrate. The film was considered as being fully relaxed at the deposition temperature. If this film is cooled down after the deposition, an in-plane deformation develops due to the differences in thermal expansion coefficients between the film  $\alpha_f$  and the substrate  $\alpha_s$ . This strain leads to a modification of the permittivity and its temperature dependence due to electrostrictive coupling. The effects are different for the in-plane  $\varepsilon_{11}$  and out-of-plane permittivity  $\varepsilon_{33}$ :

$$\varepsilon_{11}^{-1} = \varepsilon_{22}^{-1} = \varepsilon^{-1} - 2\varepsilon_0 u_m \left[ q_{11} + q_{12} - \frac{2v}{1-v} q_{12} \right] \quad (2.9)$$

$$\varepsilon_{33}^{-1} = \varepsilon^{-1} - 2\varepsilon_0 u_m \left[ 2q_{12} - \frac{2v}{1-v} q_{11} \right] \quad (2.10)$$

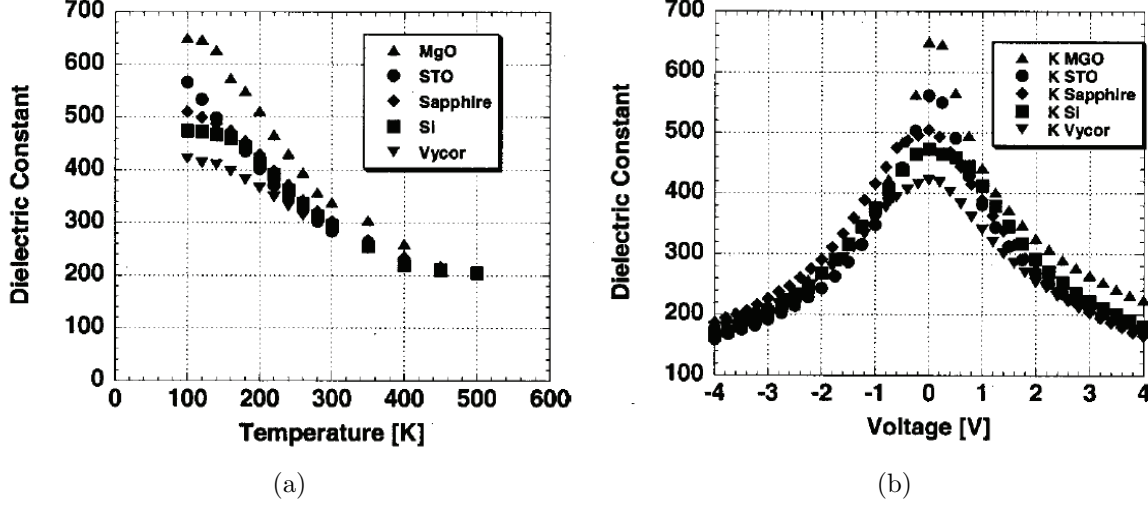


Figure 2.7: Temperature (a) and electric field (b) dependence of the permittivity of BST thin films with different thermal strains due to differences in the thermal expansion coefficients of films and substrates [36].

where  $\nu$  is the Poisson ratio,  $u_m$  is the in-plane misfit strain, and  $q_{ij}$  are the corresponding components of the tensor of linear electrostriction.

If the film obeys the Curie-Weiss law ( $\varepsilon = C/(T - T_0)$ ), a renormalization of the Curie-Weiss constant  $C$  and Curie-Weiss temperature  $T_0$  follows. Details about the formulas can be found in the paper of Pertsev et al. [35]. The results of Pertsev et al. predict an increase of the out-of-plane Curie-Weiss constant  $C_{out}$  and a decrease in the out-of-plane Curie-Weiss temperature  $T_{out}$  for an in-plane tensile thermal strain ( $\alpha_s < \alpha_f$ ). For the in-plane components  $C_{in}$  and  $T_{in}$  the behavior is opposite. For a compressive strain ( $\alpha_s > \alpha_f$ ) the behavior of all components is opposite.

The predictions of Pertsev et al. were experimentally tested by Taylor et al. [36]. They deposited BST( $x=0.24$ ) thin films on platinized substrates with different thermal expansion coefficients. Between the Pt bottom electrode and the substrate a 60 nm thick amorphous SiO<sub>2</sub> layer was deposited. The SiO<sub>2</sub> layer was deposited to achieve identical microstructures for the Pt layers on the different substrates, which resulted in identical microstructures of the BST films deposited on the different substrates. In this simple, but clever way, the influence of microstructural variations of the BST thin films on the dielectric properties could be minimized.

Figure 2.7a shows the temperature dependence of the permittivity of the BST thin films deposited on different substrates. The results confirmed the theoretical predictions of Pertsev et al. The BST film deposited on MgO substrate ( $\alpha_s > \alpha_f$ ) showed an increase of the permittivity due to an increase in  $T_{out}$  in comparison to the BST film deposited on

## 2. STATE OF THE ART - LITERATURE REVIEW

---

BST( $x=0$ ) substrate. The BST films deposited on sapphire, Si and vycor glass substrates ( $\alpha_s < \alpha_f$ ) exhibited a corresponding decrease in the permittivity, which was explained by a decrease in  $T_{out}$  in consistency with the results of Pertsev et al. The effects of the strain were also seen in the electric field dependence of the permittivity as shown in Fig. 2.7b. In general, a larger zero bias permittivity resulted in a larger tunability at a given  $E_{dc}$ .

The effect of thermal strain on the tunability of (001) textured polycrystalline BST( $x=0.5$ ) thin films was theoretically addressed by Sharma et al. [37]. Their analysis showed that the larger the difference in the thermal expansion coefficients between film and substrate and the higher the deposition temperature, the lower the tunability.

### Microstructural effects

Also the microstructure is thought to influence the dielectric response of BST thin films. Typically, a microstructure with columnar grains is observed for different deposition methods like sputtering, Pulsed Laser Deposition (PLD), and Metal Organic Chemical Vapor Deposition (MOCVD) [31; 38; 39]. The grains are of single-crystalline nature with random in-plane orientation [40]. For Chemical Solution Deposition (CSD) films a granular grain structure is often observed [41]. Since the grain boundaries are expected to have a lower permittivity than the bulk of the grain, the development of the microstructure can have a significant influence on the permittivity. For example, when considering a BST thin film with a columnar microstructure in the parallel-plate capacitor geometry, the grain boundaries are connected in parallel to the bulk of the grains, thus having a minor effect on the permittivity:

$$\varepsilon_{eff} = \varepsilon_B (1 - q) + \varepsilon_{gb} q \quad (2.11)$$

where  $\varepsilon_B$  and  $\varepsilon_{gb}$  correspond to the permittivity of the bulk grain and the grain boundary, respectively, and  $q$  is the volume fraction. Conversely, if the microstructure is granular the low permittivity grain boundaries are connected in-series with the bulk of the grain, thus reducing the permittivity of the film:

$$\frac{1}{\varepsilon_{eff}} = \frac{1 - q}{\varepsilon_B} + \frac{q}{\varepsilon_{gb}} \quad (2.12)$$

The crystallization temperature of BST thin films was studied by Noh et al. using synchrotron radiation [42]. Amorphous BST thin films were deposited on MgO substrates and annealed at temperatures up to 750 °C. For films with a thickness of about 500 nm, the perovskite phase started to nucleate in the film bulk together with a metastable intermediate phase at the interfaces at around 550 °C. The crystalline perovskite phase was observed at an annealing temperature of 650 °C. For thinner BST films, higher annealing temperatures were necessary to achieve the crystalline perovskite phase. It should be mentioned that post-annealing typically requires higher temperatures for the crystallization of thin films than direct deposition on hot substrates.

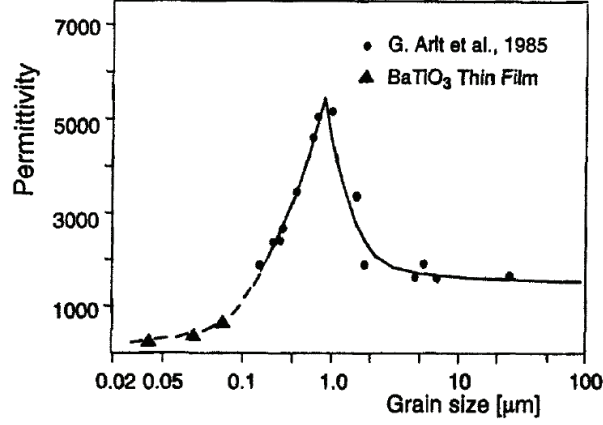


Figure 2.8: Grain size dependence of the permittivity in BST( $x=1$ ) thin films and ceramics. The data was adapted from Waser [46].

The deposition temperature of the BST films influences the film orientation [43]. For BST thin films deposited on Pt-coated Si it has been observed that an increase in the deposition and/or annealing temperature favors a (001) texture of the BST thin films [44; 45]. The orientation of the BST thin films might have an important impact on the performance of BST TFBARs (see Chapter 5). The reason is a large dependence of the BST sound velocity on the film orientation.

Also the grain size has been found to affect the dielectric response of BST thin films. Lee et al. have observed that the lateral grain size increased from 20 nm for a 25 nm thick film to 80 nm for a 300 nm thick film [47]. A grain size dependence of the permittivity has been observed in BST ceramics and thin films. The maximum permittivity in BST ( $x=1$ ) ceramics was observed at a grain size of about 700 nm. Larger or smaller grains result in a decrease in the permittivity as shown in Fig. 2.8. Horikawa et al. observed a shift of the temperature of maximum permittivity in BST thin films with decreasing grain size, which can explain the observed reduction of the room temperature permittivity of the BST thin films [48].

### Material chemistry

The materials chemistry is also known to influence the dielectric response of BST thin films. Especially, the (Ba+Sr)/Ti ratio  $y$  is of importance in this respect [49]. Stemmer et al. observed that BST thin films can accommodate much more Ti content than bulk ceramics, which they explained by the low deposition temperatures, nano-sized grains, and non-equilibrium microstructures of the films [50; 51]. Yamamichi et al. found a single perovskite BST phase for  $y$  varying from 0.75 to 1.20 in their films [52]. A peaking of

## 2. STATE OF THE ART - LITERATURE REVIEW

---

the permittivity of BST thin films was observed at or close to stoichiometry ( $y = 1$ ) with the permittivity decreasing on both sides of  $y = 1$  [52; 53]. Due to the higher zero bias permittivity stoichiometric BST thin films have a higher tunability at a given dc electric field. But, other properties are improved at off-stoichiometric compositions. For example, the maximum resistance degradation lifetime showed a maximum at  $y = 0.923$  [54]. Im et al. found a reduction of the dielectric loss and a decrease in surface roughness of the BST thin films with decreasing  $y$ , at the expense of a reduced tunability [55].

### 2.1.4 Integration of epitaxial BST thin films on silicon

The integration of epitaxial ferroelectric oxide thin films on silicon is of interest both from a fundamental and an applied point of view. The interests are due to the wide variety of optical, electronic, and magnetic properties of oxide materials that could be combined with existing semiconductor technology. This combination could increase the functionality as well as the performance of microelectronic devices. This aspect is especially true for epitaxial thin films since their higher crystallinity and lower defect density in comparison to polycrystalline films typically results in better properties and enhanced material performance [56].

For tunable applications, for example, epitaxial and single-crystalline thin films are of interest because of the potential reduction of the dielectric losses in these films. Compared to thin films, the dielectric losses in BST single crystals are about one order of magnitude lower at the frequencies of interest [10; 12]. The origin of these differences are unknown, but a reason for the higher dielectric losses in thin films could be due to imperfect film structure and defects like vacancies, dislocations, grain boundaries, etc. Another interesting aspect of epitaxial ferroelectric oxides is their strong dependence of various properties on strain and stress effects. For example, the Curie temperature  $T_c$  of BST thin films could be shifted by several hundreds of degrees due to an induced strain because of a lattice mismatch with the underlying substrate [34]. Controlling these strain effects in epitaxial films could offer enhanced material properties not realizable in other ways.

Whether epitaxial thin film growth occurs or not depends on several factors. First, the surface mobility of the arriving atoms on the substrate must be high enough so that the atoms are incorporated in the correct lattice site. Second, the lattice mismatch between the film and the substrate should be as small as possible (typically below 7-8%) and the crystal structures of the film and the substrate should be similar. Third, the film should be thermodynamically or kinetically stable against the substrate which is often called chemical matching. If a reaction between both phases occurs the condition for lattice matching is typically not fulfilled anymore and epitaxial film growth is impeded. Fourth, the difference in the thermal expansion coefficients between film and substrate should be not too big. For too large differences in the thermal expansion coefficients, film cracking due to thermal stresses is often observed after cooling the substrate down



## 2.1 BST thin films for tunable applications

---

to room temperature.

Epitaxial BST thin film growth has been realized on many different single crystal substrates like MgO [57; 58], LAO [59], LSAT [60], NdGdO<sub>3</sub> [61], DyScO<sub>3</sub> [62], etc. These substrates are typically chosen to provide good lattice matching between the film and the substrate. The thermal expansion coefficients of these substrates and BST are typically similar which allows the growth or annealing of the epitaxial thin films at high temperatures [63] which is favorable for improving the structural quality of the thin films.

Concerning the integration of epitaxial BST thin films on Si, a look at Tab 2.1 shows that good lattice matching between both phases can be realized when the BST unit cell is rotated by 45° in-plane with respect to the Si substrate. Unfortunately, it is not possible to deposit epitaxial BST directly onto silicon since the two materials react to form an amorphous phase at the film-substrate interface [64].

A possibility to solve this problem is the use of so-called buffer layers between the BST thin film and the Si substrate. These buffer layers should be chemically stable against the substrate, grow epitaxially on the Si substrate, and should provide a good lattice matching to the growing BST film. If the lattice constant of the buffer layer is between the lattice constant of the substrate and the BST film, the insertion of the buffer layer can help to increase the structural quality of the growing film by reducing the lattice mismatch.

Concerning the chemical compatibility Hubbard and Schlom investigated theoretically the stability of oxides against Si by thermodynamic analysis [65]. The thermodynamic reaction equilibrium was calculated for T=1000 K, a temperature typically used for thin film deposition. It was found that many oxides are not thermodynamically stable against Si at these high temperatures and, thus, can not be used as buffer layers (in case there is no kinetical barrier impeding a chemical reaction). According to their analysis only a limited set of binary oxides are stable against Si at typical deposition temperatures, namely MO<sub>x</sub>, where M is Li, Be, Mg, Ca, Sr, Sc, Y, Zr, Hf, Al, and, the rare earth elements.

Table 2.1 shows a selection of oxides for which (001) epitaxial thin film growth has been successful on Si(001) substrates and that are of potential interest as buffer layers for the integration of epitaxial BST thin films on Si.

The use of oxide buffer layers for the integration of epitaxial BST films is evident. Once, a thermodynamically stable interface between the buffer layer and the substrate is formed, the deposition of the BST thin film can be performed at high temperatures. Despite these advantages of oxide buffer layers, non-oxide thin films have also been successfully used as buffer layers for the integration of epitaxial oxide thin films. For these non-oxide buffer layers the same requirements as for the oxide buffer layers must be fulfilled. Table 2.1 gives a list of non-oxides that have been successfully grown epitaxially on Si and that are of interest for the integration of epitaxial BST on silicon.

Epitaxial BST thin films have been integrated on Si substrates by using single buffer layers or multilayer buffer structures. Examples for the integration with single buffer layers

## 2. STATE OF THE ART - LITERATURE REVIEW

are YSZ [66; 67; 68], SrO [69; 70], BaO [71], ZnS [72], TiN [73]. As multilayer structures CeO<sub>2</sub>/YSZ has been successfully used to integrated epitaxial BST thin films [74].

For the above mentioned examples the epitaxial BST thin films were integrated without bottom electrode. For tunable applications the parallel-plate capacitor geometry is normally preferred (see Section 2.1.5). The use of the coplanar capacitor geometry is problematic due to parasitic contributions from the substrate as discussed in Chapter 6. Therefore, it is of interest to combine the buffer layer structures with conductive layers that can serve as a bottom electrode. Here, especially conductive epitaxial oxides having a good lattice match with BST are of interest. Potential candidates for these conductive oxides are SrRuO<sub>3</sub> (SRO), (La,Sr)CoO<sub>3</sub> (LSCO), YBa<sub>2</sub>Cu<sub>3</sub>O<sub>7-x</sub> (YBCO), etc [75]. YBCO is a high temperature superconductor with a transition temperature of about 90 K [76; 77] and is therefore of interest for tunable applications at low temperatures [78].

Table 2.1: Buffer layer materials growing epitaxially with (001) orientation on Si(001).

Material	Structure	Lattice constant (a, b, c) [Å]	Lattice mismatch with Si [%]	Epitaxial relation
Si	cubic	5.43	0	
BST(x=0)	cubic	3.90	28.2; 45° rotated: 1.6	
YSZ	cubic	≈5.14	5.3	cube-on-cube
MgO	cubic	4.21	22.5	cube-on-cube
BaO	cubic	5.52	1.8	cube-on-cube
SrO	cubic	5.14	5.0	45° rotated
TiN	cubic	4.24	21.9; DME: 0.4	cube-on-cube
ZnS	cubic	5.40	0.05	cube-on-cube

There are many publications devoted to the integration of conductive epitaxial oxides on silicon [76; 79; 80; 81; 82]. But reports on the integration of epitaxial BST on these structures are rare. Boikov et al. integrated epitaxial BST thin films on YBCO/CeO<sub>2</sub>/YSZ/silicon-on-insulator [83]. The epitaxial relations of the structure for the out-of-plane and in-plane dimensions were:

- BST(001)||YBCO(001)||CeO<sub>2</sub>(001)||YSZ(001)||Si(001)
- BST[110]||YBCO[110]||CeO<sub>2</sub>[100]||YSZ[100]||Si[100]

Boikov et al. mentioned that the insertion of a BST(x=0) layer, approximately 7 nm thick, between the BST layer and the YBCO bottom electrode improved the crystallinity of the BST film and resulted in an increase of the phase transition temperature of superconductivity in the YBCO layer. The effects were attributed to reduced interdiffusion between BST and YBCO.

Another possibility to integrate epitaxial BST thin films on silicon is the use of Titanium Nitride (TiN) as a conductive buffer layer and electrode. TiN thin films can have

an electrical resistivity as low as about  $15 \mu\Omega\text{-cm}$  and can be grown epitaxially on Si [84]. Although the lattice mismatch between Si and TiN is very large (about 22%), the epitaxial film growth of TiN has been realized on Si. The reason for epitaxial growth to occur is explained by the so-called concept of Domain Matching Epitaxy (DME) in contrast to the conventional concept of Lattice Matching Epitaxy (LME) [85]. DME can occur when an integral multiples of lattice plans  $m$  of the growing film match integral multiples of lattice plans  $n$  of the substrate. In this case the lattice mismatch between the film and the substrate is efficiently reduced. For epitaxial TiN deposited on Si it has been found that 4 and 5 lattice constants of TiN match alternately 3 and 4 lattice constants of Si [86]. This reduces the effective lattice mismatch to about 0.4%, thus enabling epitaxial film growth [86].

Epitaxial BST thin film growth has been realized on TiN-buffered Si [87]. The BST and the TiN thin films were grown with a cube-on-cube epitaxial relationship on Si meaning that the films had the same in-plane and out-of-plane orientation as the substrate:

- $\text{BST}[100]||\text{TiN}[100]||\text{Si}[100]$
- $\text{BST}(001)||\text{TiN}(001)||\text{Si}(001)$

Some authors also reported other orientations of the BST layer depending on the processing conditions [88]. The growth of BST or any other oxide on TiN can lead to the oxidation of the TiN phase which would impede epitaxial film growth due to the loss of the criterion of lattice/domain matching. Thus, the deposition condition for the epitaxial growth of BST on TiN-buffered Si have to be chosen with care, as will be discussed in Chapter 7.

### 2.1.5 Applications

The most important ferroelectric component for tunable applications is the varactor which is a tunable capacitor. Due to the tunability of the BST permittivity the capacitance of the device can be changed by applying a dc bias. There are basically two types of tunable capacitors, namely the parallel-plate and the coplanar capacitor. Cross sections of these device types are shown in Fig 2.9.

In the parallel-plate capacitor geometry the dc bias is applied across the thickness of the BST thin film and as a result low to moderate dc voltages are enough for effective tuning. Because of the high permittivity and the small thickness of the BST thin film in this geometry, the capacitor typically shows a rather large capacitance of up to 10 pF. This can be problematic for high-frequency applications due to issues like impedance matching and electrical resonances. Moreover, in the parallel-plate geometry the loss contribution from the electrodes is much more pronounced than in the coplanar capacitor geometry.

In the coplanar capacitor geometry, the electric field is applied along the BST film across the gap formed by the two electrodes. Typically, the gap width is larger than the

## 2. STATE OF THE ART - LITERATURE REVIEW

---

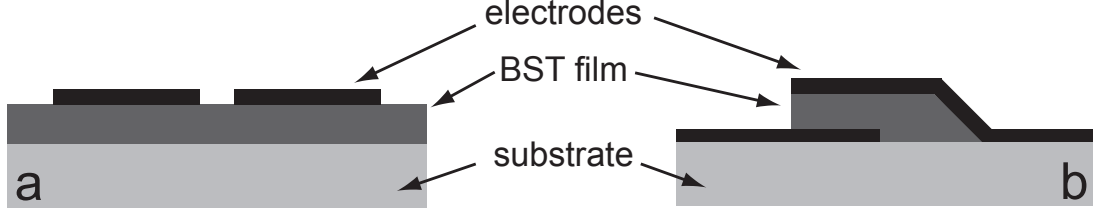


Figure 2.9: Coplanar (a) and parallel-plate (b) capacitor geometries.

thickness of the BST films in the parallel-plate geometry and, thus, higher dc voltages are required to apply a certain dc electric field. The capacitances are typically lower (up to 1 pF) than for the parallel-plate geometry and the loss contribution from the electrodes is less pronounced.

The varactors are typically integrated with other components to build tunable devices. Examples include tunable filters [89; 90], voltage controlled oscillators [91], and phase shifters [92].

In this thesis a new type of tunable device based on BST thin films has been developed, which is the tunable TFBAR.

### 2.2 Piezoelectricity induced by a dc bias through the electrostrictive effect

Electrostriction is a property shown by all materials. It describes the nonlinear coupling of electric and elastic fields [93]:

$$u_{ij} = Q_{ijkl} P_k P_l \quad (2.13)$$

where  $u_{ij}$  and  $Q_{ijkl}$  are the corresponding components of the tensors of strain and electrostriction, respectively, and  $P_i$  is the polarization. Typically, the electrostrictive effect is strong in materials showing a large polarization response like ferroelectrics and relaxor-ferroelectrics [94; 95].

If a dc and an ac electric field are applied to a non-piezoelectric material, Eq. (2.13) can be written as:

$$u = Q(P_{dc} + P_{ac})^2 = QP_{dc}^2 + 2QP_{dc}P_{ac} + QP_{ac}^2 \quad (2.14)$$

where  $P_{dc}$  and  $P_{ac}$  correspond to the dc and ac parts of the polarization. In Eq. (2.14) we omitted the indices of the tensor components for simplicity of notation. The term  $(2QP_{dc})P_{ac}$  in Eq. (2.14) behaves like a piezoelectric effect meaning that the strain is

a linear function of the ac field and changes its sign with a change in the direction of the ac field. This means that all materials show an induced piezoelectric effect under dc bias [95]. If the problem is addressed from a point of view of symmetry, one can say that the application of a dc electric field to a centrosymmetric material leads to a displacement of the ions in the material's unit cell. This displacement results in a break of the central symmetry of the materials crystal structure. Thus, the material becomes non-centrosymmetric under dc bias and shows therefore piezoelectric activity.

Like mentioned in Section 2.1.2 tuning of the permittivity of BST is achieved by applying a dc electric field. This application of a dc electric field results in piezoelectric activity in the material. A piezoelectric material that is sandwiched between 2 electrodes shows acoustic resonances at a certain frequency of the ac field depending mainly on the thickness and the sound velocity of the material. Acoustic resonances in BST thin film parallel-plate capacitors have been observed under dc bias [15; 16]. The resonances were observed in the capacitance-frequency (and/or loss tangent-frequency) curves. It was observed that the acoustic resonances became more pronounced with increasing dc bias. It was also stated that the frequencies of the acoustic resonances are independent from the dc electric field and thus, cannot be tuned [15; 16]. Contrariwise, Gevorgian et al. filed a patent on a tunable resonator, where the dc bias induced acoustic resonances can be tuned by varying the dc electric field [18].

In this thesis we will demonstrate that the acoustic resonances in a BST thin film can be tuned by a dc bias. The effect can be used to develop tunable TFBARs. This idea is addressed in this thesis in Chapters 3 and 5.

## 2.3 Introduction to TFBAR technology

TFBARs are devices based on piezoelectric thin films. There are two resonator geometries, namely the parallel-plate geometry where the resonator operates in the thickness excitation (TE) mode, and the coplanar geometry where the resonator operates in the lateral field excitation (LFE) mode. Resonators working in the TE mode are by far the most common ones.

For a TE mode resonator acoustic resonances appear at a certain frequency of the applied ac electric field depending mainly on the thickness and the sound velocity of the layers building the TFBAR device. A reduction in the thickness of the resonator results in an increase of the frequencies of the acoustic resonances for a given device. For typical piezoelectric materials used in TFBAR technology acoustic resonances at frequencies from 1 to 10 GHz correspond roughly to a thickness of about 0.5 to 5  $\mu\text{m}$ . Thus, piezoelectric thin films are very attractive for frequencies above 1 GHz whereas the thinning down of single crystals to such low thicknesses is not [96].

At resonance the electrical impedance of the device changes from a low value (typically about 1  $\Omega$ ) at the resonance frequency  $f_{res}$  to a high value (typically about 1000  $\Omega$ ) at the

## 2. STATE OF THE ART - LITERATURE REVIEW

---

antiresonance frequency  $f_{ares}$  [97]. The effective electromechanical coupling factor  $k_{eff}^2$  of the device depends on the separation between both frequencies:

$$k_{eff}^2 = \frac{\pi}{2} \frac{f_{res}}{f_{ares}} \frac{1}{\tan\left(\frac{\pi}{2} \frac{f_{res}}{f_{ares}}\right)} \quad (2.15)$$

If the electromechanical coupling in the piezoelectric material is weak,  $k_{eff}^2$  can be calculated as:

$$k_{eff}^2 = \frac{\pi^2}{4} \frac{f_{ares} - f_{res}}{f_{ares}} \quad (2.16)$$

The  $k_{eff}^2$  is dependent on the electromechanical coupling factor  $k_t^2$  of the piezoelectric material as well as on device design.

As piezoelectric materials, Aluminium Nitride (AlN) and Zinc Oxide (ZnO) are typically used [98; 99]. Both materials (AlN and ZnO) have a sufficiently high  $k_t^2$ , can be grown with a high structural film quality, and exhibit good acoustic material properties. Other piezoelectric materials like PZT are also of interest [100; 101; 102], but are problematic because of poor acoustic material properties and low film quality [103].

Beside  $k_{eff}^2$ , the Q-factor of the resonator is an important device property. The Q-factor of the device gives a measure of the dissipated energy in the system. It can be defined as the ratio of the stored energy to the dissipated energy during the period of the ac field in the device. The resonator Q-factor is of importance as it affects many of the performance characteristics of the system in which the resonator is used. The higher the Q-factor, the higher the amplitude of the vibration and the sharpness of the resonance peak. The Q-factor can be calculated from the slope of the impedance phase  $\phi$  at the resonance or antiresonance frequency. At the resonance frequency the Q-factor is:

$$Q = \frac{f_{res}}{2} \frac{\partial \phi}{\partial f} \bigg|_{f_{res}} \quad (2.17)$$

where  $f$  is the frequency. The Q-factor of a device is in principle affected by several factors including device design, the electrical resistance of the electrodes and other parasitic effects as well as acoustic losses in the materials used in the device.

To excite high-quality (high-Q) acoustic resonances, the energy of the traveling acoustic wave must be confined in the active area of the resonator. This is achieved by isolating the active area of the resonator from the substrate preventing propagation of the acoustic wave into the substrate and providing appropriate boundary conditions. For TFBARs this isolation is realized either by removing the substrate under the active area of the device or by removing a priorly deposited sacrificial layer under the active area [104]. Another way to achieve an acoustic isolation from the substrate has been demonstrated by using a Bragg reflector in Solidly Mounted Resonators (SMR) [104]. Here, alternating layers of high and low mechanical impedance and of quarter wavelength thickness are deposited under the active area of the resonators. The acoustic wave is reflected at the interface

between the layers of the Bragg reflector preventing its penetration into the substrate and thus, minimizing acoustic losses.

TFBARs are of interest for several applications. The sensitivity of the resonance frequency on a mass loading effect led to the development of various sensors based on TFBARs [105; 106; 107]. The high Q-factor at high frequencies above 1 GHz enabled the use of TFBARs in Voltage Controlled Oscillators (VCOs) [106]. The change from a low to a high impedance state at close-by frequencies makes resonators attractive for filter applications [96; 108; 109]. By combining several resonators a passband can be designed. In the passband the signals can pass whereas outside of the passband the signals are rejected. Several types of filters have been proposed [110]. Electronic filters have been commercially available since the late 1990's [111; 112; 113].

### 2.3.1 1-dimensional model for acoustic resonances in piezoelectric plates

The lateral dimensions of a typical TFBAR are much larger than the thickness of the device. Thus, the device can be considered as 1-dimensional for the purpose of wave propagation.

#### TE-mode

We consider a piezoelectric plate with thickness  $t$  sandwiched between two electrodes of area  $A$  as shown in Fig. 2.10a. The electrodes in the model are considered as being infinitely thin, of zero mass, and lossless. The piezoelectric plate is laterally clamped, but free to move in the out-of-plane  $z$  direction. This means that the strain component  $u_{33} \neq 0$ . For the TE mode the electric displacement  $D$  and the strain  $u$  are typically chosen as independent variables, and the stress  $\sigma$  and the electric field  $E$  are dependent variables. In this case, the constitutive piezoelectric equations (written in Voigt Notation) are:

$$\sigma_3 = c_{33}^D u_3 - h_{33} D_3 \quad (2.18)$$

$$E_3 = \frac{1}{\varepsilon_{33}^u} D_3 - h_{33} u_3 \quad (2.19)$$

where  $c_{33}^D$ ,  $\varepsilon_{33}^u$ , and  $h_{33}$  are the elastic constant at constant  $D$ , the permittivity at constant  $u$ , and the piezoelectric stress constant, respectively. The displacement  $d$  of the longitudinal traveling wave follows the wave equation:

$$\frac{\partial^2 d}{\partial z^2} = \frac{\rho}{c_{33}^D} \frac{\partial^2 d}{\partial t^2} \quad (2.20)$$

where  $\rho$  is the density. Considering a plane wave, the following “Ansatz” can be used:

$$d(z, t) = B \sin(kz) e^{i\omega t} \quad (2.21)$$

## 2. STATE OF THE ART - LITERATURE REVIEW

---

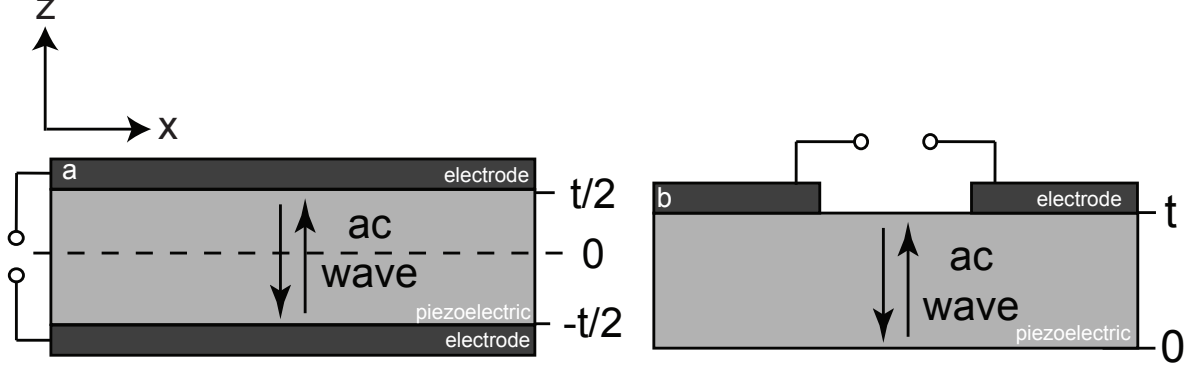


Figure 2.10: Cross sections of piezoelectric plates resonating in the TE mode (a) and the LFE mode (b).

where  $k$  is the propagation constant and  $\omega$  is the angular frequency. The propagation constant  $k$  is defined as:

$$k = \frac{\omega}{v^D} \quad (2.22)$$

where  $v^D$  is the sound velocity in the piezoelectric material under constant  $D$ . Using the mechanical boundary conditions ( $\sigma_3=0$  at  $z=-t/2$  and  $z=t/2$ ), and noting that  $u_3 = \partial d/\partial z$  the constant  $B$  can be found using Eq. (2.18):

$$B = \frac{h_{33}D_3}{c_{33}^D k \cos(kt/2)} \quad (2.23)$$

Combining Eqs. (2.23), (2.21) and (2.19) and bearing in mind that  $u_3 = \partial d/\partial z$ , the voltage across the piezoelectric can be calculated by integration of Eq. (2.19) over the plate thickness:

$$V = \int_{-t/2}^{t/2} E_3 dz = \frac{D_3 h}{\varepsilon_{33}^u} \left( 1 - k_t^2 \frac{\tan(kt/2)}{kt/2} \right) \quad (2.24)$$

where

$$k_t^2 = h_{33}^2 \frac{\varepsilon_{33}^u}{c_{33}^D} \quad (2.25)$$

is the electromechanical coupling factor of the piezoelectric material for the TE mode. The current  $I$  through the piezoelectric film can be calculated with the electric charge  $Q(t) = AD_3(t)$  on the electrodes:

$$I = \frac{\partial Q}{\partial t} = i\omega t AD_3 \quad (2.26)$$



Thus, the impedance  $Z$  or admittance  $Y = 1/Z$  can be calculated:

$$Z(\omega) = Y^{-1}(\omega) = \frac{V}{I} = \frac{1}{i\omega C_0} \left( 1 - k_t^2 \frac{\tan\left(\frac{kt}{2}\right)}{\frac{kt}{2}} \right) \quad (2.27)$$

where  $C_0$  is the clamped capacitance:

$$C_0 = \frac{A\varepsilon^u}{t} \quad (2.28)$$

The resonance  $f_{res}$  and antiresonance  $f_{ares}$  frequencies are defined at  $Z$  being zero and infinite, respectively. Using Eq. (2.27) they can be expressed as:

$$f_{ares} = \frac{1}{2t} \sqrt{\frac{c_{33}^D}{\rho}} = \frac{v^D}{2t} \quad (2.29)$$

$$f_{res} = \frac{1}{2\pi t} \sqrt{(\pi^2 - 8k_t^2) \frac{c_{33}^D}{\rho}} \quad (2.30)$$

### LFE mode

For the LFE mode we consider a piezoelectric plate with thickness  $t$  with two coplanar electrodes as shown in Fig. 2.10b. The electrodes have a width  $W$  and are separated by a gap  $g$ . The electrodes in the model are considered as being infinitely thin, of zero mass, and lossless. The piezoelectric plate is laterally clamped, but free to move in the out-of-plane  $z$  direction. This means that the strain component  $u_{33} \neq 0$ .

The constitutive piezoelectric equations (written in Voigt Notation) are:

$$\sigma_3 = c_{33}^E u_3 - e_{13} E_1 \quad (2.31)$$

$$D_1 = \varepsilon_{11}^u E_1 - e_{13} u_3 \quad (2.32)$$

where  $e_{13}$  is the piezoelectric stress coefficient. Taking the mechanical boundary conditions and the mechanical wave equation like in the TE mode into account, the current  $I$  and the voltage  $V$  can be calculated:

$$I = i\omega W \int_0^t D_1 dz \quad (2.33)$$

$$V = E_1 g \quad (2.34)$$

## 2. STATE OF THE ART - LITERATURE REVIEW

---

The impedance  $Z$  or admittance  $Y = 1/Z$  can be calculated with Eqs. (2.33) and (2.34):

$$Y(\omega) = Z^{-1}(\omega) = i\omega C_0 \left( 1 + k_{lat}^2 \frac{\tan\left(\frac{kt}{2}\right)}{\frac{kt}{2}} \right) \quad (2.35)$$

where

$$k_{lat}^2 = \frac{e_{13}^2}{c_{33}^E \varepsilon_{11}} \quad (2.36)$$

is the electromechanical coupling factor of the piezoelectric plate in the LFE mode. The clamped capacitance  $C_0$  is:

$$C_0 = \frac{W\varepsilon g}{t} \quad (2.37)$$

The conditions for the resonance and antiresonance frequency in the LFE mode are:

$$f_{res} = \frac{1}{2t} \sqrt{\frac{c_{33}^E}{\rho}} = \frac{v^E}{2t} \quad (2.38)$$

$$f_{ares} = \frac{1}{2\pi t} \sqrt{(\pi^2 - 8k_{lat}^2) \frac{c_{33}^E}{\rho}} \quad (2.39)$$

where  $v^E$  is the sound velocity in the piezoelectric plate at constant  $E$ .

### 2.3.2 Tuning of TFBARs

A tunable TFBAR is a device where the resonance and/or antiresonance frequency can be altered in a controlled way. There are several reasons for the interest in tunable TFBARs. For example, the tunability of the TFBAR could be used to compensate for temperature drifts and aging effects. Also, the post-fabrication adjustment of the resonance frequencies is of interest. Since the resonance frequencies depend on the thickness of the device, a thickness inhomogeneity of the different layers across the wafer results in some variation of the resonance frequencies. This problem has been addressed by adding or removing material to or from the active area of the device. This affects the mass loading of the device which changes the resonance frequencies [114]. This kind of passive tuning can only be done once. Probably the highest interest in tunable TFBAR is due to the potential to fabricate tunable filters for communication system. In the ideal case, the passband of a filter could be tuned over a large frequency range [115]. Thus, the filter could be adapted to work in different frequency bands. This is of special importance for handheld devices since the number of components could be reduced in this way, which would decrease weight and cost of the devices while saving space at the same time.

Tuning of TFBARs based on AlN or ZnO films has been realized by temperature tuning [116; 117], application of a dc bias [118; 119], and by connecting additional tunable components like varactors or tunable inductors to the TFBAR [120; 121].

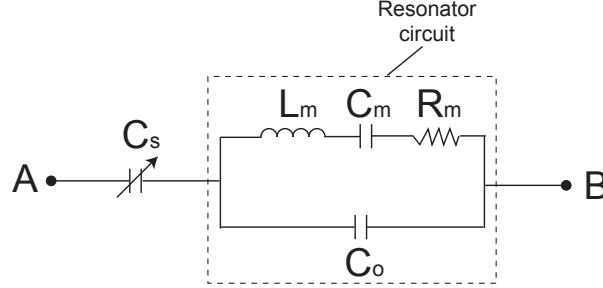


Figure 2.11: Equivalent circuit of a resonator with an in-series connected tunable capacitor. The dashed rectangle shows the equivalent circuit of a resonator.

Ruby and Merchant investigated the possibility of temperature tuning [116]. The elastic constant of a material typically shows a small dependence on temperature, which results in a variation of the sound velocity in this layer. Thus, the resonance frequencies also change with temperature. Typically, one tries to reduce this temperature coefficient. Ruby and Merchant tried to use this temperature coefficient by adding a heating layer, a so-called microheater, around the active area of the resonator. The maximum temperature achievable was estimated to be about 580 °C. Such high temperatures distorted the membrane of the TFBAR and resulted in film cracking. Nevertheless, the temperature coefficient of their device was up to 78 ppm/K. Thus, a temperature change of 100 °C should result in a change of the resonance frequency of about 7800 ppm.

The effect of applying a dc bias to tune the resonator has been investigated by several groups [116; 118; 122]. The change of the resonance frequencies per V of the applied dc bias is called the voltage coefficient VCF. Typically a VCF of some tens of ppm/V is observed [118; 122]. The tuning under dc bias can be attributed to two effects [122]. Through the inverse piezoelectric effect the thickness changes, which results in a modification of the resonance frequency. Lanz estimated this effect to account for about 7.5 ppm/V of the VCF [122]. The other, and stronger effect is due to electrostriction. The electrostrictive effect leads to a stiffening of the elastic constant  $c$  which alters the sound velocity of the piezoelectric layer and thus, the resonance frequencies of the device.

The tuning ranges for the mechanisms discussed above are rather small being in the ppm-range for materials like AlN and ZnO. Another possibility to tune the resonance frequencies of a TFBAR is to connect it with tunable components like varactors or tunable inductors [120; 121; 123]. The equivalent circuit for a resonator with a tunable capacitor connected in-series is shown in Fig. 2.11.

Here,  $L_m$ ,  $C_m$ , and  $R_m$  build the motional arm of the resonating mode.  $C_s$  and  $C_0$  correspond to the capacitance of the in-series connected varactor and the clamped capacitance of the resonator, respectively.

## 2. STATE OF THE ART - LITERATURE REVIEW

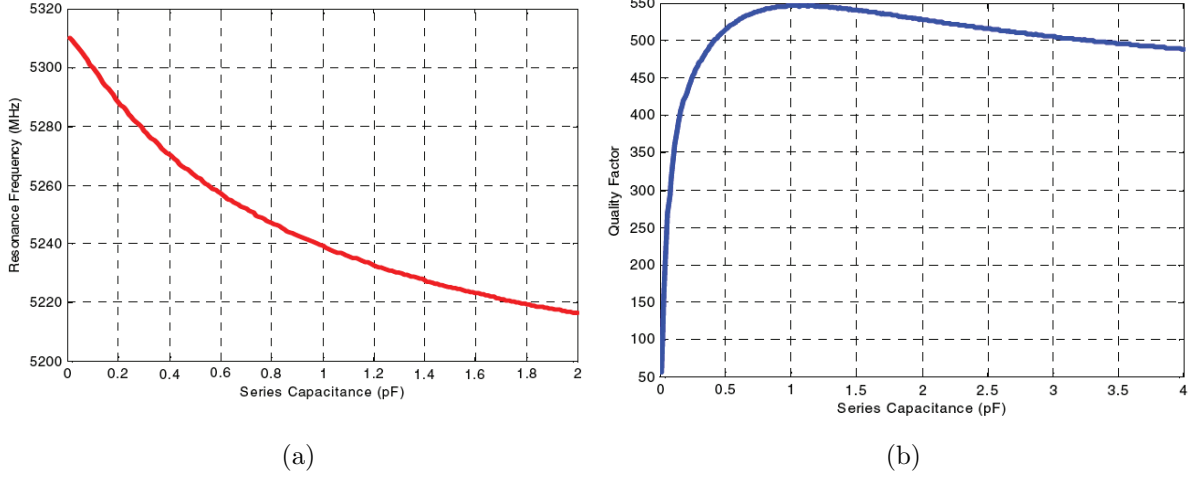


Figure 2.12: Dependence of the resonance frequency (a) and the Q-factor (b) of a ZnO TFBAR on the capacitance  $C_s$  of an in-series connected varactor [115].

According to Pang et al. the resonance and antiresonance frequency of such a device can be determined as [115]:

$$f_{res} = \frac{1}{2\pi} \sqrt{\frac{1 + \frac{C_m}{C_0 + C_s}}{L_m C_m}} \quad (2.40)$$

$$f_{ares} = \frac{1}{2\pi} \sqrt{\frac{1 + \frac{C_m}{C_0 + \frac{C_s C_p}{C_s + C_p}}}{L_m C_m}} \quad (2.41)$$

where  $C_p$  being the parasitic capacitance from the substrate was taken into account. As can be seen from Eqs. (2.40) and (2.41) a change in  $C_s$  alters the resonance and antiresonance frequencies with the effect being stronger for the resonance frequency. A decrease of  $C_s$  as observed for a MEMS varactor under dc bias, increases the resonance frequency bringing both resonance frequencies closer together. Thus,  $k_{eff}^2$  is reduced. The maximum tuning range is defined by the difference in resonance and antiresonance frequency and is therefore dependent on  $k_{eff}^2$ . For a TFBAR with  $k_{eff}^2=6\%$  the maximum tuning range will be  $\approx 2.4\%$  [121]. Figure 2.12 shows simulations of the dependence of resonance frequency and the Q-factor on the capacitance of the in-series connected varactor [115]. It can be seen that a large tuning of the varactor is needed to achieve an appreciable tuning of the resonance frequency. If the capacitance of the series varactor is small ( $C_s < 0.5$  pF), the Q-factor of the resonator decreases dramatically.

Pang et al. fabricated a ZnO TFBAR with a tunable MEMS air-gap capacitor connected in-series [115]. The series varactor showed only a continuous tuning range of 1.5:1 due to pull-in at higher dc voltages. The tuning of the TFBAR was about 0.8%

## 2.3 Introduction to TFBAR technology

---

( $\Delta f=18$  MHz) for a resonance frequency of about 2.3 GHz and a dc bias of 27.5 V. This tuning range was about 6 times larger than the one typically achieved by the electrostrictive effect as mentioned above. The Q-factor of the device was less than 50.



## Chapter 3

# Theory of electrical tuning of dc bias induced acoustic resonances in paraelectric thin films

In this chapter we develop a theory of the electrical tuning of dc bias induced acoustic resonances in paraelectric thin films. The theory is based on the Landau free energy  $P$ -expansion and takes linear and non-linear electrostrictive effects and the background permittivity into account.

### 3.1 Introduction

Thin film bulk acoustic wave resonators (TFBARs) are devices based on piezoelectric thin films. Typically, piezoelectric thin films of AlN [124; 125] or ZnO [99; 126] being sandwiched between two electrodes are used. The device resonates at a certain frequency of the applied ac signal depending on the acoustic velocity and the thickness of the different layers building the device. This resonance phenomenon is useful for many applications like in filters, sensors, etc.

Piezoelectricity occurs in materials belonging to non-centrosymmetric point groups with the non-centrosymmetric point groups 432 and  $\infty\infty$  being exceptions. Materials belonging to centrosymmetric point groups do not show piezoelectricity. However, all materials, centrosymmetric as well as non-centrosymmetric, show electrostriction. The electrostrictive effect describes the nonlinear coupling of elastic and electric fields [93]. If a dc electric field is applied to a centrosymmetric material, the central symmetry of the material's crystal structure is broken. Therefore, the material becomes piezoelectric due to the electrostrictive effect as described in Chapter 2.2 [95].

Thin films of BST being in the paraelectric (centrosymmetric) phase are considered for frequency agile applications due to the dc bias dependent permittivity of the material [10;

### 3. THEORY OF ELECTRICAL TUNING OF DC BIAS INDUCED ACOUSTIC RESONANCES IN PARAELECTRIC THIN FILMS

---

14; 89; 127]. If a dc bias is applied to tune the permittivity of the material, the central symmetry of the BST crystal structure is broken and piezoelectricity is induced. Field induced acoustic resonances have been observed in parallel-plate [15; 128; 129] as well as in interdigital [130; 131] BST thin film capacitors under dc bias. This is a critical issue from the point of view of applications because the capacitance and the loss tangent show instabilities at the resonance frequency. However, it was found that the dc bias induced resonance phenomenon depends on the applied dc electric field and is therefore also tunable [17]. This phenomenon can be used to develop voltage-controlled tunable resonators [132; 133] and filters [134].

Recently, the phenomenon of the dc bias dependence of acoustic resonances in BST thin films was theoretically addressed by Vendik et al. [135]. They treated the problem by deriving the field dependent constitutive equations from the free energy D-expansion. According to their theory, the main contribution to the tuning of the acoustic resonances is attributed to the tensor of nonlinear electrostriction  $m$ . The signs of the shifts of both resonance and antiresonance frequencies are determined by the sign of the corresponding component of  $m$ .

In this chapter we present a theoretical model for the dc electric field induced and dc bias dependent resonance phenomenon in centrosymmetric (paraelectric) films. We discuss the case of high permittivity materials, namely BST, being of interest for tunable applications, although the model is also valid for other paraelectric materials. The model is based on the Landau free energy  $P$ -expansion by taking linear and nonlinear electrostrictive effects as well as the background permittivity  $\epsilon^b$  into account. Two different modes of excitation of the acoustic resonances, namely the thickness excitation (TE) and the lateral field excitation (LFE) modes, are considered. For the TE mode the model predicts a much stronger dc bias dependence for the resonance frequency than for the antiresonance frequency. In the LFE mode both resonance and antiresonance frequencies may exhibit comparable dc bias dependencies with the antiresonance frequency being more strongly dc bias dependent. We calculated the relevant tensor components controlling the tuning of the resonance and antiresonance frequencies for different BST compositions and film orientations from the available literature data. The senses and the amounts of the dc bias dependent frequency shifts are discussed for both modes of excitation.

## 3.2 Derivation of the field dependent piezoelectric constitutive equations

In this section we derive the field dependent piezoelectric constitutive equations being valid for the TE and the LFE mode. The case of a ferroelectric in paraelectric phase is



### 3.2 Derivation of the field dependent piezoelectric constitutive equations

considered. We start with the Landau free energy  $P$ -expansion:

$$F = \frac{\alpha_{ij}}{2} P_i P_j + \frac{\beta_{ijkl}}{4} P_i P_j P_k P_l + \frac{1}{2} c_{ijkl}^0 u_{ij} u_{kl} - q_{ijkl} u_{ij} P_k P_l - \frac{1}{2} m_{ijklmn} u_{ij} u_{kl} P_m P_n \quad (3.1)$$

where  $P_i$  is the ferroelectric part of the polarization,  $\beta_{ijkl}$  is the tensor of dielectric non-linearity and  $c_{ijkl}^0$ ,  $u_{ij}$ ,  $q_{ijkl}$ , and  $m_{ijklmn}$  are the tensors of the elastic constant at constant  $P$ , strain, linear electrostriction, and nonlinear electrostriction, respectively. The tensor component  $\alpha_{ij}$  is given by:

$$\alpha_{ij} = \left( \chi_{ij}^{f_0} \right)^{-1} \quad (3.2)$$

where  $\chi_{ij}^{f_0}$  is the ferroelectric contribution to the susceptibility of the material at zero bias ( $E^{dc} = 0$ ).

The constitutive equations can be found by the relations:

$$\frac{\partial F}{\partial P_i} = E_i \quad (3.3)$$

$$\frac{\partial F}{\partial u_{ij}} = \sigma_{ij} \quad (3.4)$$

$$D_i = \varepsilon^b E_i + P_i \quad (3.5)$$

where  $E_i$  is the electric field,  $\sigma_{ij}$  is the stress tensor and  $\varepsilon^b$  is the background permittivity. The background permittivity comprises all non-ferroelectric contributions to the permittivity of the material. In ferroelectric materials  $\varepsilon^b/\varepsilon_0$  is expected to be of the order of the relative permittivity in non-ferroelectric materials where  $\varepsilon_0$  is the vacuum permittivity. For BST(x=1)  $\varepsilon^b/\varepsilon_0$  is estimated to be around 7 [136]. We are interested in the electromechanical behavior of the system in the case where it is under the action of a dc electric field  $E^{dc}$  superimposed with a relatively small electric field  $E^{ac}$ , i.e.  $E^{dc} \gg |E^{ac}|$ . In this case, we will present all variables of the problem as sums of larger dc and small ac components as follows:

$$E^{tot} = E^{dc} + E^{ac} \quad (3.6)$$

$$P^{tot} = P^{dc} + P^{ac} \quad (3.7)$$

$$\sigma^{tot} = \sigma^{dc} + \sigma^{ac} \quad (3.8)$$

$$u^{tot} = u^{dc} + u^{ac} \quad (3.9)$$

By linearization of the constitutive equations (3.3) and (3.4) with respect to the ac components in Eqs. (3.6) to (3.9), the field dependent piezoelectric constitutive equations can be derived:

$$E_i = \left( \chi_{ij}^f \right)^{-1} P_j - h_{ikl} u_{kl} \quad (3.10)$$

$$\sigma_{ij} = c_{ijkl}^P u_{kl} - h_{kij} P_k \quad (3.11)$$

### 3. THEORY OF ELECTRICAL TUNING OF DC BIAS INDUCED ACOUSTIC RESONANCES IN PARAELECTRIC THIN FILMS

---

For simplicity of notation, we have dropped the suffix “ac” from the ac parts. The piezoelectric tensor  $h_{ikl}$ , the ferroelectric contribution to the susceptibility of the material  $\chi_{ij}^f$  and the tensor of elastic constant  $c_{ijkl}^P$  at constant  $P$  can be presented as functions of the polarization  $P^{dc}$  induced by the dc electric field:

$$h_{ijk} = 2q_{iskl}P_s^{dc} \quad (3.12)$$

$$c_{ijkl}^P = c_{ijkl}^0 - m_{ijklmn}P_m^{dc}P_n^{dc} \quad (3.13)$$

Here,  $c_{ijkl}^0$  is the tensor of the electric constant of the material in the absence of the tuning electric field and in Eqs. (3.12) and (3.13) we have kept only lower order terms in  $P^{dc}$ .

The polarization induced by the dc field  $P^{dc}$  and the ferroelectric contribution to the susceptibility of the material  $\chi_{ij}^f$  loaded with this field can be determined from Eqs. (3.3) and (3.4) after elimination of the elastic variables. Keeping the lowest non-linear terms this equation can be written as:

$$E_i^{dc} = \alpha_{ij}^*P_j^{dc} + \beta_{ijkl}^*P_j^{dc}P_k^{dc}P_l^{dc} \quad (3.14)$$

where the coefficients  $\alpha_{ij}^*$  and  $\beta_{ijkl}^*$  depend on the mechanical conditions of the system. Explicit expressions for the components of these tensors for (100) and (111) thin films clamped on the substrate (the situation treated further in this chapter) can be found in Ref. [137; 138]. This equation leads to the following for  $\chi_{ij}^f$ :

$$\left(\chi_{ij}^f\right)^{-1} = \alpha_{ij}^* + 3\beta_{ijkl}^*P_k^{dc}P_l^{dc} \quad (3.15)$$

The set of variables can be changed from “ $P, u \rightarrow E, \sigma$ ” to “ $E, u \rightarrow D, \sigma$ ” to express the field dependent piezoelectric constitutive equations (3.10) and (3.11) in the standard form for TFBAR considerations:

$$D_i = \varepsilon_{ij}E_j + e_{ijk}u_{jk} \quad (3.16)$$

$$\sigma_{ij} = c_{ijkl}^E u_{kl} - e_{kij}E_k \quad (3.17)$$

where the tensor of the clamped permittivity  $\varepsilon_{ij}$ , the tensor of the elastic constant  $c_{ijkl}^E$  for constant  $E$  and the tensor of the piezoelectric coefficient  $e_{ijk}$  are given by the relations:

$$\varepsilon_{ij} = \varepsilon_{ij}^b + \chi_{ij}^f \quad (3.18)$$

$$c_{ijkl}^E = c_{ijkl}^0 - m_{ijklmn}P_m^{dc}P_n^{dc} - h_{pij}\chi_{pq}^f h_{qkl} \quad (3.19)$$

$$e_{ijk} = \chi_{is}^f h_{sjk} \quad (3.20)$$

### 3.3 Field dependence of the acoustic resonances (TE mode)

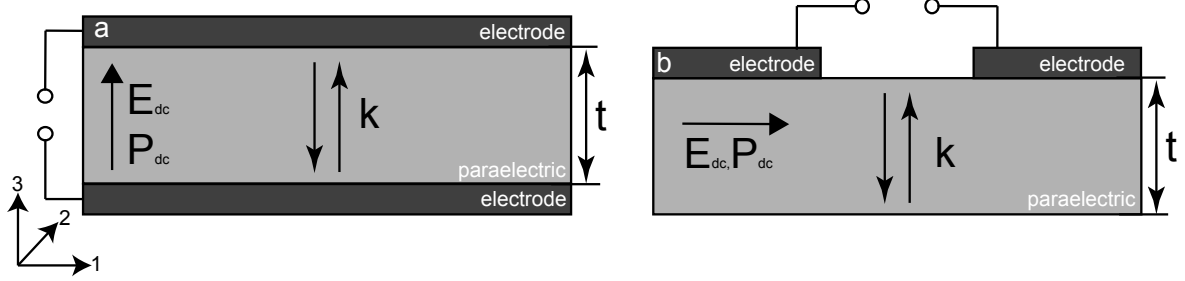


Figure 3.1: Schematic drawings of the considered resonator geometries. For the TE mode a parallel-plate capacitor geometry as shown in (a) is considered. In this case the polarization  $P^{dc}$  is parallel to the direction of the traveling acoustic wave indicated by the wave vector  $k$ . The coplanar capacitor shown in (b) corresponds to the LFE mode. Here, the polarization  $P^{dc}$  is perpendicular to the direction of the traveling acoustic wave.

### 3.3 Field dependence of the acoustic resonances (TE mode)

To excite the acoustic resonances in the TE mode, the geometry of a parallel-plate capacitor as shown in Fig. 3.1a is considered. We consider the acoustic resonances associated with a longitudinal acoustic wave traveling in the thickness direction, which we take for the direction of the Cartesian  $X_3$  axis. The following consideration is valid if a pure longitudinal acoustic wave is possible for this direction. For cubic paraelectric materials like BST this condition is met for epitaxial or textured films of (001), (111), and (110) orientations and polycrystalline films. Because of the geometry of the problem only the  $X_3$  components of the dc and ac electric fields become relevant. The film is considered to be clamped in the in-plane direction and free in the out-of plane direction. The electrodes are considered as being of zero mass.

The field dependent constitutive equations for the TE mode can be written in Voigt notation:

$$D_3 = \varepsilon_{33}E_3 + e_{33}u_3 \quad (3.21)$$

$$\sigma_3 = c_{33}^E u_3 - e_{33}E_3 \quad (3.22)$$

with

$$e_{33} = \chi_3^f h_{33} \quad (3.23)$$

$$c_{33}^E = c_{33}^0 - m_{333} (P_3^{dc})^2 - h_{33} \chi_3^f h_{33} \quad (3.24)$$

From Eqs. (3.21) and (3.22) the admittance  $Y$  (or impedance  $Z$ ) can be derived by taking the mechanical wave equation, mechanical boundary conditions and the Poisson equation

### 3. THEORY OF ELECTRICAL TUNING OF DC BIAS INDUCED ACOUSTIC RESONANCES IN PARAELECTRIC THIN FILMS

---

into account as demonstrated in Chapter 2.3.1 [139]:

$$Y^{-1}(\omega) = \frac{1}{i\omega C_0} \left( 1 - k_t^2 \frac{\tan\left(\frac{kt}{2}\right)}{\frac{kt}{2}} \right) \quad (3.25)$$

where  $\omega$  is the angular frequency,  $C_0$  is the clamped capacitance,  $t$  is the thickness of the piezoelectric plate and  $k$  is the wave vector of the longitudinal wave. The wave vector  $k$ , the elastic constant  $c^D$  and the electromechanical coupling factor  $k_t^2$  are defined as [139]:

$$k = \frac{\omega}{\sqrt{\frac{c_{33}^D}{\rho}}} \quad (3.26)$$

$$c_{33}^D = c_{33}^E + \frac{e_{33}^2}{\varepsilon_{33}} \quad (3.27)$$

$$k_t^2 = \frac{e_{33}^2}{c_{33}^D \varepsilon_{33}} \quad (3.28)$$

Using Eqs.(3.18), (3.19), (3.20) and (3.27), we can express  $c^D$  at constant  $D$  as:

$$c_{33}^D = c_{33}^0 \left( 1 - \frac{m_{333}}{c_{33}^0} (P_3^{dc})^2 - \frac{e_{33}^2 \varepsilon_{33}^b}{\chi_{33}^f c_{33}^0 \varepsilon_{33}} \right) \quad (3.29)$$

In the TE mode the relations for the antiresonance  $f_{ares}$  and the resonance frequency  $f_{res}$  are given by [139]:

$$f_{ares} = \frac{1}{2t} \sqrt{\frac{c_{33}^D}{\rho}} \quad (3.30)$$

$$f_{res} = \frac{1}{2\pi t} \sqrt{(\pi^2 - 8k_t^2) \frac{c_{33}^D}{\rho}} \quad (3.31)$$

Substitution of Eq. (3.29) into Eqs. (3.30) and (3.31) gives the field dependence of the antiresonance and the resonance frequency, respectively:

$$f_{ares} = \frac{1}{2t} \sqrt{\frac{c_{33}^0}{\rho} \left( 1 - \frac{m_{333}}{c_{33}^0} (P_3^{dc})^2 - \frac{e_{33}^2 \varepsilon_{33}^b}{\chi_{33}^f c_{33}^0 \varepsilon_{33}} \right)} \quad (3.32)$$

$$f_{res} = \frac{1}{2\pi t} \sqrt{(\pi^2 - 8k_t^2) \frac{c_{33}^0}{\rho} \left( 1 - \frac{m_{333}}{c_{33}^0} (P_3^{dc})^2 - \frac{e_{33}^2 \varepsilon_{33}^b}{\chi_{33}^f c_{33}^0 \varepsilon_{33}} \right)} \quad (3.33)$$

Equations (3.32) and (3.33) represent the exact description of the field dependence of the antiresonance and the resonance frequency, respectively, and can be calculated with  $P^{dc}$  given in Eq. (3.14).

### 3.3 Field dependence of the acoustic resonances (TE mode)

In practical situations the electromechanical coupling will be weak, meaning that the effect of the dc electric field on the elastic parameters of the system is small. Therefore, the difference between  $c_{ij}^D$  or  $c_{ij}^E$  and  $c_{ij}^0$  can be considered as small and the electromechanical coupling factor  $k_t^2$  will be much smaller than 1. In this case, by taking Eqs. (3.18), (3.20) and (3.28) into account and keeping the leading terms in  $(P^{dc})^2$ , Eqs. (3.32) and (3.33) can be simplified to:

$$f_{ares} = \frac{1}{2t} \sqrt{\frac{c_{33}^0}{\rho}} \left( 1 - k_t^2 \left( \frac{m_{333}\varepsilon_{33}}{8q_{33}^2 (\chi_{33}^f)^2} + \frac{\varepsilon_{33}^b}{2\chi_{33}^f} \right) \right) \quad (3.34)$$

$$f_{res} = \frac{1}{2t} \sqrt{\frac{c_{33}^0}{\rho}} \left( 1 - k_t^2 \left( \frac{m_{333}\varepsilon_{33}}{8q_{33}^2 (\chi_{33}^f)^2} + \frac{\varepsilon_{33}^b}{2\chi_{33}^f} \right) - \frac{4}{\pi^2} k_t^2 \right) \quad (3.35)$$

Considering the case of high permittivity materials ( $\varepsilon \approx \chi^f \gg \varepsilon^b$ ), the relations (3.34) and (3.35) can be written in simpler form:

$$f_{ares} = \omega_0 \left( 1 - k_t^2 \left( \gamma_t + \frac{\mu}{2} \right) \right) \quad (3.36)$$

$$f_{res} = \omega_0 \left( 1 - k_t^2 \left( \gamma_t + \frac{\mu}{2} \right) - k_t^2 \frac{4}{\pi^2} \right) \quad (3.37)$$

where

$$\gamma_t \approx \frac{m_{333}}{8q_{33}^2 \varepsilon_{33}} \quad (3.38)$$

$$\mu \approx \frac{\varepsilon_{33}^b}{\varepsilon_{33}} \quad (3.39)$$

$$f_o = \frac{1}{2t} \sqrt{\frac{c_{33}^0}{\rho}} \quad (3.40)$$

$$k_t^2 = \frac{4q_{33}^2 \varepsilon_{33}}{c_{33}^0} (P^{dc})^2 \quad (3.41)$$

In these equations, the effect of the tuning dc field is introduced through two field dependent variables  $\varepsilon_{33}(E^{dc})$  and  $P^{dc}(E^{dc})$ . The dependences  $P^{dc}(E^{dc})$  and  $\varepsilon_{33}(E^{dc})$  can either be taken from an independent experiment or be calculated with the aid of Eqs. (3.14) and (3.15), respectively, neglecting the difference between  $\varepsilon_{33}^f$  and  $\chi_{33}^f$ , with the vectors  $E_i^{dc}$  and  $P_i^{dc}$  being set as  $(0 \ 0 \ E^{dc})$  and  $(0 \ 0 \ P^{dc})$ .

### 3. THEORY OF ELECTRICAL TUNING OF DC BIAS INDUCED ACOUSTIC RESONANCES IN PARAELECTRIC THIN FILMS

---

#### 3.4 Field dependence of the acoustic resonances (LFE mode)

The LFE mode corresponds to the geometry of a coplanar capacitor as shown in Fig. 3.1b. The propagation direction of the traveling acoustic wave is  $X_3$  like in the TE mode, but now because of the geometry of the problem it is the  $X_1$  components of the dc and ac electric fields that are relevant. The applicability conditions for the consideration are identical to those given for the TE mode. Again the film is considered to be clamped in the in-plane direction, but is free in the out-of-plane direction. The electrodes are considered as being of zero mass.

For the LFE mode the field dependent constitutive equations can be written in Voigt notation:

$$D_1 = \varepsilon_{11}E_1 + e_{13}u_3 \quad (3.42)$$

$$\sigma_3 = c_{33}^E u_3 - e_{13}E_1 \quad (3.43)$$

where

$$e_{13} = \chi_1^f h_{13} \quad (3.44)$$

and  $c_{33}^E$  has already been defined in Eq. (3.24).

The admittance  $Y$  (or impedance  $Z$ ) of the piezoelectric plate can be derived by taking the mechanical boundary conditions, mechanical wave equation and the Poisson equation into account as demonstrated in Chapter 2.3.1 [139]:

$$Y(\omega) = i\omega C_0 \left( 1 + k_{lat}^2 \frac{\tan\left(\frac{kt}{2}\right)}{\frac{kt}{2}} \right) \quad (3.45)$$

where the electromechanical coupling factor  $k_{lat}^2$  is given by [139]:

$$k_{lat}^2 = \frac{e_{13}^2}{c_{33}^E \varepsilon_{11}} \quad (3.46)$$

The relations for the resonance and the antiresonance frequency are given by [139]:

$$f_{res} = \frac{1}{2t} \sqrt{\frac{c_{33}^E}{\rho}} \quad (3.47)$$

$$f_{ares} = \frac{1}{2\pi t} \sqrt{(\pi^2 - 8k_t^2) \frac{c_{33}^E}{\rho}} \quad (3.48)$$

In the same way as for the TE mode discussed in Section 3.3, the field dependencies of the resonance and antiresonance frequencies are found by substituting Eq. (3.24) into

### 3.4 Field dependence of the acoustic resonances (LFE mode)

---

Eqs. (3.47) and (3.48). Treating the case of weak electromechanical coupling and taking Eqs. (3.18), (3.20) and (3.46) into account, Eqs. (3.47) and (3.48) read:

$$f_{res} = \frac{1}{2t} \sqrt{\frac{c_{33}^0}{\rho}} \left( 1 - k_{lat}^2 \left( \frac{m_{331}\varepsilon_{11}}{8q_{31}^2 (\chi_{11}^f)^2} + \frac{\varepsilon_{11}}{2\chi_{11}^f} \right) \right) \quad (3.49)$$

$$f_{ares} = \frac{1}{2t} \sqrt{\frac{c_{33}^0}{\rho}} \left( 1 - k_{lat}^2 \left( \frac{m_{331}\varepsilon_{11}}{8q_{31}^2 (\chi_{11}^f)^2} + \frac{\varepsilon_{11}}{2\chi_{11}^f} \right) - \frac{4}{\pi^2} k_t^2 \right) \quad (3.50)$$

Using Eq. (3.40) and considering high permittivity materials we can rewrite the relations for the field dependent resonance and antiresonance frequencies as:

$$f_{res} = \omega_0 \left( 1 - k_{lat}^2 \left( \gamma_{lat} + \frac{1}{2} \right) \right) \quad (3.51)$$

$$f_{ares} = \omega_0 \left( 1 - k_{lat}^2 \left( \gamma_{lat} + \frac{1}{2} \right) - k_{lat}^2 \frac{4}{\pi^2} \right) \quad (3.52)$$

where

$$\gamma_{lat} \approx \frac{m_{331}}{8q_{31}^2 \varepsilon_{11}} \quad (3.53)$$

$$k_{lat}^2 = \frac{4q_{13}^2 \varepsilon_{11}}{c_{33}^0} (P^{dc})^2 \quad (3.54)$$

Here, similar to the TE mode case, the dependences  $P^{dc}(E^{dc})$  and  $\varepsilon_{11}(E^{dc})$  can either be taken from an independent experiment or be calculated with the aid of Eqs. (3.14) and (3.15), respectively, neglecting the difference between  $\varepsilon_{11}^f$  and  $\chi_{11}^f$ , with the vectors  $E_i^{dc}$  and  $P_i^{dc}$  being set as  $(E^{dc} \ 0 \ 0)$  and  $(P^{dc} \ 0 \ 0)$ .

As a summary, Tab. 3.1 lists the relations for the tuning of the resonance and the antiresonance frequency for the two considered modes of excitation.

Table 3.1: Relations for the tuning of the resonance and antiresonance frequencies for the TE and the LFE mode of excitation.

Resonance tuning	TE mode	LFE mode
$\frac{f_{res}-f_0}{f_0}$	$-k_t^2(\gamma_t + \frac{\mu}{2} + \frac{4}{\pi^2})$	$-k_{lat}^2(\gamma_{lat} + \frac{1}{2})$
$\frac{f_{ares}-f_0}{f_0}$	$-k_t^2(\gamma_t + \frac{\mu}{2})$	$-k_{lat}^2(\gamma_{lat} + \frac{1}{2} + \frac{4}{\pi^2})$

## 3.5 Relation between the electromechanical coupling factors and the relative tunability

In the previous section we have shown that for the realistic experimental situation where the background contribution to the permittivity can be neglected and the relative tuning of the elastic constants and the electromechanical coupling factors are small, both  $k_t^2$  and  $k_{lat}^2$  exhibit dc field dependences identical to those of the factors  $\varepsilon_{33} (P^{dc})^2$  and  $\varepsilon_{11} (P^{dc})^2$ , respectively. One can readily show that these factors also control the dc field dependence of the relative tunability  $n_r$  of the material defined as [138]:

$$n_r = \frac{\varepsilon(0) - \varepsilon(E^{dc})}{\varepsilon(0)} = 1 - \frac{\varepsilon(E^{dc})}{\varepsilon(0)} \quad (3.55)$$

Here,  $\varepsilon(0)$  and  $\varepsilon(E^{dc})$  correspond to the permittivity at zero and under dc bias, respectively. Indeed, for the case of  $X_3$  non-zero components of the field and polarization, taking Eqs. (3.2) and (3.15), and neglecting the background contribution to the dielectric permittivity we find:

$$\varepsilon_{33}(0) = \frac{1}{\alpha_{33}} \quad (3.56)$$

$$\varepsilon_{33}(E^{dc}) = \frac{1}{\alpha_{33}^* + 3\beta_{33}(P^{dc})^2} \quad (3.57)$$

where the Voigt Notation  $\beta_{33} \equiv \beta_{3333}$  is used. Equations (3.55) to (3.57) imply:

$$n_r = 3\beta_{33}\varepsilon_{33}(P^{dc})^2 \quad (3.58)$$

For the case of  $X_1$  non-zero components of the field and polarization, on the same lines we get:

$$n_r = 3\beta_{11}\varepsilon_{11}(P^{dc})^2 \quad (3.59)$$

Now combining Eqs. (3.41), (3.54), (3.58), and (3.59) we find a simple relation between the electromechanical coupling factors and the relative tunability:

$$k_t^2 = A_t n_r \quad (3.60)$$

$$k_{lat}^2 = A_{lat} n_r \quad (3.61)$$

with

$$A_t = \frac{4q_{33}^2}{3c_{33}^0\beta_{33}} \quad (3.62)$$

$$A_{lat} = \frac{4q_{31}^2}{3c_{33}^0\beta_{11}} \quad (3.63)$$



## 3.6 Modeling and Discussion

In this section we model and discuss the theoretical field dependence of the resonance and antiresonance frequency for the TE and the LFE mode for the case of paraelectric BST films.

In BST the dielectric permittivity is typically larger than 300, so that the background contribution to its permittivity can be neglected. We will address the case of the typical experimental situation where both the relative tuning of the elastic constants and electromechanical coupling factors are small compared to unity. Thus, in our analysis we can use the simple relations (3.36), (3.37), (3.51) and (3.52). The material parameters of BST films needed for the analysis were calculated from the available literature data; they are listed in Tab. 3.2. The details of the calculations can be found in Appendix A.

### Tuning behavior in the TE mode

Tuning of the resonance and antiresonance frequencies in this mode is described by the relations (3.36) and (3.37). Let us compare the tuning behavior of these frequencies.

To do this, we first evaluate the factor  $\gamma_t + \mu/2$ . For high permittivity materials, like BST in paraelectric phase,  $\varepsilon \gg \varepsilon^b$ . Therefore, the term  $\mu = \varepsilon^b/\varepsilon$  is much smaller than 1. To estimate the magnitude of the term  $\gamma_t$ , we calculated the values of  $q_{33}$  for different BST compositions and orientations as listed in Tab. 3.2. As Tab. 3.2 shows the values of  $q_{33}$  are about  $10^{10}$  m/F for different compositions and the considered orientations of the BST thin film. For the coefficients of the tensor of nonlinear electrostriction  $m_{ijk}$  no published experimental data on BST is available to the authors' knowledge. From ab-initio calculations, the components of  $|m_{ijk}|$  for BST(x=1) are of the order of  $10^{11}$  m/F [140]. Using these estimates we can evaluate  $|\gamma_t| \cong 10/\varepsilon_{33}^r \ll 1$  where  $\varepsilon_{33}^r$  is the relative permittivity of BST. Note that the components of  $m_{ijk}$  and  $\gamma_t$  can be of either sign. From the presented estimates we infer that the sum  $|\gamma_t + \mu/2| \ll 1$  and that, depending on the relation between  $\mu$  and  $\gamma_t$ ,  $\gamma_t + \mu/2$  can be of either sign as well.

Bearing in mind the above statements and that the tuning of the resonance and antiresonance frequencies is controlled by the factors  $\gamma_t + \mu/2 + 4/\pi^2$  and  $\gamma_t + \mu/2$  (see Eqs. (3.36) and (3.37)), we can draw the following conclusions. First, since, the factor  $\gamma_t + \mu/2 + 4/\pi^2 \approx 0.4$  is much larger than  $\gamma_t + \mu/2$ , a much stronger tuning of the resonance than the antiresonance frequency is expected. Second, since  $\gamma_t + \mu/2 + 4/\pi^2 \approx 0.4$  is always positive, the resonance frequency will always shift to lower frequencies with increasing dc bias. Third, the sign of tuning of the antiresonance frequency with increasing dc bias is controlled by that of the sum  $\gamma_t + \mu/2$ , thus the antiresonance frequency can shift both up or down with increasing dc bias.

For a given relative dielectric tunability, the amount of tuning for both frequencies is also controlled by the  $A_t$  factor (see Eqs. (3.36), (3.37), (3.41), and (3.60)). This factor calculated for different film orientations and compositions is given in Tab. 3.2. For BST(x

### 3. THEORY OF ELECTRICAL TUNING OF DC BIAS INDUCED ACOUSTIC RESONANCES IN PARAELECTRIC THIN FILMS

---

Table 3.2: List of the tensor components  $q_{33}$ ,  $q_{31}$ ,  $c_{33}$ ,  $\beta_{33}$  controlling the tuning of the resonance and the antiresonance frequency in the TE and LFE mode. The calculated proportionality factors  $A_t$  and  $A_{lat}$  between the electromechanical coupling factors and the relative tunability  $n_r$  are also listed. The values are given for different BST compositions and orientations. The values are calculated for room temperature ( $T=25^\circ\text{C}$ ).

Variables	BST (x=0)	BST (x=0.3)	BST (x=0.5)	BST (x=0.7)	BST (x=1)
$q_{33}^{(001)} (\times 10^{10} \text{ m/F})$	2.53	2.61	2.67	2.73	2.81
$q_{31}^{(001)} (\times 10^9 \text{ m/F})$	-1.53	-2.18	-2.61	-3.04	-3.69
$c_{33}^{(001)} (\times 10^{11} \text{ N/m}^2)$	3.16	2.98	2.86	2.73	2.55
$\beta_{33}^{(001)} (\times 10^9 \text{ Vm}^5/\text{C}^3)$	8.96	5.68	3.52	1.38	-1.82
$A_t^{(001)} (\times 10^{-1})$	3.01	5.39	9.45	26.26	-22.61
$A_{lat}^{(001)} (\times 10^{-3})$	1.10	3.74	9.03	32.71	-39.12
$q_{33}^{(110)} (\times 10^{10} \text{ m/F})$	1.43	1.46	1.48	1.50	1.53
$q_{31}^{(110)} (\times 10^9 \text{ m/F})$	9.48	9.36	9.28	9.20	9.05
$c_{33}^{(110)} (\times 10^{11} \text{ N/m}^2)$	3.32	3.15	3.04	2.93	2.77
$\beta_{33}^{(110)} (\times 10^9 \text{ Vm}^5/\text{C}^3)$	5.58	3.44	2.03	0.65	-1.42
$A_t^{(110)} (\times 10^{-1})$	1.47	2.62	4.72	15.86	-7.98
$A_{lat}^{(110)} (\times 10^{-1})$	0.65	1.08	1.85	5.95	-2.78
$q_{33}^{(111)} (\times 10^{10} \text{ m/F})$	1.06	1.08	1.08	1.09	1.11
$q_{31}^{(111)} (\times 10^9 \text{ m/F})$	5.81	5.52	5.32	5.12	4.80
$c_{33}^{(111)} (\times 10^{11} \text{ N/m}^2)$	3.37	3.21	3.11	3.00	2.84
$\beta_{33}^{(111)} (\times 10^9 \text{ Vm}^5/\text{C}^3)$	4.45	2.69	1.54	0.40	-1.28
$A_t^{(111)} (\times 10^{-1})$	1.00	1.78	3.28	13.24	-4.48
$A_{lat}^{(111)} (\times 10^{-2})$	2.99	4.69	7.89	28.97	-8.44

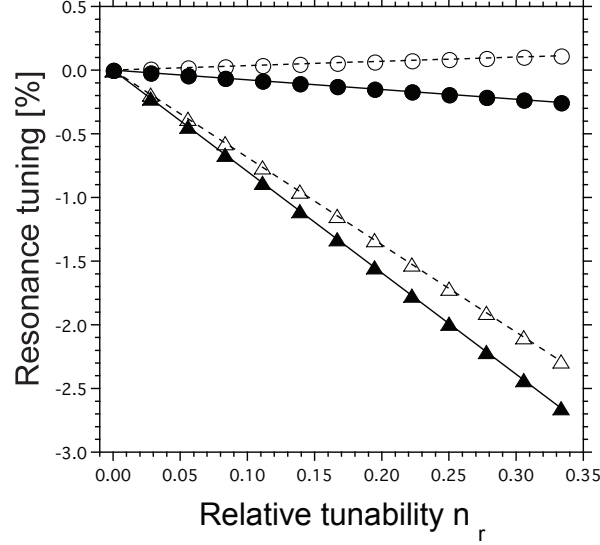


Figure 3.2: Modeled dependence of the tuning of the resonance and antiresonance frequencies on the relative tunability  $n_r$  of a BST( $x=0.3$ ) thin film with (111) orientation in the TE mode. If the sum  $\gamma_t + \mu/2$  is positive the antiresonance frequency (filled circle) and the resonance frequency (filled triangle) shift down to lower frequencies. If the sum  $\gamma_t + \mu/2$  is negative the antiresonance frequency (open circle) shifts up whereas the resonance frequency (open triangle) shifts down. In any case the resonance frequency shifts down and shows a much stronger dependence on the dc bias than the antiresonance frequency. The values used in the modeling were taken from Tab. 3.2:  $q_{33} = 1.1 \times 10^{10}$  m/F;  $\varepsilon_{33}^r = 300$ ;  $\varepsilon^b = 7$ ;  $A_t = 0.178$ . The value of  $m_{333} = +7.5 \times 10^{10}$  m/F was used for  $\gamma_t + \mu/2$  being positive. For a negative sign of the sum  $\gamma_t + \mu/2$  the value of  $m_{333} = -7.5 \times 10^{10}$  m/F was used in the modeling.

$\leq 0.7$ ) the values indicate an increase in the electromechanical coupling factor  $k_t^2$  and therefore a stronger tuning of the resonance frequency for increasing Ba concentration at a given  $n_r$ . For BST( $x=1$ ) the values of  $A_t$  become negative since the corresponding components of  $\beta_{33}$  are negative. A negative value of  $\beta_{ij}$  corresponds to a negative  $n_r$ . Experimentally, it was found that, in the limit of small tuning, the permittivity of BST( $x=1$ ) single crystals in the paraelectric phase can increase with increasing dc bias [141]. This means that  $n_r$  is negative. To describe the field dependence of the dielectric permittivity and of the resonance tuning for BST( $x=1$ ) compositions at higher electric fields, higher order polarization terms of the dielectric response in the Landau free energy expansion need to be taken into account [142].

Figure 3.2 illustrates the modeled dependence of the tuning of the resonance and

### 3. THEORY OF ELECTRICAL TUNING OF DC BIAS INDUCED ACOUSTIC RESONANCES IN PARAELECTRIC THIN FILMS

---

antiresonance frequencies on the relative tunability  $n_r$  for a BST( $x=0.3$ ) thin film with (111) orientation and  $m_{333} = \pm 7.5 \times 10^{10}$  m/F. As discussed above the resonance frequency shifts always to lower frequencies with increasing dc bias and shows a stronger dependence on the dc bias than the antiresonance frequency. The antiresonance frequency can shift up or down with increasing dc bias depending on the sign of the sum  $\gamma_t + \mu/2$ . Published experimental data for BST films ( $x=0.2-0.3$ ) corroborates with the theoretical predictions, corresponding to the case of  $\gamma_t + \mu/2 > 0$  [133; 143].

#### Tuning behavior in the LFE mode

The tuning of resonance and the antiresonance frequencies in the LFE mode is described by the relations (3.51) and (3.52).

In contrast to the TE mode, in the relations for the LFE mode  $\mu/2$  is replaced by 0.5. This can be understood by considering the geometry of the two modes of excitation. In the TE mode the polarization  $P_i$  and the wave vector  $k$  are parallel which results in a depolarizing field. The term  $\mu$  takes the effect of the depolarizing field into account. In the LFE mode the polarization  $P_i$  and the wave vector  $k$  are perpendicular. In this case there is no depolarizing field and the term  $\mu$  is replaced with 1. The difference in the electrical conditions in the waves is also responsible for the displacements of the factor  $4/\pi^2$  from the relation for the resonance frequency (for the TE mode) to that for the antiresonance frequency (for the LFE mode). The tuning behavior in the LFE mode in BST films is expected to be strongly dependent on the orientation of the films. The reason for this is a strong orientation dependence of  $\gamma_{lat}$  (in contrast to  $\gamma_t$ ).

For (110) and (111) orientations, using the data from Tab. 3.2 and the above estimate  $|m_{jik}| \cong 10^{11}$  m/F, one finds  $\gamma_{lat} \ll 1$ . Thus, one can neglect  $\gamma_{lat}$  in Eqs. (3.51) and (3.52) to find that the relative tuning of the resonance and antiresonance frequencies is about  $0.5k_{lat}^2$  and  $0.9k_{lat}^2$ , respectively. In both cases, the frequencies will always shift down to lower frequencies with increasing dc bias. Such behavior is illustrated in Fig. 3.3 which shows the modeled dependence of the tuning of resonance and antiresonance frequency on the relative tunability  $n_r$  for a BST( $x=0.3$ ) thin film with (110) orientation in the LFE mode and  $m_{331} = \pm 10^{11}$  m/F. For BST films of (001) orientation, the values of  $q_{31}$  are up to an order of magnitude smaller than those used for the above estimates of  $\gamma_{lat}$  and  $\gamma_t$ . This implies that  $\gamma_{lat}$  increases by up to 2 orders of magnitude for this orientation, so that  $|\gamma_{lat}|$  can be comparable to 1. Here, different types of tuning behavior of the characteristic frequencies of the impedance of the system are possible. Depending on the sign and value of  $\gamma_{lat}$ , both frequencies can shift up with increasing bias field, both down, or one up and one down. Examples of possible tuning behaviors in this case are illustrated in Fig. 3.4, which shows the modeled dependence of the tuning of the resonance and antiresonance frequency on the relative tunability  $n_r$  in the LFE mode calculated for parameters of a BST( $x=0.3$ ) thin film with (001) orientation taken from Tab. 3.2 and  $m_{331} = \pm 10^{11}$  m/F. Note that in the case of the LFE mode the absolute value of tuning for a given  $n_r$  for

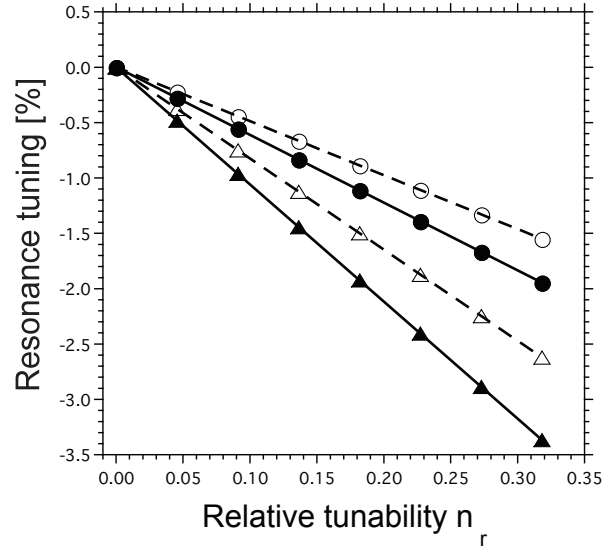


Figure 3.3: Modeled dependence of the resonance and antiresonance frequencies on the relative tunability  $n_r$  for a BST( $x=0.3$ ) thin film with (110) orientation in the LFE mode. The values used for the modeling were taken from Tab. 3.2:  $q_{31} = 9.4 \times 10^{10}$  m/F;  $m_{331} = \pm 10^{11}$  m/F;  $\epsilon_{11}^r = 300$ ;  $\epsilon^b = 7$ ;  $A_{lat} = 0.11$ . For  $m_{331} = +10^{11}$  m/F the antiresonance (filled triangles) frequency shows a stronger dc bias dependence than the resonance (filled circles) frequency. Both resonance and antiresonance frequencies shift down with increasing bias. For  $m_{331} = -10^{11}$  m/F the tuning of the antiresonance (open triangles) and the resonance (open circles) frequency is slightly reduced but shows the same principal behavior as for  $m_{331} = +10^{11}$  m/F.

### 3. THEORY OF ELECTRICAL TUNING OF DC BIAS INDUCED ACOUSTIC RESONANCES IN PARAELECTRIC THIN FILMS

---

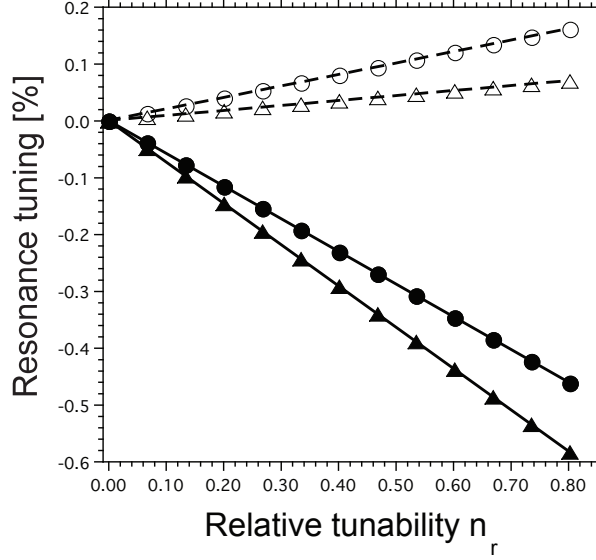


Figure 3.4: Modeled dependence of the resonance and antiresonance frequencies on the relative tunability  $n_r$  for a BST( $x=0.3$ ) thin film with (001) orientation in the LFE mode. The values used for the modeling are taken from Tab. 3.2:  $q_{31} = -2.18 \times 10^9$  m/F;  $m_{331} = \pm 10^{11}$  m/F;  $\varepsilon_{11}^r = 300$ ;  $\varepsilon^b = 7$ ;  $A_{lat} = 0.00374$ . For  $m_{331} = +10^{11}$  m/F both antiresonance (filled triangles) and resonance frequency (filled circles) shift down with increasing dc bias. The antiresonance frequency shows a stronger dc bias dependence then the resonance frequency. For  $m_{331} = -10^{11}$  m/F both antiresonance (open triangles) and resonance frequency (open circles) shift up with increasing dc bias.

(100) thin films is small in comparison to that of (110) oriented thin films (c.f. scale of the y-axis in Figs. 3.3 and 3.4).

The theoretical prediction concerning the tuning of the characteristic frequencies in LFE mode cannot be compared to experimental results since the latter are not available in the literature.

### Use of $P$ and $D$ expansions for the derivation of the constitutive equations

Considering our theoretical treatment of the dc bias induced piezoelectric resonances in centrosymmetric high permittivity materials we want to stress several points. We have derived our results by starting with the Landau free energy expansion in terms of the ferroelectric contribution to the polarization ( $P$ -expansion) where we took into account

the nonlinear electrostriction and the background permittivity, which are customarily neglected. This is a proper way to derive the field dependent coefficients of the basic constitutive piezoelectric equations (3.16) and (3.17). A derivation of the field dependent coefficients starting from Landau free energy in terms of the electric displacement ( $D$ -expansion) is also possible, but in this case the term  $e^2 \varepsilon^b / (\chi^f c \varepsilon)$  is missing from Eq. (3.29) [135]. Often the tensor of nonlinear electrostriction  $m_{ijklmn}$  is neglected. This leads again to a wrong description of the field dependent elastic constant  $c^D$  because the important term  $m (P^{dc})^2 / c$  in Eq. (3.29) would be missing.

We have actually stated above that the constitutive equations derived from the  $D$ -expansion of the free energy of the ferroelectric does not properly describe the dependence of the coefficients of these equations on the value of the applied dc field and that the  $P$ -expansion does. At this point a question arises of why we consider the  $P$ -expansion as more credible than the  $D$ -expansion. Such a question is justified since the treatments of dielectric and electromechanical properties of ferroelectrics that can be found in the literature are often based on the  $D$ -expansion or, the most often, on the expansion in terms of the total polarization of the system ( $P^{tot} = D - \varepsilon_0 E$ ). Here, the following arguments are available. First of all, in a wide class of problems, all three types of the free energy expansion lead to basically identical results. At the same time, the results obtained using these schemes can differ essentially if the depolarizing field enters the game (in the present chapter it is the calculations for the TE geometry). In this case, in general, the predictions of  $D$ -expansion,  $P$ -expansion, and  $P^{tot}$ -expansion can be different, so that the question of which scheme is to be trusted arises. (Specifically, using the  $D$ -expansion one finds the factor  $\mu$  from Eqs. (3.36) and (3.37) equal to zero whereas the  $P^{tot}$ -expansion leads to  $\mu$  which is  $\varepsilon^b / \varepsilon_0$  times smaller than that given by Eq. (3.39)). To decide which of the results to trust, one should address the microscopic justification of the Landau expansion for ferroelectrics. When deriving the Landau expansion from the microscopic calculations, one obtains an expansion in terms of the microscopic order parameter which, in displacive ferroelectrics, is the soft mode displacement (see e.g. [144]). Among  $D$ ,  $P^{tot}$ , and  $P$ , only the latter (ferroelectric contribution to the polarization) is always proportional to the microscopic order parameter. Thus, it is the  $P$ -expansion that is the original and to be trusted.

It is worth also mentioning that the choice of the variables of the Landau expansion for the derivation of the constitutive electromechanical equations is fully independent of that for the variables used in the calculations of the impedance of the system. We have demonstrated this when changing variables in Section 3.2.

### Applicability of the results obtained

All results obtained in this chapter have been derived starting from the Landau free-energy expansion containing only the lowest non-linear polarization term ( $P^4$ ) and by keeping only the lowest non-linear  $P^3$  terms in the renormalized equation of state (see Eq. 3.14).

### 3. THEORY OF ELECTRICAL TUNING OF DC BIAS INDUCED ACOUSTIC RESONANCES IN PARAELECTRIC THIN FILMS

---

Let us now shortly discuss the impact of higher order non-linear polarization terms (e.g.  $P^6$  terms in the energy and  $P^5$  terms in the equation of state).

An essential feature of the principle result of this chapter - the field dependencies of the characteristic frequencies of the impedance of the system - is that these frequencies are functions of the permittivity and induced polarization,  $\varepsilon(E^{dc})$  and  $P(E^{dc})$ , while there is no other dependence on  $E^{dc}$ . Taking into account the higher order non-linear polarization terms will modify the  $\varepsilon(E^{dc})$  and  $P(E^{dc})$  dependencies. If needed, they can be calculated in a straightforward way. Of importance is that the field dependencies of the characteristic frequencies given in this chapter remain valid in the case of arbitrary dielectric non-linearity if the results are written in terms of  $\varepsilon(E^{dc})$  and  $P(E^{dc})$ . Actually, results written in this way can be used with the dependencies  $\varepsilon(E^{dc})$  and  $P(E^{dc})$  taken from experiment.

The result really sensitive to the higher order non-linear polarization terms is the relation between the field-induced electromechanical coupling factor and the relative tunability in Eqs. (3.60) and (3.61). These relations are essentially based in the equation of state containing  $P^3$  as the non-linear term. Thus, if in the material higher order terms are important for the description of the dielectric non-linearity, the simple relations (3.60) and (3.61) do not hold any more. Such a situation occurs, for example, in BST with high barium concentration.

It should be mentioned that the calculated values of  $A_t$  should only be taken as rough estimates because of some uncertainties in the literature values of the tensor components controlling the values of  $A_t$ .

## 3.7 Summary and Conclusions

To summarize, we have derived the field dependence of the dc bias induced acoustic resonance phenomenon in paraelectric materials starting from the Landau free energy expansion with respect to the ferroelectric (soft-mode) contribution to the polarization ( $P$ -expansion). We have derived the field dependent piezoelectric constitutive equations for the general case. Using these equations, we have modeled the dc field dependence (tuning) of the frequencies of acoustic resonances and antiresonances for thickness (TE) and the lateral field (LFE) excitation modes. We have found that, for these excitation modes, the tuning can be qualitatively different. It has been shown that, in ferroelectrics with high dielectric permittivity, the dc-field induced electromechanical coupling factor and the relative tuning of dielectric permittivity  $n_r$  exhibit the same bias field dependence, including the case where  $n_r$  is not small compared to unity. The formulated framework has been applied to the analysis of tuning of resonators based on paraelectric BST films of (100), (110) and (111) orientations for different Ba contents. It has been demonstrated that the adequate description of the field dependence of the induced acoustic resonances requires the constitutive equations derived from the  $P$ -expansion where the background



### 3.7 Summary and Conclusions

---

permittivity and the nonlinear electrostriction (customarily neglected), are taken into account.



## Chapter 4

# Growth and characterization of $\text{Ba}_x\text{Sr}_{1-x}\text{TiO}_3$ thin films on platinized silicon

This chapter is dedicated to the growth and characterization of BST thin films deposited on platinized Si substrates.

### 4.1 Introduction

We report on the processing and structural and electrical characterization of BST thin films deposited on platinized Si substrates. Two different compositions, namely BST( $x=0.3$ ) and BST( $x=0.7$ ), were investigated. The aim of this work was to obtain information about the quality of our BST thin films. This information is also of relevance for the BST TF-BARs discussed in Chapter 5. The films were deposited under the same conditions as for the TFBAR devices. The BST thin films were structurally characterized by x-ray diffraction (XRD), Transmission Electron Microscopy (TEM) and Atomic Force Microscopy (AFM). The electrical characterization provided information on the temperature and dc bias dependence of the dielectric properties of the BST thin films. Where possible, we compare the obtained results with relevant data from the literature.

### 4.2 Film growth and fabrication of test devices

In this section, the processing of the BST thin films, the deposition method, and the design and fabrication of the test structures is described.

#### 4. GROWTH AND CHARACTERIZATION OF $\text{Ba}_x\text{Sr}_{1-x}\text{TiO}_3$ THIN FILMS ON PLATINIZED SILICON

---

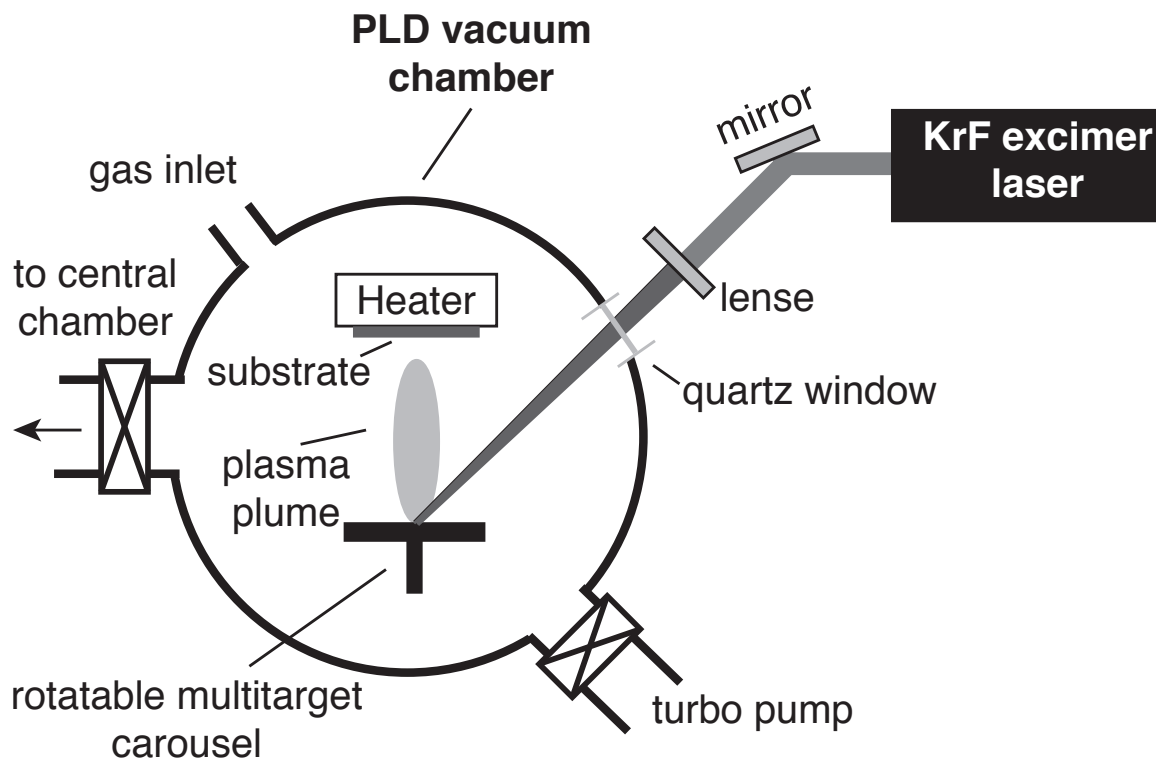


Figure 4.1: Schematic drawing of a PLD setup.

##### 4.2.1 Pulsed Laser Deposition method

Pulsed Laser Deposition (PLD) is a Physical Vapor Deposition (PVD) technique to grow thin films of a wide variety of materials [145]. The method is based on coupling of photonic energy provided by a laser to a, normally solid, target. The most common types of lasers used for PLD systems are excimer lasers and frequency-multiplied Nd:YAG solid-state lasers. Typically, the lasers have a wavelength of about 200 to 400 nm and a pulse duration of about 5 to 20 ns. The intense laser pulse heats a small volume of material on the surface of the target to very high temperatures where a plasma is formed and all elements of the target material are evaporated. The evaporated material condenses on the substrate which is placed opposite the target. In principal, the stoichiometry of the target is directly transferred to the thin film. This allows for depositing multi-component stoichiometric films from single targets [146; 147]. This is an advantage over other deposition techniques where controlling the film stoichiometry is more difficult [148].

The basic setup of a PLD system is shown in Fig. 4.1. The laser and the high vacuum deposition chamber are separated, which is one of the advantages of PLD increasing

the (geometrical) flexibility of the method. The pulsed laser beam is directed through an optical system of mirrors and lenses on a quartz window of the deposition chamber. The quartz window is transparent to the wavelength of the laser which minimizes energy loss. The laser light enters the deposition chamber and is focused on the solid target. The laser spot focused on the target surface has a typical size of about  $1 \text{ mm}^2$ . PLD systems are often equipped with a multi-target carousel offering the possibility to deposit heterostructures without breaking the vacuum [149]. To avoid quick local erosion and groove development on the target, the target is rotated or rastered leading to a homogeneous ablation of the target surface. The laser beam hits the target at an incident angle of  $30$  to  $45^\circ$ . The target material absorbs the laser energy and a highly forward directed plasma plume develops. The plasma plume contains electrons, ions, atoms, molecules and clusters of material. The evaporated material is deposited on the substrate which is typically placed parallel and opposite to the target.

### 4.2.1.1 The ablation process

The ablation process has been studied in detail by many authors [145; 150]. The absorption of the laser radiation on the surface of the target leads to a conversion of the electromagnetic energy of the laser to strong electronic excitation in the target material. The excited electrons transfer their energy to the lattice within a few picoseconds resulting in heating of the material within the optical absorption depth  $1/\alpha$  where  $\alpha$  is the optical absorption coefficient.

Using femto- or picosecond lasers, the excitation ends at this point and the developing plasma plume can expand in the direction of the substrate. For longer pulse durations, typical for excimer lasers, the processes are more complicated. The long pulse duration leads to melting of a macroscopic region of the target and to an interaction of the expanding plasma plume with the incident laser beam. The depth of the melted surface layer depends on the laser wavelength and pulse duration. Melting of the target surface can lead to the formation of particulates (also called droplets) in the film due to the recoil pressure of the plasma plume [145]. The interaction of the expanding plasma plume and the laser leads to a strong absorption of the laser energy by the plasma. Thus, the bulk material is, at least partially, screened by the remainder of the plasma plume. The absorption of the laser energy results in an increase in the degree of ionization and a significant gas-phase heating of the plasma plume. The kinetic energies of the plasma species range from about  $1$  to about  $100 \text{ eV}$  [151; 152] and also depend strongly on the laser fluence. A typical value for the velocity of ions and atoms in the plasma plume is  $10 \text{ km/s}$  which means that the plasma plume reaches the substrate in  $5 \text{ }\mu\text{s}$  for a target-substrate distance of  $5 \text{ cm}$ .

The plasma plume is strongly peaked along the normal to the target surface. The angular distribution of the plume has been fitted by many authors to a  $\cos^n \theta$  function with  $n$  ranging from  $2$  to  $20$  [153]. In general,  $n$  increases with laser fluence and spot size and decreases when a background gas is used, which broadens the angular distribution.

#### 4. GROWTH AND CHARACTERIZATION OF $\text{Ba}_x\text{Sr}_{1-x}\text{TlO}_3$ THIN FILMS ON PLATINIZED SILICON

---

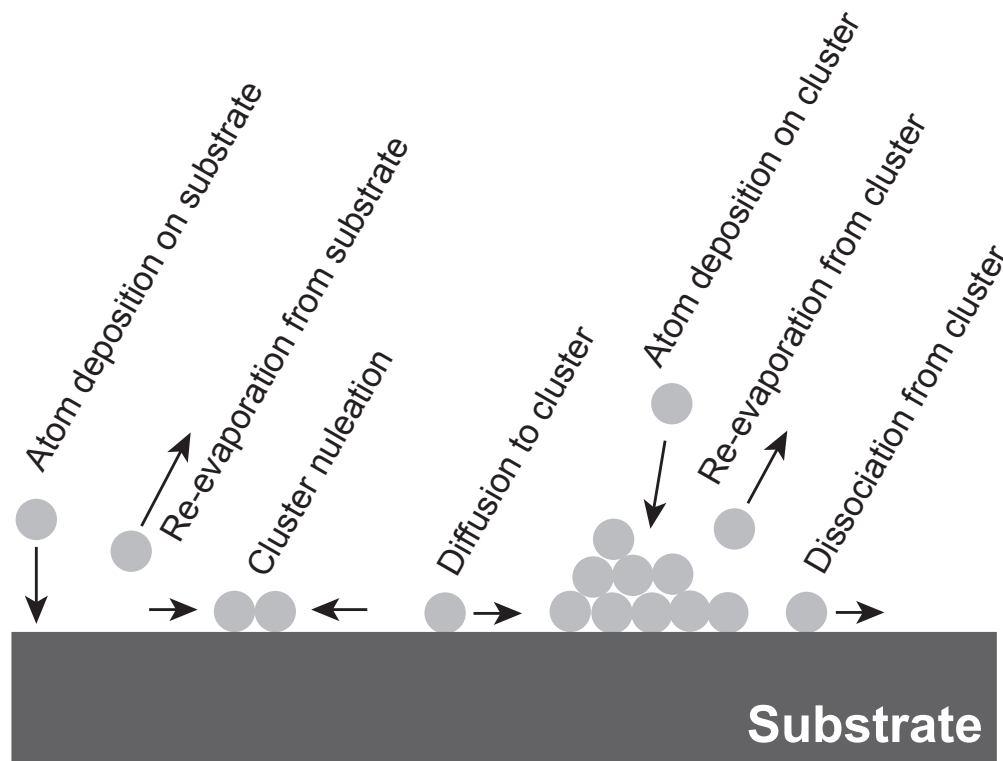


Figure 4.2: Schematic viewgraph of possible processes occurring during film nucleation.

##### 4.2.1.2 Film growth by PLD

The nucleation of film-atom clusters on a substrate surface due to the arrival of atoms in a vapor phase involves several processes as shown in Fig. 4.2. The arrival rate of atoms on the substrate or on preexisting clusters depends on deposition parameters. The arriving atoms can diffuse over the substrate or preexisting clusters, diffuse to or dissociate from existing clusters, form new clusters or be re-evaporated. Once thermodynamically stable clusters are formed, film growth occurs. Depending mainly on the interface energies between clusters, surface, and vapor, three different growth modes are observed. These growth modes include the Volmer-Weber (island growth), the Frank-van-der Merwe (monolayer growth) and the Stranski-Krastanov (monolayer followed by island growth) mode. These models are in principle equally applicable to the PLD process [154; 155; 156].

The great differences between PLD and other deposition techniques like sputtering or thermal evaporation are due to the pulsed nature of the PLD process and the relatively high energies of the vapor species. The arrival energies of the vapor species can range from several eV for neutral atoms to several hundreds of eV for ions in the vapor flux. This

can have important effects when the deposition is done in vacuum. Ions with a kinetic energy of about 100 eV can cause sputtering of the film. If a background gas, as for example for the deposition of oxides, is used, the energy of the vapor species is reduced due to various scattering processes. The pulsed nature of the PLD process leads to a brief period of incident vapor flux on the substrate ( $\approx 1$  ms) followed by a relatively long period ( $\approx 100$  ms, assuming a laser repetition rate of 10 Hz) without arriving vapor flux. This can have an effect on the film growth if the pulse period approximately matches the time constants for all the relevant diffusion, agglomeration, and dissociation phenomena during film nucleation and growth. If the pulse period is much shorter or longer than the above mentioned time constants, the effect of the pulsed nature on the film nucleation and growth is expected to be of minor importance [145]. Another important feature of the pulsed nature is the effect of the background pressure. For typical background pressures in the mTorr-range, the arrival rate of the background gas atoms (oxygen atoms in case of oxide films) and the average arrival rate of the film atoms are comparable. This can promote stoichiometric film formation [145].

### 4.2.2 Film growth and annealing conditions

BST thin films with compositions  $x=0.3$  and  $x=0.7$  were deposited on platinized Si(001) substrates. For the test structures, standard Si test wafers with low resistivity were used (electrical resistivity  $\rho=0.1$  to  $100 \Omega\cdot\text{cm}$ ). The wafers were dry-oxidized to deposit 100 nm of  $\text{SiO}_2$  on the wafer surfaces. The Pt bottom electrode was deposited at  $300^\circ\text{C}$  by DC magnetron sputtering on the oxidized silicon wafer using a thin  $\text{TiO}_2/\text{Ti}$  adhesion layer (Balzers, BAS450, Liechtenstein). The Pt bottom electrode had a thickness of 100 nm. XRD analysis of the Pt bottom electrode revealed a pure (111) texture without detection of any other orientation in the out-of-plane direction. After bottom electrode deposition the 4 inch wafer was cut into square-shaped samples of about 1.2 cm edge length to have a compatible substrate size for the PLD system.

BST thin films with compositions  $x=0.3$  and  $x=0.7$  were deposited by PLD (SURFACE GmbH + Co KG., Germany). Before film deposition the substrates were cleaned in isopropanol with ultrasound agitation. The substrates were heated at  $10^\circ\text{C}/\text{min}$  up to the deposition temperature. Sintered ceramic discs of the appropriate BST composition were used as targets. Prior to PLD deposition, the targets were pre-cleaned by ablating the target surface with the laser for approximately 2 min. The BST thin films were deposited at  $T=600^\circ\text{C}$  and  $p(\text{O}_2)=5\times 10^{-4}$  Torr using a KrF excimer laser with  $\lambda=248$  nm (Lambda Physik AG, COMPex 201, Germany). The laser frequency was set to 5 Hz. The laser energy was 220 mJ which resulted in an estimated energy density at the laser spot of about  $10 \text{ J}/\text{cm}^2$ . The target to substrate distance was set to 5 cm. A deposition time of about 75 to 90 min resulted in the desired film thickness of about 500 nm. The films were cooled down at  $2.5^\circ\text{C}/\text{min}$  to avoid film damage since faster cooling rates resulted in microcracks in the BST thin films. After BST thin film deposition, the samples were

#### 4. GROWTH AND CHARACTERIZATION OF $\text{Ba}_x\text{Sr}_{1-x}\text{TiO}_3$ THIN FILMS ON PLATINIZED SILICON

---

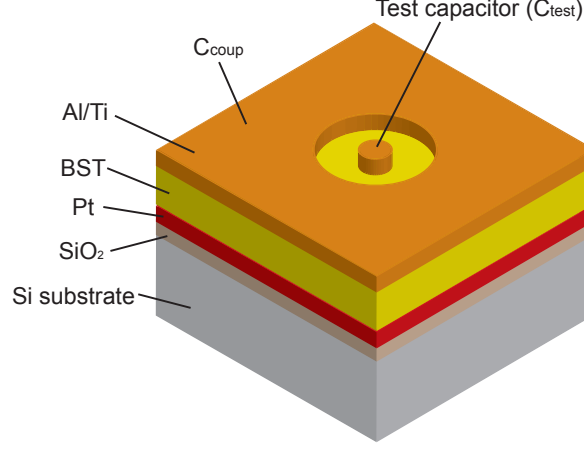


Figure 4.3: Schematic drawing of a test capacitor. The large capacitor  $C_{coup}$  provides capacitive coupling to the Pt bottom electrode.

annealed in air at 500 °C for 1 h in order to decrease the oxygen vacancy population [157] and to improve the film quality.

##### 4.2.3 Fabrication of test structures

For the electrical characterization of the BST thin films, Metal-Insulator-Metal (MIM) test structures were fabricated. For the test structures, circular-patch capacitor structures as proposed by Ma et al. [158] were used. The advantages of the proposed design are the simple fabrication (one step of photolithography) and the avoidance of etching the dielectric layer to contact the bottom electrode. As a top metallization, Al(300 nm)/Ti(30 nm) were deposited by room temperature evaporation (Oerlikon Leybold Vacuum GmbH, LAB600H, Germany). The Ti layer was deposited to improve adhesion of the Al layer on the BST surface. After evaporation, the top metallization was patterned by lift-off. An example of a test structure is shown in Fig. 4.3. The test devices were formed by the small circular top electrodes. The diameter of these circular electrodes ranged from 10 to 50  $\mu\text{m}$ . The bottom electrode was contacted by probing the large metal pad surrounding the test devices, which resulted in capacitive coupling to the bottom electrode. In this case, measurements of two capacitors connected in-series are performed. The measured capacitance  $C_{meas}$  is:

$$\frac{1}{C_{meas}} = \frac{1}{C_{test}} + \frac{1}{C_{coup}} \quad (4.1)$$

where  $C_{test}$  and  $C_{coup}$  are the capacitance of the test device and the capacitance of the large capacitor surrounding the circular capacitor, respectively. Since  $C_{coup} \gg C_{test}$ ,



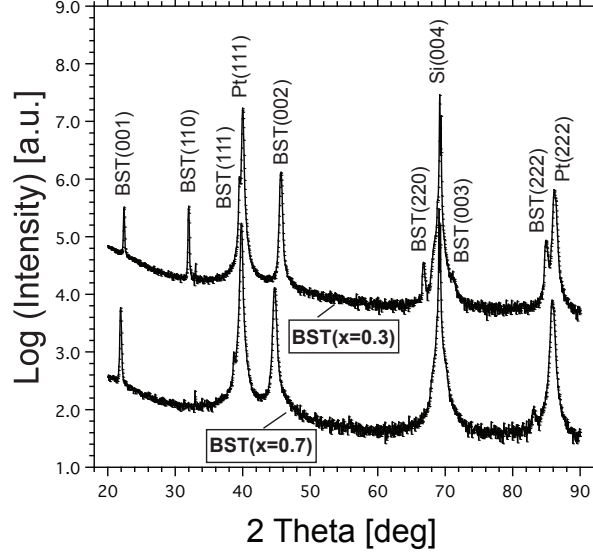


Figure 4.4: Comparison of x-ray diffraction patterns of BST thin films with composition  $x=0.3$  and  $x=0.7$ .

$$C_{meas} = C_{test}.$$

## 4.3 Results and Discussion

### 4.3.1 Structural characterization

The BST thin films with composition  $x=0.3$  and  $x=0.7$  were characterized by x-ray diffraction (XRD) using a Bragg-Brentano diffractometer (Siemens, Kristalloflex 805, Germany). The diffractometer was equipped with a Cu source providing Cu  $K\alpha$  radiation ( $\lambda=1.5418 \text{ \AA}$ ). The tension  $U$  and the current  $I$  were set to 40 kV and 35 mA, respectively. Diffraction peaks were identified and indexed with the JCPDS Powder diffraction file database. XRD was used for phase analysis and investigation of the out-of-plane orientation of the BST thin films.

Figure 4.4 shows a comparison of the x-ray diffraction patterns obtained from BST thin films with composition  $x=0.3$  and  $x=0.7$ , respectively. All detected peaks could be attributed to either BST, Pt or Si indicating that no crystalline secondary phase was present in the films. The Pt bottom electrode showed a strong (111) texture typically observed for Pt films sputtered on oxidized Si. The BST ( $x=0.7$ ) film showed only peaks of the (00l) and (hhh) family of lattice planes. The (110) peak being the most intense peak in a randomly oriented BST bulk ceramic (see JCPDS file: 39-1395) was completely absent.

#### 4. GROWTH AND CHARACTERIZATION OF $\text{Ba}_x\text{Sr}_{1-x}\text{TiO}_3$ THIN FILMS ON PLATINIZED SILICON

---

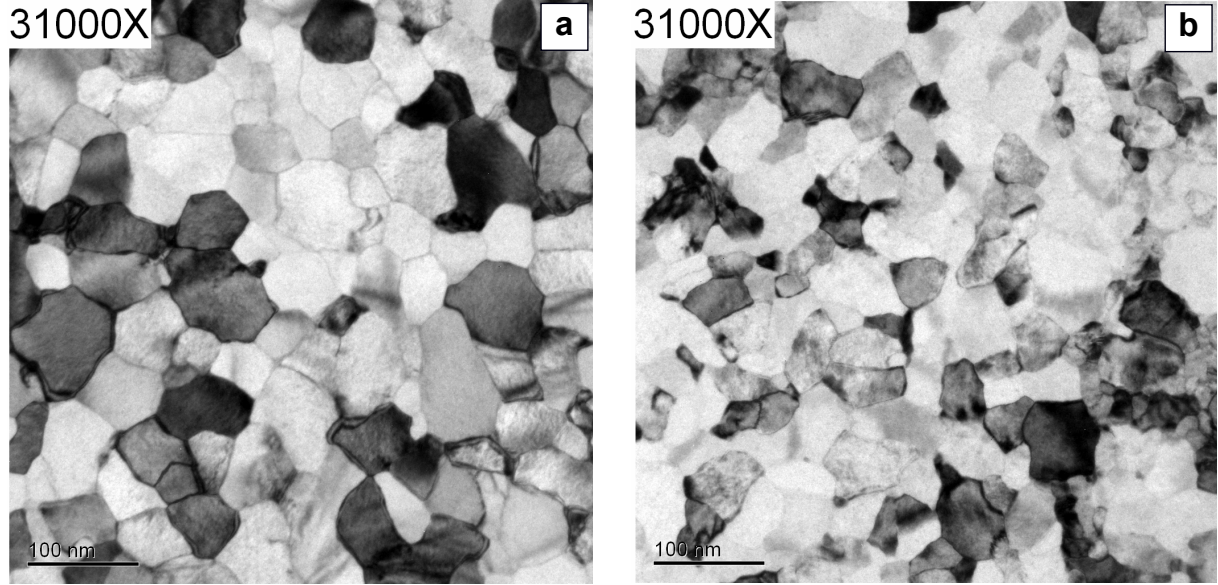


Figure 4.5: TEM plane view images of BST ( $x=0.3$ ) (a) and BST ( $x=0.7$ ) (b) thin films.

For the BST ( $x=0.3$ ) thin film, peaks of the (001), (hh0) and (hhh) family of lattice planes were detected. The (110) peak was relatively weaker than the peaks (002) and (111) in comparison to a randomly oriented BST bulk ceramic. Therefore, it is concluded that both BST thin films exhibit a strong (001) and (111) texture in the out-of-plane direction. A (001) texture of BST thin films deposited (or annealed) at high temperatures (typically  $T \geq 650^\circ\text{C}$ ) on Pt(111)/Si has been observed by many authors [43; 44; 159]. The (001) texture of BST thin films was also found to be promoted by increasing film thickness [45].

The microstructure of the BST thin films was studied by Transmission Electron Microscopy (TEM) (Philips, CM300, Netherlands). Figure 4.5 shows plane-view TEM images of the BST thin films with compositions  $x=0.3$  and  $x=0.7$ . Both films exhibited a very dense microstructure without any indication of pores or voids. No evidence of significant amounts of secondary phases like amorphous material at grain boundaries could be found. The BST ( $x=0.3$ ) thin film showed an average lateral grain size of about 50 nm. This was slightly larger than the average lateral grain size of the BST ( $x=0.7$ ) thin film which was about 30 nm. Lee et al. observed that the lateral grain size increases with increasing film thickness [47]. Considering the film thickness of about 500 nm for our films, their lateral grain size appears to be rather small if compared to the data in the literature where for the same deposition temperature the same grain size (about 50 nm) or a larger grain size is normally observed for thinner film [47].

Investigation of the cross-section of the BST thin films (not shown here) revealed a

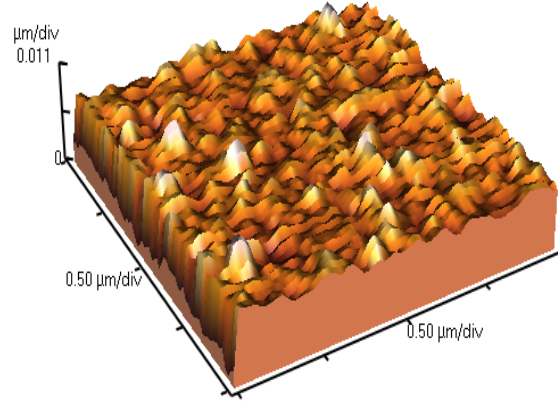


Figure 4.6: Typical example of an AFM scan. The image is shown for the BST( $x=0.3$ ) thin film.

columnar grain structure typically observed for BST thin films deposited by PVD methods. In this case the microstructure consists of single-crystalline grains throughout the film thickness that exhibit a random orientation in the in-plane direction [40].

The surface roughness of the BST thin films was investigated with Atomic Force Microscopy (AFM) operated in contact mode. The area of  $2 \times 2 \mu\text{m}$  was scanned at a rate of 0.25 Hz. A typical example of an image of these scans is shown in Fig. 4.6 for the BST( $x=0.3$ ) thin film. Images for the BST( $x=0.7$ ) thin film were comparable without any significant difference. The root mean square roughness (rms) was  $1.3 \pm 0.3 \text{ nm}$  and  $1.1 \pm 0.3 \text{ nm}$  for the BST( $x=0.3$ ) and BST( $x=0.7$ ) thin film, respectively.

### 4.3.2 Electrical characterization

The low-frequency electrical characterization of the BST test capacitors was performed with a precision LCR meter (Hewlett-Packard, HP4284A, USA). A sinusoidal (ac) voltage of 10 mV was applied to the sample. Measurements were performed in the frequency range of 1 kHz to 1 MHz. The measurement frequency will be specified for all data shown in this section. Temperature dependent measurements were performed in a special chamber (MMR-Technologies Inc, LTMP4, USA) that allowed the temperature to be varied from -180 to about 100 °C. For the measurement of the field dependent properties, a dc bias of max.  $\pm 40 \text{ V}$  was supplied by the LCR meter. All the measurements were software controlled using different Labview programs.

Figure 4.7 shows the temperature dependence of the permittivity and the loss tangent

#### 4. GROWTH AND CHARACTERIZATION OF $\text{Ba}_x\text{Sr}_{1-x}\text{TiO}_3$ THIN FILMS ON PLATINIZED SILICON

---

of the BST thin films. The measurements were performed at 1 MHz. The BST ( $x=0.3$ ) thin film shown in Fig. 4.7a showed a permittivity of about 310 and a loss tangent of about 0.02 at  $T=25^\circ\text{C}$ . The permittivity increased with decreasing temperature. At  $T \approx -180^\circ\text{C}$ , a maximum in the permittivity was observed. The loss tangent of the BST ( $x=0.3$ ) thin film was fairly constant with temperature.

The BST( $x=0.7$ ) thin film shown in Fig. 4.7b exhibited a permittivity of about 390 and a loss tangent of about 0.03 at  $T=25^\circ\text{C}$ . The permittivity increased slightly with decreasing temperature until a broad maximum of the permittivity was observed in the temperature range of  $-60$  to  $-110^\circ\text{C}$ . Below  $-110^\circ\text{C}$  the permittivity dropped to lower values. In the temperature interval of  $-60$  to  $-110^\circ\text{C}$ , the loss tangent started to increase with decreasing temperature. An increase in the loss tangent below the temperature of maximum permittivity of BST( $x=0$ ) thin films was also observed by Keane et al. [160]. They found that their films displayed ferroelectric behavior below the temperature of maximum permittivity. A possible explanation for the increase in the loss tangent is the stabilization of the polar phase of the BST structure, where a domain-related contribution to the loss tangent of the BST film might exist.

Comparing the temperature of maximum permittivity of our BST thin films with bulk samples with the corresponding compositions, we observed a shift to lower temperatures for the BST thin films. The phase transition temperature for bulk ceramics decreases linearly from  $T_c=120^\circ\text{C}$  for BST( $x=1$ ) (corresponding to  $\text{BaTiO}_3$ ) by  $3.4^\circ\text{C}$  per mole percent of strontium [20]. Thus, the phase transition temperatures of BST bulk samples with  $x=0.3$  and  $x=0.7$  composition are  $-118$  and  $18^\circ\text{C}$ , respectively. The downward shift of the maximum of permittivity of our thin films might be attributed to some effects related to the grain size. This was demonstrated by Horikawa et al. who showed that the maximum of permittivity shifts to lower temperatures with decreasing grain size [48].

A comparison of the permittivity of our thin films with literature data is difficult since many factors affect the permittivity of BST thin films. Among these factors the most important are film thickness, grain size, film stress, and film stoichiometry. Since the (micro-)structural characteristics of the thin films vary considerably, a comparison is not straight forward, if possible at all. If we consider only the film composition, we find that comparing our results with the relevant literature data, an enhancement of the dielectric permittivity of our BST thin films should be considered. This is especially true for the BST( $x=0.7$ ) thin film. But, since we want to integrate these BST thin films in TFBAR devices, we were also restricted in the deposition conditions of the thin films. Higher deposition temperatures could enhance the dielectric permittivity of our films significantly, but also led to cracking of the membranes of the TFBAR devices. Therefore, we kept the deposition temperatures of our thin films rather low.

Figure 4.8 shows the dc bias dependence of the permittivity and the loss tangent for the BST thin films with composition  $x=0.3$  (Fig. 4.8a) and  $x=0.7$  (Fig. 4.8b). For both thin films no significant hysteresis associated with the  $\varepsilon - E$  curve could be observed as is expected for materials in the paraelectric phase. The BST ( $x=0.3$ ) thin film showed

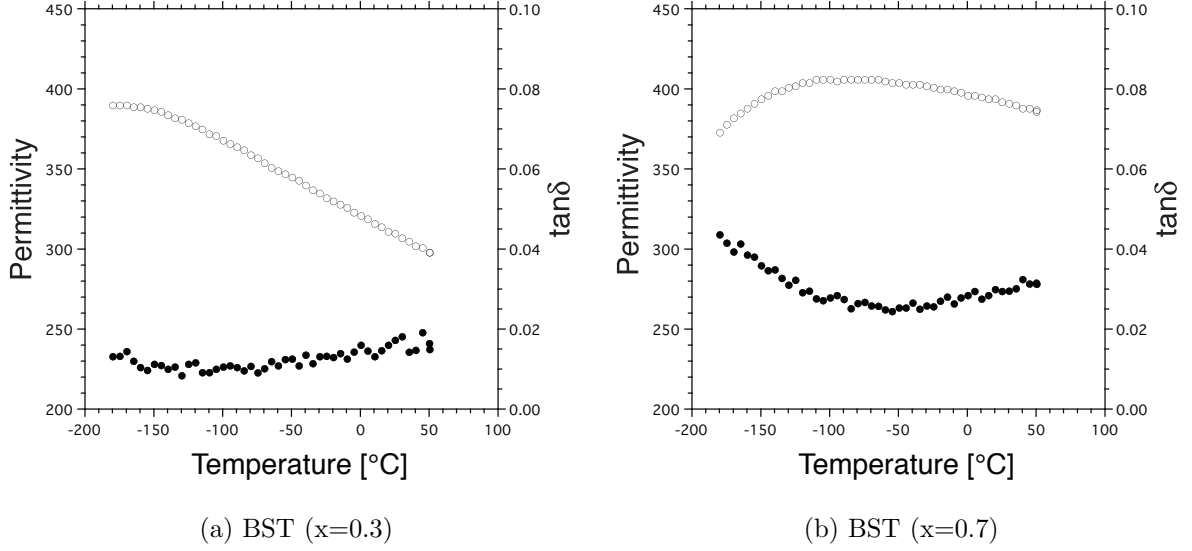


Figure 4.7: Temperature dependence of the permittivity (open circles) and the loss tangent (filled circles) of the BST thin films. (a) and (b) show the data for the BST films with  $x=0.3$  and  $x=0.7$  composition, respectively.

a relative tunability  $n_r$  of about 47% at a dc electric field  $E_{dc}=750$  kV/cm. Under dc bias the loss tangent showed a small decrease. A slight increase in the loss tangent was observed only at high negative dc electric fields.

The BST ( $x=0.7$ ) thin film exhibited a relative tunability  $n_r$  of about 56% at 750 kV/cm. The loss tangent was about 0.03. The higher tunability and loss tangent of the BST ( $x=0.7$ ) thin film in comparison to the BST ( $x=0.3$ ) thin film can be explained by its higher permittivity. Both tunability and loss tangent dependent on the permittivity. In general, the rule “the higher the permittivity, the higher the tunability and loss tangent” [10] is valid. For weak dc electric fields the loss tangent showed a small decrease. At high negative dc electric field an increase in the loss tangent was observed like in the case of the BST ( $x=0.3$ ) thin film.

This increase of the loss tangent at high negative dc electric fields can be attributed to the lower work function  $W$  of the Ti layer ( $W_{Ti}=4.45$  eV) at the interface between BST and top electrode in comparison to Pt ( $W_{Pt}=5.3$  eV) [161]. The lower work function leads to increased thermoionic emission from the cathode under dc bias which increases the leakage currents at a given dc electric field [161]. Higher leakage currents mean that the conductivity  $\sigma$  is increased. The conductivity contributes to the imaginary part of the permittivity  $\varepsilon'' = \sigma/\omega$ , where  $\omega$  is the angular frequency. The increase in the imaginary part of the permittivity results in an increase in the loss tangent  $\tan\delta = \varepsilon''/\varepsilon' = \sigma/\omega\varepsilon'$ .

#### 4. GROWTH AND CHARACTERIZATION OF $\text{Ba}_x\text{Sr}_{1-x}\text{TiO}_3$ THIN FILMS ON PLATINIZED SILICON

---

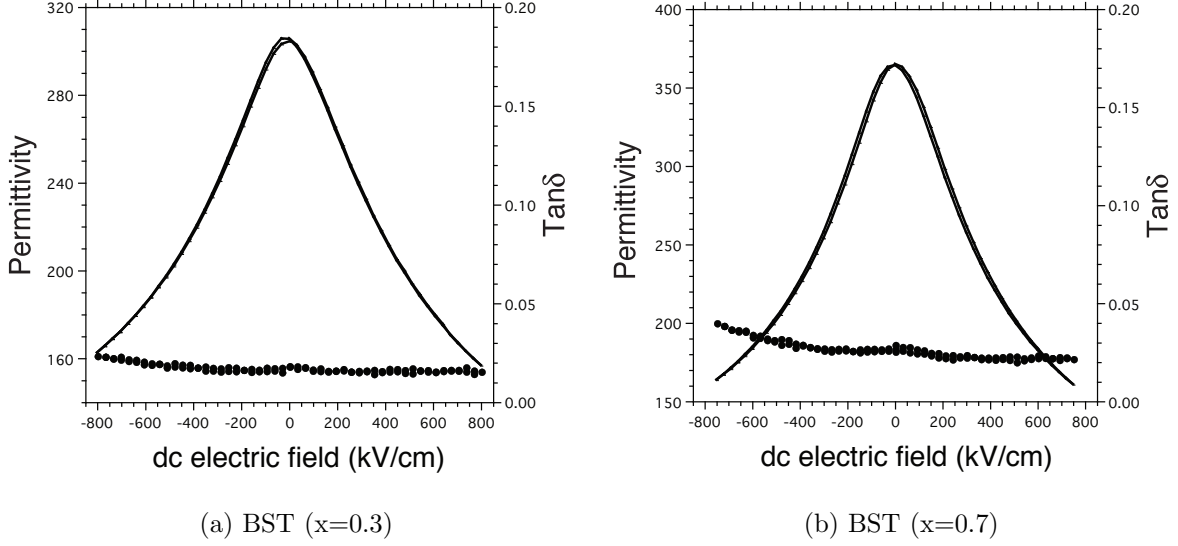


Figure 4.8: Dependence of the permittivity (solid line) and the loss tangent (filled circles) on the dc electric field. (a) and (b) show the data for the BST films with  $x=0.3$  and  $x=0.7$  composition, respectively.

#### 4.4 Summary and Conclusions

In this chapter we investigated the structural and electrical properties of BST thin films deposited on platinized Si substrates. The obtained information on the BST thin film properties are important for an estimation of the material quality and are of relevance for the performance and the understanding of the fabricated BST TFBARs discussed in Chapter 5.

BST thin films of  $x=0.3$  and  $x=0.7$  composition were investigated. Both thin films showed a (001)/(111) texture. The films were nano-crystalline with an average grain size below 50 nm. The root mean square surface roughness of both films were comparable with about 1.2 nm. Both BST thin films showed a diffuse phase transition. The maximum in the permittivity of the BST( $x=0.3$ ) thin film was at about  $T=-180$  °C and at about  $T=-110$  to  $-60$  °C for the BST( $x=0.7$ ) thin film. The maximum of the permittivity was shifted to lower temperatures in comparison to the bulk counterparts which might be explained by grain size effects. For the BST ( $x=0.7$ ) thin film the tunability and the loss tangent were 56% and 0.03 at room temperature. For the BST ( $x=0.3$ ) thin film the tunability and the loss tangent were 47% and 0.02 at room temperature. The higher tunability and the loss tangent of the BST( $x=0.7$ ) thin film in comparison to the BST( $x=0.3$ ) can be explained by the initially higher permittivity of the BST( $x=0.7$ ) thin film. Comparing the performance of our BST thin films with the available literature data, we find that

improvement of the film quality is still possible. A higher permittivity (which leads to a higher tunability at a given dc electric field) is often observed when comparing our results with literature data for BST thin films with the same compositions. This is especially true for the BST( $x=0.7$ ) thin film. But, since the BST thin films should be used in the membrane-type TFBARs, we were also restricted in the film deposition conditions. Depositing the BST thin films at higher temperatures led to cracking of the membranes of the TFBAR devices. Therefore, we kept the deposition temperature of our thin films rather low.





## Chapter 5

# Fabrication, characterization and modeling of BST-based TFBARs

This chapter deals with the fabrication, characterization, and modeling of TFBARs based on BST thin films in the paraelectric phase. The TFBARs are tunable via a dc electric field.

### 5.1 Introduction

Thin Film Bulk Acoustic Wave Resonators (TFBARs) are devices based on a piezoelectric thin film sandwiched between two electrodes. A TFBAR resonates at a certain frequency depending mainly on the sound velocity and the thickness of the different layers forming the structure. Typical applications include sensors [105; 162; 163], voltage controlled oscillators [106; 164], and electronic filters [104; 112]. Electronic filters based on TFBARs are already commercially available. The advantages of TFBARs for filter applications are their small size, high Q-factor [165], high-frequency operation [163; 166], etc. Drawbacks are the need to control precisely the thickness of the different layers of the structure in order to meet the tight specifications for the resonance frequencies [167]. A TFBAR, typically based on a piezoelectric AlN film, is normally static meaning that the resonance and the antiresonance frequencies of the device are fixed. For future communication system it is of interest to replace these static devices by reconfigurable or adaptive devices. In the ideal case a tunable filter could be adapted to operate at different frequency bands used in wireless communication systems. Thus, the number of components could be reduced which is of special interest in handheld wireless communication devices. Other advantages of tunable TFBARs include the possibility to compensate for temperature variations or aging and the possibility of a post-fabrication adjustment of the resonance frequency in case the tight specifications for the resonance frequencies for a given device can not be fulfilled. Tuning of TFBARs has been realized in various ways including the addition of

## 5. FABRICATION, CHARACTERIZATION AND MODELING OF BST-BASED TFBARS

---

a heating layer [116] (temperature tuning), application of a dc bias [118] (piezoelectric stiffening), and the combination of tunable capacitors and static TFBARs [168].

Another way to realize tunable TFBARs is to replace the piezoelectric layer of the devices by tunable materials that show piezoelectric activity [103]. One potential candidate is  $\text{Ba}_x\text{Sr}_{1-x}\text{TiO}_3$  (BST). The material is known for its nonlinear electrical properties [10] and is investigated for a range of tunable devices like varactors [14; 169], phase shifters [170], etc. If a dc bias is applied to the material to tune its dielectric permittivity, piezoelectricity is induced in the material through the electrostrictive effect as discussed in Chapter 2.2. We explored this effect to fabricate tunable TFBARs based on BST thin films [143; 171].

In this chapter we present the fabrication, characterization, and modeling of a BST TFBAR. We demonstrate that the TFBAR is tunable via a dc electric field. We apply the theory we developed in Chapter 3 in order to describe the electrical tuning characteristics of the device. We show that the tuning behavior of the BST TFBAR can be described by the relative tunability of the permittivity of the BST thin film. The Q-factor and the non-hysteretic tuning behavior are addressed. From the modeling we could estimate the value of the components of the tensor of nonlinear electrostriction which are of importance in the tuning behavior of the antiresonance frequency of BST TFBARs. We investigated the effect of a mechanical load on the performance of the tuning of the BST TFBAR.

### 5.2 Experimental details

In this section the process steps in the fabrication of BST-based TFBARs and its electrical characterization will be described. The different steps of fabrication will be described in detail and are summarized in Fig. 5.1.

#### 5.2.1 Device fabrication

##### 5.2.1.1 Silicon wafers

High resistive silicon wafers (Si-Mat, Germany) were used for the fabrication of the BST TFBAR (Fig. 5.1a). The 4 inch silicon wafers were double side polished, had a thickness of  $300\text{ }\mu\text{m}$ , and a high resistivity of  $\rho=10\text{ k}\Omega\cdot\text{cm}$ . The high resistivity of the silicon is needed in order to avoid conduction through the substrate during the high-frequency measurements. The high resistivity therefore helps to reduce parasitic effects.

##### 5.2.1.2 $\text{SiO}_2$ deposition

In a first processing step,  $\text{SiO}_2$  was deposited on the wafer surface. The  $\text{SiO}_2$  layer was deposited by wet oxidation in a Centrotherm furnace under  $\text{H}_2\text{O}$  vapor flux at

T=1050 °C (Fig. 5.1b). The following reaction occurs:



The time of the oxidation was controlled to deposit 2.5  $\mu\text{m}$  on both wafer sides. The  $\text{SiO}_2$  on the backside was structured in a later processing step (see Section 5.2.1.3) to serve as a hard mask for the deep Si etching which is the last processing step.

The  $\text{SiO}_2$  layer on the front side of the wafer was removed by BHF (7:1) wet chemical etching. The  $\text{SiO}_2$  on the wafer backside was prevented from being attacked by protecting it with a 3.5  $\mu\text{m}$  thick layer of photoresist (MicroChemicals, S1818, Germany). After this, the wafer was again oxidized. A  $\text{SiO}_2$  layer with 100 nm was deposited by dry oxidation (Fig. 5.1c). The dry oxidation process is characterized by heating the wafer to high temperatures under a flow of  $\text{O}_2$  gas. The thickness of the  $\text{SiO}_2$  of 100 nm was chosen to reduce the stresses in the membrane structure (thicker layers produce larger stresses) and to decrease the effect of a mechanical load on the active area of the resonator (see Section 5.3.3).

### 5.2.1.3 Patterning of backside $\text{SiO}_2$ layer - hard mask fabrication

The 2.5  $\mu\text{m}$  thick  $\text{SiO}_2$  layer on the backside was structured to serve as a mask for the deep Si etching in the last process step (Fig. 5.1d). A patterned photoresist with a thickness of 3.5  $\mu\text{m}$  was used as a mask for etching the  $\text{SiO}_2$  layer. The photoresist was patterned by exposing the resist through a photomask that was aligned with respect to the structured frontside of the wafer using a double side mask aligner (Süss Microtec, MA150, Germany). The  $\text{SiO}_2$  layer was etched by dry etching using an ICP (Inductively Coupled Plasma) reactor (Alcatel, AMS200 DSE, France). Etching of the  $\text{SiO}_2$  layer was performed at T=0 °C using  $\text{C}_4\text{F}_8$  gas. The reduced temperature of 0 °C improves the verticality of the side walls of the etched  $\text{SiO}_2$  and therefore improves the accuracy of the pattern transfer from the patterned photoresist to the  $\text{SiO}_2$  hard mask. The  $\text{SiO}_2$  layer was etched at a rate of  $\approx 225$  nm/min. After the etching process, the remaining photoresist was removed with remover (Shipley Co. Inc., Microposit Remover 1165, USA) at 70 °C for 10 min. followed by microwave plasma stripping in  $\text{O}_2$ . The openings in the  $\text{SiO}_2$  layer were square-shaped with an edge length of 350  $\mu\text{m}$ .

### 5.2.1.4 Bottom electrode deposition and patterning

A 100 nm thick Pt layer was deposited as a bottom electrode by dc magnetron sputtering as described in Section 4.2.2 (Fig. 5.1e). The Pt layer was patterned by dry etching using a RIE/ICP (Reactive Ion Etching coupled with Inductively Coupled Plasma) reactor (STS, Multiplex ICP, UK) (Fig. 5.1f). A patterned, spray coated photoresist (MicroChemicals, S1818, Germany) served as a mask for the etching process. The Pt layer was etched in a  $\text{Cl}_2/\text{Ar}$  gas mixture with a selectivity of about 1 to 8 with respect to the photoresist. The

## 5. FABRICATION, CHARACTERIZATION AND MODELING OF BST-BASED TFBARS

---

Pt etch rate was  $\approx 30$  nm/min. After the Pt etching, the photoresist mask was removed in remover (Shipley Co. Inc., Microposit Remover 1165, USA) at 70 °C for 10 min. followed by microwave plasma stripping in O<sub>2</sub>. The structured Pt electrode was square-shaped with an edge length of 270  $\mu\text{m}$  and was centered on the openings in the SiO<sub>2</sub> layer on the wafer backside.

### 5.2.1.5 BST film deposition

Prior to BST film deposition the prepared wafer was cut into square-shaped samples with an edge length of about 1.2 cm. Deposition of BST thin films with composition  $x=0.3$  as well as post-annealing of the films was undertaken as described in Section 4.2.2 (Fig. 5.1g). The BST thin film growth was controlled to reach the desired thickness.

### 5.2.1.6 Top electrode deposition

The top electrode of Al/Ti was deposited by evaporation (Oerlikon Leybold Vacuum GmbH, LAB600H, Germany) and patterned by lift-off (Fig. 5.1h). A negative photoresist (Futurrex Inc, NR7, USA) with a thickness of about 3.5  $\mu\text{m}$  was used for the lift-off. The layer thickness of Al and Ti were 300 and 30 nm, respectively. The Ti layer was deposited to improve adhesion of the Al layer on the BST surface. The metal pattern was defined to probe the device with GSG (Ground-Signal-Ground) probes with a 250  $\mu\text{m}$  pitch size. The contact pad for the signal electrode was 150 by 150  $\mu\text{m}$ . The active area of the device was varied from 200 to 600  $\mu\text{m}^2$ . The bottom electrode was contacted by capacitive coupling to avoid patterning of the BST layer and to simplify processing.

### 5.2.1.7 Membrane liberation - The Bosch process

In the final process step the Si substrate was removed locally under the active area of the resonator (Fig. 5.1i). The Si was etched by dry etching (Alcatel, AMS200 DSE, France) using the Bosch process [172]. The Si was anisotropically etched by using alternatingly 300 sccm of SF<sub>6</sub> gas for 9 s and 200 sccm C<sub>4</sub>F<sub>8</sub> gas for 2 s. The SF<sub>6</sub> gas is used for etching the Si whereas the C<sub>4</sub>F<sub>8</sub> gas is used to passivate the Si side walls through polymerization. The Bosch process is used to etch deep, anisotropic holes into silicon. The Si was etched at a rate of  $\approx 4.5$   $\mu\text{m/s}$ . The selectivity of the etch process against etching of SiO<sub>2</sub> is about 200 so that the patterned SiO<sub>2</sub> on the backside serves as a hard mask for the deep Si etch process. An example of a SEM top view image of a BST TFBAR is shown in Fig. 5.2. Fig. 5.3a shows schematic a cross-section of the fabricated device. Fig. 5.3b shows the same device but with increased mechanical load. Details about the investigations on the effect of the mechanical load will be discussed in Section 5.3.3.

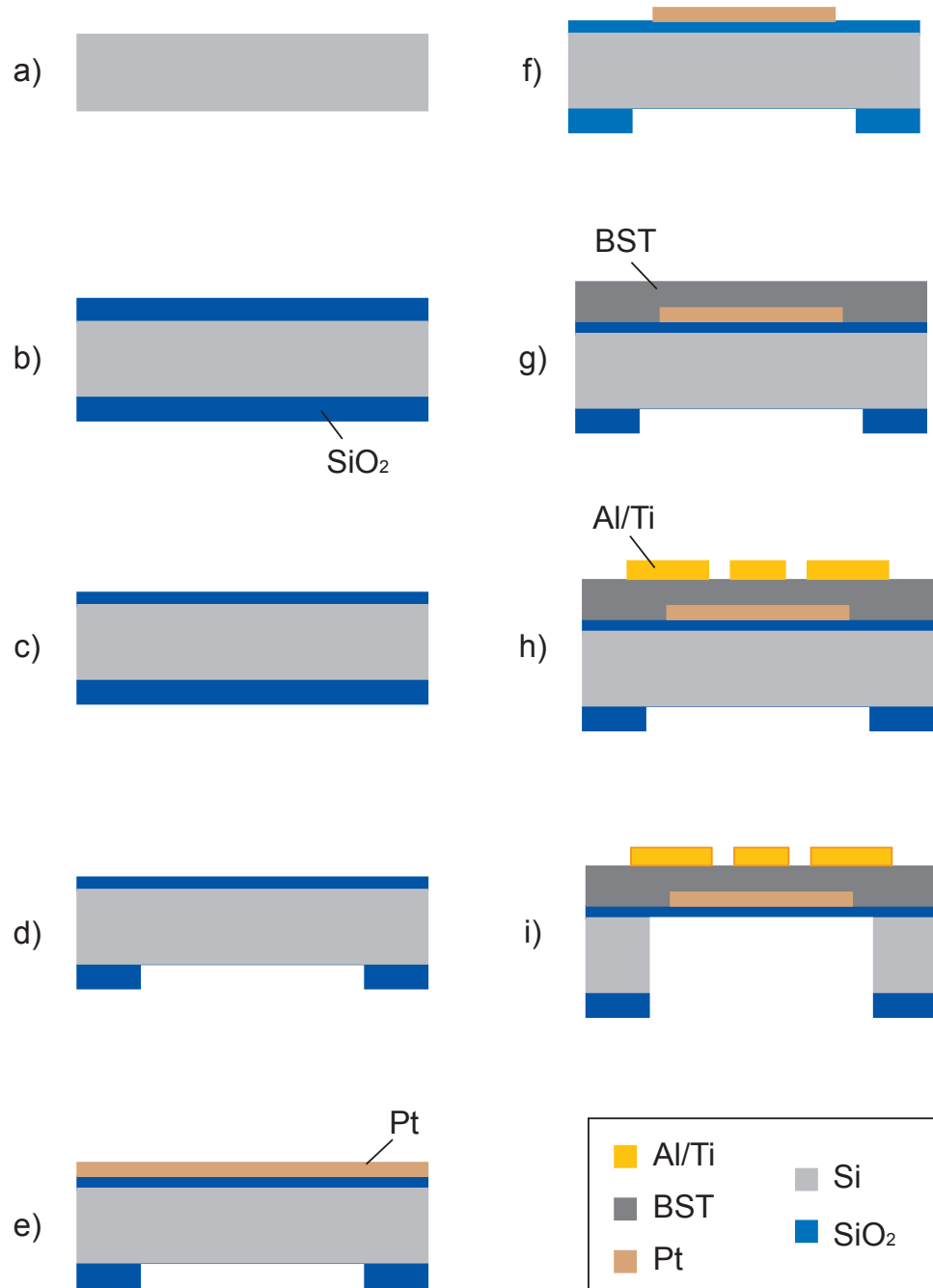


Figure 5.1: Process flow for the fabrication of the BST TFBAR.

## 5. FABRICATION, CHARACTERIZATION AND MODELING OF BST-BASED TFBARS

---

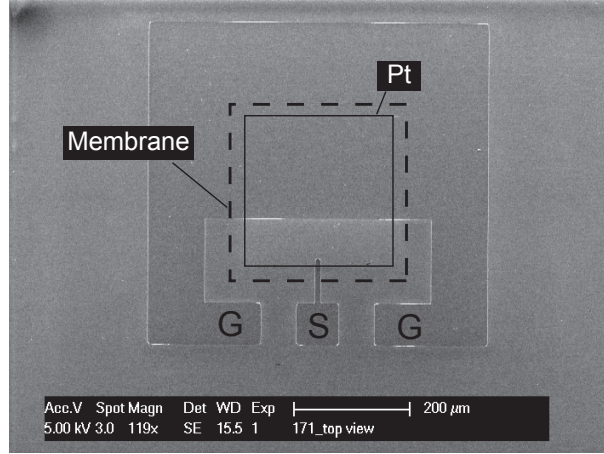


Figure 5.2: An example of a SEM top view image of a BST TFBAR. The floating Pt bottom electrode is centered on the membrane. The device is contacted by G-S-G (Ground-Signal-Ground) probes. The contact to the bottom electrode is realized by capacitive coupling.

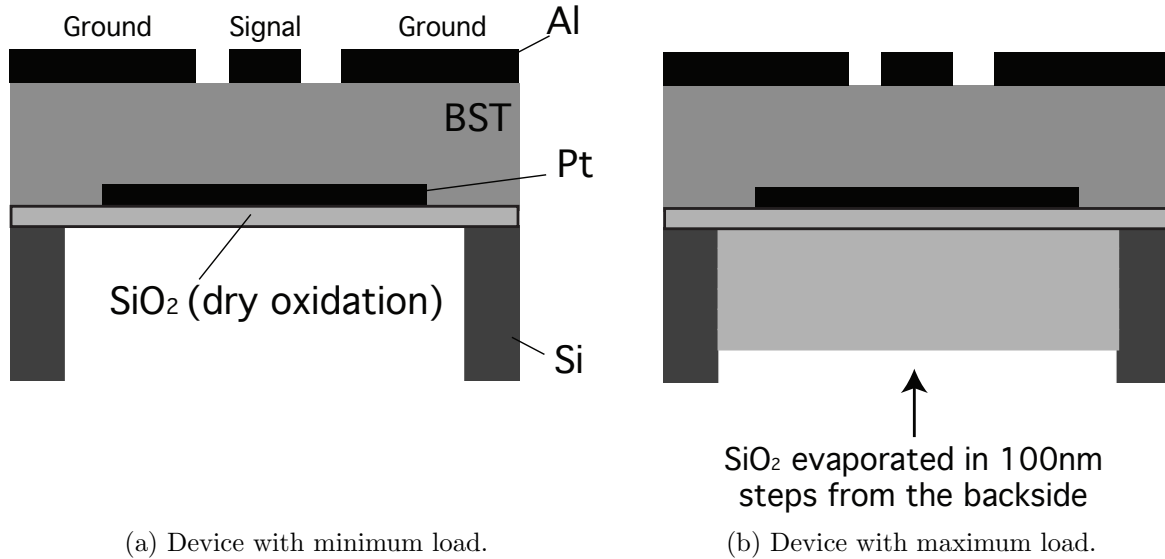


Figure 5.3: Schematic cross-sections of the fabricated device with minimum mechanical load (a) and the device with maximum mechanical load (b).

### 5.2.2 Electrical characterization

The BST TFBARs were electrically characterized using a HP8722D network analyzer (HP, HP8722D, USA) which has a frequency range from 50 MHz to 40 GHz. The devices were contacted using G-S-G (Ground-Signal-Ground) probes (Cascade Microtech, I40-GSG-250, USA) with 250  $\mu\text{m}$  pitch size. Prior to testing, a one port reflection OSL (open, short, 50  $\Omega$  load) calibration was performed using a commercial calibration substrate (Cascade Microtech, 101-190, USA). The 1-port reflection measurements were controlled using a Labview program. The Labview program also calculated the resonators impedance  $Z$  or admittance  $Y$  from the measured reflection coefficient  $S_{11}$ :

$$Z = Z_0 \frac{1 + S_{11}}{1 - S_{11}} \quad (5.2)$$

$$Y = \frac{1}{Z_0} \frac{1 - S_{11}}{1 + S_{11}} \quad (5.3)$$

where  $Z_0 = 50 \Omega$  is the characteristic impedance of the system. To measure the TFBAR under dc bias, a Bias-Tee (SHF AG, BT45B, Germany) was inserted in the electric circuit. The Bias-Tee permits the application of a dc voltage across the rf circuit without affecting the rf signal in the main transmission path. The dc voltage was supplied by a function generator (Agilent, 33120A, USA) and an amplifier (Trek Inc, P0615M, USA). The maximum applicable dc bias was  $\pm 200\text{V}$ .

## 5.3 Results and Discussion

The BST-based TFBARs were characterized at room temperature. At this temperature the BST layer is in the paraelectric phase like shown in Section 4.3.2.

### 5.3.1 Properties of BST-based TFBARs

If a dc bias is applied to the BST thin film, piezoelectric activity is induced in the material through the electrostrictive effect as shown in Chapter 2.2. Due to the induced piezoelectric effect, acoustic resonances appear.

Figure 5.4 shows the admittance of a BST( $x=0.3$ ) TFBAR at zero and under 615 kV/cm dc electric field. At zero bias, no piezoelectric activity is observed and the device works as a capacitor. The application of a dc bias, induces the piezoelectric effect and acoustic resonances appear. If the dc bias is turned off, the acoustic resonances disappear because the BST layer is in the paraelectric phase where no spontaneous polarization exists (i.e. the electromechanical coupling factor  $k_{BST}^2=0$ ). This means that the BST TFBAR can be switched on or off depending on whether a dc bias is applied to the device or not.

Figure 5.5 shows the conductance (real part of admittance) plotted against frequency for different dc electric fields  $E_{dc}$ . The maximum in the conductance corresponds to

## 5. FABRICATION, CHARACTERIZATION AND MODELING OF BST-BASED TFBARS

---

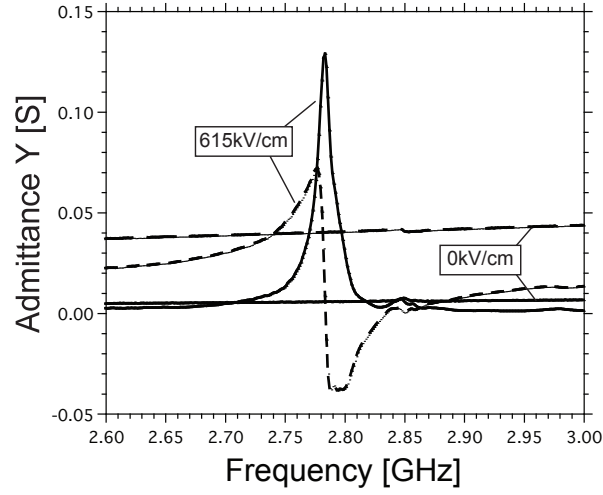


Figure 5.4: Admittance against frequency for the BST( $x=0.3$ )-based TFBAR at zero and 615 kV/cm. The real and imaginary part of the admittance are shown as solid and dashed lines, respectively.

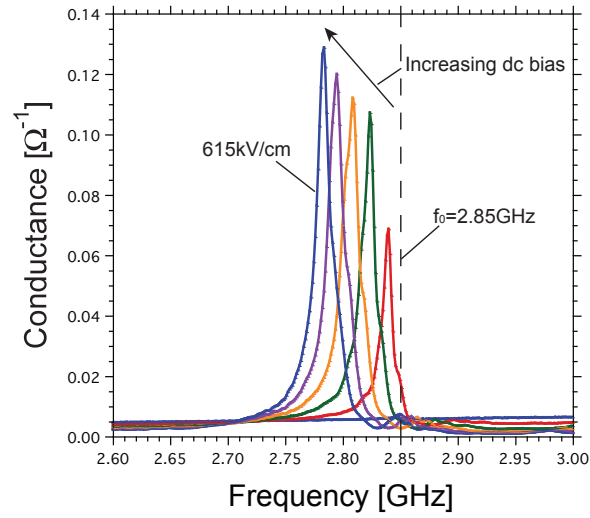


Figure 5.5: Conductance (real part of admittance) against frequency for the BST( $x=0.3$ )-based TFBAR at different dc electric fields.



the resonance frequency  $f_{res}$  [173]. By increasing the dc bias, the acoustic resonances became more pronounced as expected [15; 17]. A dc bias dependence of the resonance frequency was observed. An increase of the dc bias resulted in a clear downward shift of the resonance frequency. The dashed line in Fig. 5.5 shows the resonance frequency at  $E_{dc}$  extrapolated to 0 kV/cm.

Figure 5.6 shows the resistance (real part of impedance) against frequency for different  $E_{dc}$ . The maximum in the resistance corresponds to the antiresonance frequency  $f_{ares}$  [173]. The dashed line in Fig. 5.6 shows the antiresonance frequency at  $E_{dc}$  extrapolated to 0 kV/cm. Like in the case of  $f_{res}$ ,  $f_{ares}$  shifts to lower frequencies with increasing dc bias. Thus, the BST TFBAR is tunable via a dc electric field. In Fig. 5.6 additional resonances can be observed. These parasitic resonances occurred at frequencies above the main resonances and even at higher frequencies than the resonance frequencies at very low dc electric fields. These parasitic resonances were also observed in the real part of the admittance (see Fig. 5.5), but were much less pronounced there. For the moment the origin of these parasitic resonances remains unclear. A possible explanation could be the excitation of spurious resonance modes which is the excitation of lateral Lamb waves in the TE geometry [109; 174; 175]. This phenomenon has often been observed and the effects can be minimized or circumvented by changing the device design [109; 112; 175; 176]. Another possibility for the excitation of parasitic resonances could be due to the in-series connection of two resonators in our device design. Due to our device design the Pt electrode is floating (i.e. at 0 V). At a given time the two in-series connected resonators see different voltage potentials meaning that one resonator sees a positive voltage potential and the other one sees a negative potential. Thus, one of the resonators expands in thickness, whereas the resonator connected in-series is contracting in thickness at the same time. These effects alternate with the ac field, which could give rise to additional resonance modes. To check these hypotheses, resonators with different designs should be fabricated and tested.

Figure 5.7 shows  $f_{res}$  and  $f_{ares}$  against the dc electric field. At a maximum  $E_{dc}$  of 615 kV/cm, the resonance and antiresonance frequency shifted by 66 and 16 MHz, respectively.

Figure 5.8 shows the tuning of the resonance  $n_{res}$  and antiresonance frequencies  $n_{ares}$  as well as the effective electromechanical coupling factor  $k_{eff}^2$  against the dc electric field.

The tuning of the resonance  $n_{res}$  and antiresonance frequencies  $n_{ares}$  were calculated as:

$$n_{res} = \frac{f_{res}(E_{max}) - f(0)}{f(0)} \quad (5.4)$$

$$n_{ares} = \frac{f_{ares}(E_{max}) - f(0)}{f(0)} \quad (5.5)$$

where  $f_{res}(E_{max})$ ,  $f_{ares}(E_{max})$  and  $f(0)$  are the resonance frequency at maximum dc bias,

## 5. FABRICATION, CHARACTERIZATION AND MODELING OF BST-BASED TFBARS

---

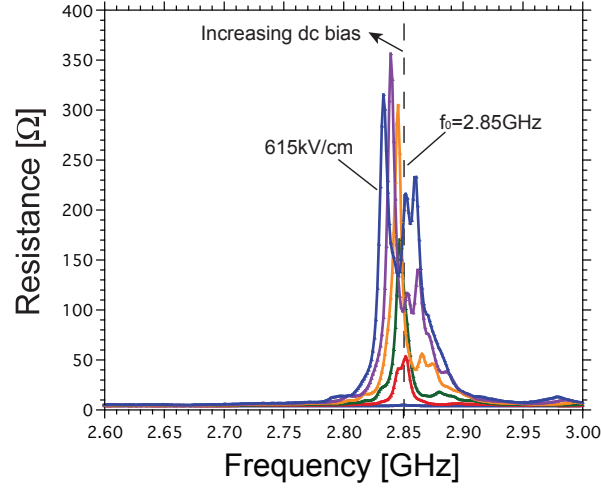


Figure 5.6: Resistance (real part of impedance) against frequency for the BST( $x=0.3$ )-based TFBAR at different dc electric fields.

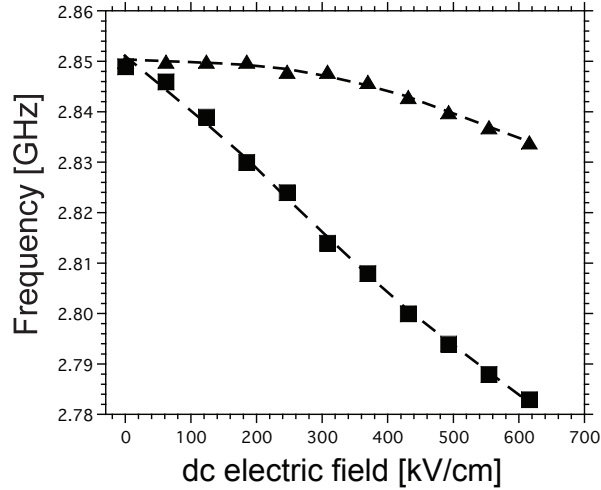


Figure 5.7: Dependence of the resonance (filled squares) and antiresonance frequency (filled triangles) on the dc electric field.

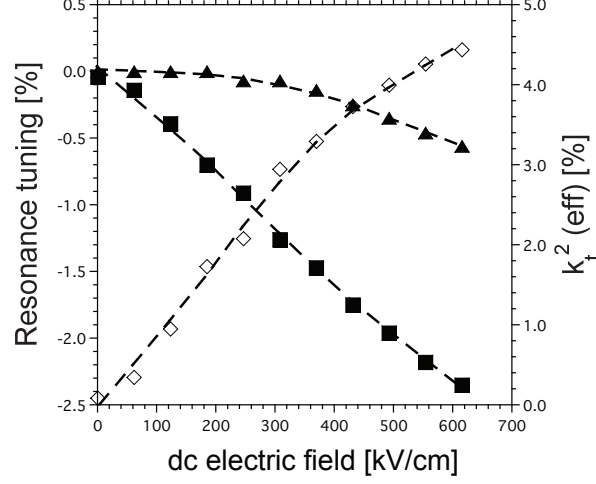


Figure 5.8: Tuning of resonance (filled squares) and antiresonance (filled triangles) frequency and effective electromechanical coupling factor (open diamonds) against dc electric field.

the antiresonance frequency at maximum dc bias, and the resonance frequency at vanishing dc bias, respectively. At  $E_{dc}=615$  kV/cm,  $n_{res}$  and  $n_{ares}$  were -2.4% and -0.6%, respectively. For a maximum dc electric field of 615 kV/cm,  $k_{eff}^2$  increased up to 4.4%. The proportionality factor  $A_t$  between  $k_{eff}^2$  and  $n_r$  from Eq. (3.60) was determined to be about 0.09.

As mentioned above, tuning of TFBARs can also be realized by connecting a tunable capacitor in-series with a static TFBAR. In this case, a reduction of the capacitance of the tunable capacitor leads to an increase in the resonance frequency, whereas the effect on the antiresonance frequency is negligible. Thus, the resonance and antiresonance frequencies are pulled together which means that  $k_{eff}^2$  is reduced. The theoretical tuning range is given by the separation between the resonance and antiresonance frequencies. Using a ZnO FBAR with a tunable capacitor in-series, Pan et al. achieved a maximum tuning of the resonance frequency of about 1.5% [168]. To their knowledge this was the maximum tuning range reported without any additional power consumption. With our BST TFBAR we clearly achieved a wider tuning range also using a dc bias for tuning. In addition, our BST TFBAR showed an appreciable tuning of the antiresonance frequency of 0.6% which is not possible using a static FBAR with a tunable capacitor connected in-series.

The dc bias dependence of the Q-factor at resonance frequency of the TFBAR is shown

## 5. FABRICATION, CHARACTERIZATION AND MODELING OF BST-BASED TFBARS

---

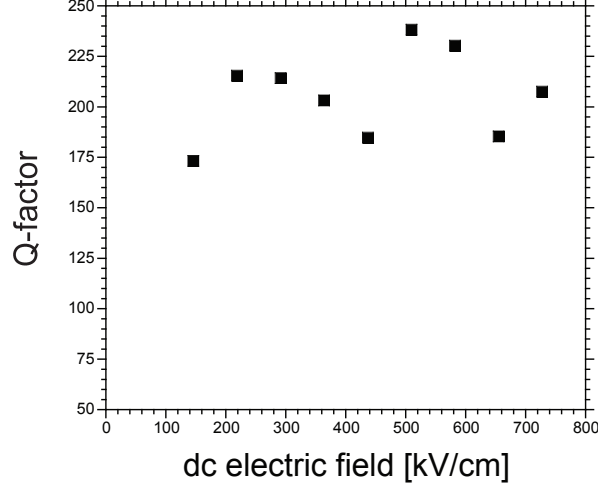


Figure 5.9: Dependence of the Q-factor of the BST TFBAR on the dc electric field.

in Fig. 5.9. The Q-factor was calculated as:

$$Q = \frac{f_{res}}{2} \frac{\partial \phi}{\partial f} \bigg|_{f_{res}} \quad (5.6)$$

where  $\phi$  and  $f$  are the impedance phase of the TFBAR and the frequency, respectively. The Q-factor was about 200. The values of the Q-factor showed some scattering for different dc electric fields which cannot be explained for the moment and needs further investigation. The scattering might be due to a measurement artefact or some parasitic effects. Tunable TFBARs that utilize an in-series connected tunable capacitor observe a reduction of the Q-factor of the static FBAR by the in-series connection of the tunable capacitor. The Q-factor of the tunable FBAR of Pan et al. varied between 160 and 300 depending also on the dc bias [168]. These values are not significantly better than the values of our BST TFBAR.

An advantage of using materials in the paraelectric instead of the ferroelectric phase for tunable TFBARs is the non-hysteretic behavior of the dc bias dependent properties. In TFBARs based on ferroelectric PZT it has been observed that the resonance and antiresonance frequencies are tunable by a dc electric field, but the tuning is hysteretic [100; 177; 178]. This can pose problems for the device control. In addition, in ferroelectric materials the flexibility of switching the resonator on or off by a dc electric field is lost. Figure 5.10 shows the dependence of the resonance and antiresonance frequencies of a BST TFBAR on sweeping the dc bias forward and backward. As expected, no hysteresis associated with the tuning of the acoustic resonances could be detected.

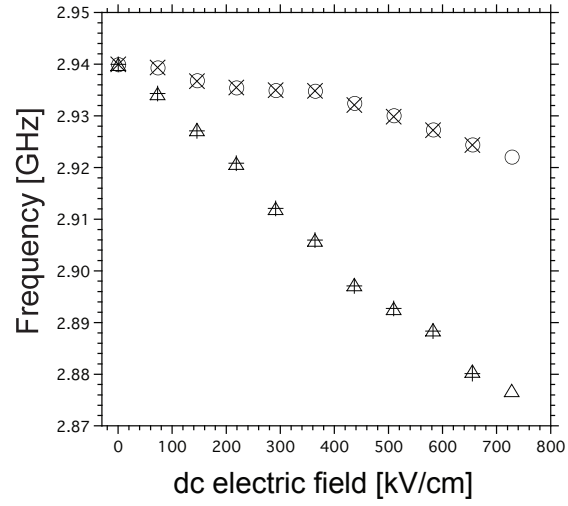


Figure 5.10: Non-hysteretic dc bias dependence of the resonance and antiresonance frequencies. The resonance frequency on the forward and backward sweep of the dc bias is shown as open triangles and plus signs, respectively. The antiresonance frequency on the forward and backward sweep of the dc bias is shown as open circles and crosses, respectively.

## 5. FABRICATION, CHARACTERIZATION AND MODELING OF BST-BASED TFBARS

---

This is a clear advantage over tunable TFBARs based on ferroelectric materials due to the reasons mentioned above.

### 5.3.2 Modeling of BST-based TFBARs

The BST TFBAR was modeled under different dc bias fields and mechanical loading conditions in order to extract relevant properties of the BST layer, verify the model of the electrical tuning of the dc bias dependence of the field-induced acoustic resonances developed in Chapter 3 [179], and to estimate the effect of the mechanical load on the tuning performance of the device. The mechanical load comprises all non-piezoelectric layers like electrodes, membrane support layers, etc. in the TFBAR device. The device was modeled by calculating its electrical impedance with the formula developed by Lakin for a composite resonator structure [110]:

$$Z = \frac{1}{i\omega C} \left[ 1 - k_{BST}^2 \frac{\tan \phi}{\phi} \frac{(z_b + z_t) \cos^2 \phi + i \sin 2\phi}{(z_b + z_t) \cos 2\phi + i(z_b z_t + 1) \sin 2\phi} \right] \quad (5.7)$$

where  $\omega$  is the angular frequency,  $C$  is the (clamped) capacitance, and  $k_{BST}^2$  is the intrinsic electromechanical coupling factor of the BST layer. The phase  $\phi$  across the BST layer is given by:

$$\phi = \frac{kt_{BST}}{2} = \frac{\omega t_{BST}}{2v_{BST}} \quad (5.8)$$

where  $k$ ,  $t_{BST}$  and  $v_{BST}$  are the propagation constant, the thickness, and the sound velocity of the BST layer at constant electric displacement  $D$ , respectively. The variables  $z_b$  and  $z_t$  are the normalized mechanical input impedances of the layers attached to the BST layer from the bottom and the top, respectively. These mechanical loading impedances are normalized with the mechanical impedance of the BST layer  $Z_{BST}$ :

$$z_b = \frac{Z_{in,b}}{Z_{BST}} \quad (5.9)$$

$$z_t = \frac{Z_{in,t}}{Z_{BST}} \quad (5.10)$$

The mechanical impedance of the BST layer is defined as:

$$Z_{BST} = \rho v_{BST} \quad (5.11)$$

where  $\rho$  is the density of the BST layer. We calculated the mechanical input impedance  $Z_{in}$  of each loading (non-piezoelectric) layer by using the transmission line equation as demonstrated in Ref. [110].

Mechanical losses were introduced as an imaginary part into the phase of the BST layer as proposed by Lanz [122]:

$$\phi_{loss} = \phi_{lossless} \left( 1 - \frac{i}{2Q} \right) \quad (5.12)$$

where  $\phi_{loss}$  and  $\phi_{lossless}$  are the phases across the BST layer with and without acoustic losses, respectively.  $Q$  corresponds to the mechanical Q-factor of the BST layer at antiresonance frequency. In our case a value of  $Q = 100$  gave the best fit to the experimental data. The mechanical losses of the layers attached to the BST layers were neglected. The acoustic properties of each layer used in the modeling are shown in Tab. 5.1.

The sound velocity of the BST thin film at zero dc bias  $v_{BST}^0$  can be estimated by solving the Christoffel equation. The sound velocity of a quasi-longitudinal wave traveling in an arbitrary direction in cubic crystals varies between the sound velocity of the wave traveling in the (100) and the (110) direction of the crystal [139]. The sound velocity of a material can be calculated from its tensor of elastic constant  $c_{ijkl}$  and its density  $\rho$ . The components of the tensor of the elastic constant  $c_{ijkl}$  have been calculated for BST(x=0.3) in virtual crystal approximation, i.e. using linear interpolation between the values of parameters between the end members of the composition. With this method, the elastic constants  $c_{11}$ ,  $c_{12}$  and  $c_{44}$  were calculated to be 283, 124 and 113 GPa, respectively (see Table 3.2). The density was calculated from the mass and the lattice parameters of the BST(x=0.3) unit cell, which resulted in a value of 5413 kg/m<sup>3</sup>. The sound velocity of a longitudinal wave traveling in the (100) and (110) can be calculated as:

$$v_{100}^0 = \sqrt{\frac{c_{11}}{\rho}} \approx 7200 \text{ m/s} \quad (5.13)$$

$$v_{110}^0 = \sqrt{\frac{c_{11} + c_{12} + c_{44}}{\rho}} \approx 10800 \text{ m/s} \quad (5.14)$$

For the modeling, a sound velocity at zero dc bias  $v_{BST}^0$  of 6840 m/s for the BST layer gave the best fit to the experimental data. This value for the BST sound velocity is reasonable considering the (100) and (111) texture of the BST thin film and a certain variation of the BST film thickness across the sample. The sound velocity of the BST layer is dc bias dependent:

$$v_{BST} = \sqrt{\frac{c_{BST}^D}{\rho}} = v_{BST}^0 \left( 1 - k_{BST}^2 \left( \gamma_t + \frac{\mu}{2} \right) \right) \quad (5.15)$$

where the parameters  $\gamma_t$  and  $\mu$  are given in Chapter 3.3. The sound velocity of the SiO<sub>2</sub> layer is  $\approx 5950$  m/s [180]. This value of the sound velocity gave a good fit to the data of the device shown in Fig. 5.3a, where the 100 nm thick SiO<sub>2</sub> layer was deposited by dry oxidation.

The values of the capacitance  $C$  and the permittivity  $\varepsilon$  used in the model were taken from experimental measurements. Due to the dc bias dependence of  $v_{BST}$ , it follows that  $Z_{BST}$  and  $\phi_{BST}$  are also dc bias dependent which we took into account in the modeling. The use of the parameters  $q$ ,  $m$  and  $k_{BST}^2$  is discussed below.

The dc electric field dependence of the performance of the system was introduced in the modeling via a variation of the intrinsic electromechanical coupling factor  $k_{BST}^2$  of the

## 5. FABRICATION, CHARACTERIZATION AND MODELING OF BST-BASED TFBARS

Table 5.1: Material parameters used in the modeling of the BST TFBAR. The sound velocity and the mechanical impedance of BST correspond to the value at zero dc bias.

Material	t [nm]	mechanical impedance $\times 10^6$ [kg/m <sup>2</sup> s]	v [m/s]
Al	300	17.4	6380
BST	650	35.1	6840
Pt	100	57.6	2680
SiO <sub>2</sub> (dry oxidation)	100	12.6	5950
SiO <sub>2</sub> (evaporation)	variable	9.9	4500

BST layer in Eq. (5.7). The resonance and antiresonance frequencies were determined as the maximum of the real part of the modeled admittance and impedance, respectively. From these values, the tuning of the resonance and antiresonance frequencies as well as the modeled effective electromechanical coupling factor  $k_{eff}^2(mod)$  were calculated. The  $f_{res}$  and  $f_{ares}$  measured on the structure shown in Fig. 5.3a for different applied dc electric fields  $E_{dc}$  were fit by changing  $k_{BST}^2$  in Eq. (5.7). Thus, the dependence of  $k_{BST}^2$  on  $E_{dc}$  has been determined. At this point we were able to check a prediction of the theory of non-loaded tunable TFBARs, specifically the relation [179]:

$$A_t = \frac{k_{BST}^2}{n_r} \quad (5.16)$$

between  $k_{BST}^2$  and the relative dielectric tunability  $n_r$  of the BST layer. We have found this relation satisfied to within the experimental error. However, the obtain value  $A_t = 0.09$  is smaller than our estimates obtained from the thermodynamical parameters of BST (x=0.3) shown in Chapter 3. Here, for thin films of (001) and (111) orientations, the values  $A_t^{(001)} \approx 0.5$  and  $A_t^{(111)} \approx 0.2$ . were found [179]. For the moment we cannot comment on this difference, which may be attributed to a poor knowledge of the thermodynamical parameters of the material.

Figure 5.11 shows the modeled and experimentally determined dependence of the resonance and antiresonance frequencies on the dc electric field. The value of  $q$  in Eq. (3.38) was taken from Table 3.2. The value of  $q$  depends on the orientation of the BST thin film and varies for BST(x=0.3) thin films between  $1.08 \times 10^{10}$  and  $2.61 \times 10^{10}$  m/F for BST films with (111) and (001) orientation. Considering the (001) and (111) texture of our BST thin film, we considered  $q=1.8 \times 10^{10}$  m/F to be a reasonable value for the modeling. The parameter  $m$  was used as a fitting parameter (for the dc bias dependence of the antiresonance frequency). A value of  $m=5 \times 10^{11}$  m/F gave the best fit to our data. The value of the components of  $m$  are not known. Vendik et al. estimated the averaged values of  $m$  from literature data on the pressure dependence of the permittivity for BST(x=0) and BST(x=1) [135]. The averaged values they obtained were  $-(4 \text{ to } 7) \times 10^{11}$  m/F and  $(3 \text{ to } 8) \times 10^{11}$  m/F for BST(x=0) and BST(x=1), respectively. Vendik et al. used a



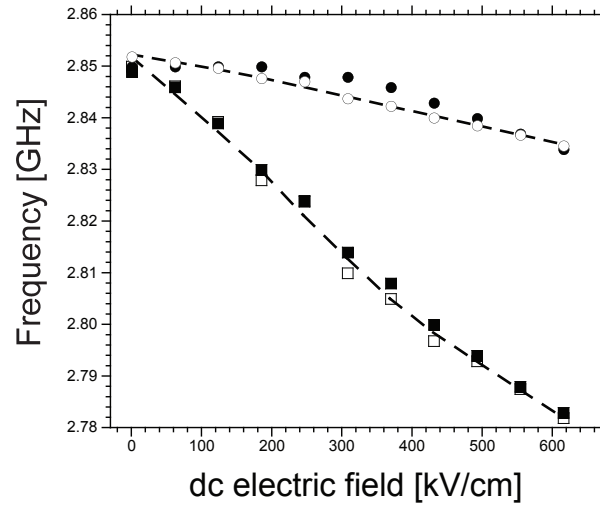


Figure 5.11: Experimental and modeled values for the dc bias dependence of the resonance and antiresonance frequencies. The experimental values for the resonance and antiresonance frequencies are shown as (filled squares) and (filled circles), respectively. The modeled values of the resonance and antiresonance frequencies are shown as (open squares) and (open circles), respectively.

## 5. FABRICATION, CHARACTERIZATION AND MODELING OF BST-BASED TFBARS

---

positive sign of the term  $\frac{1}{2}m_{ijklmn}u_{ij}u_{kl}P_mP_n$  in the Landau free energy expansion (see Eq. (3.1)) which means that their value of  $m$  is of the opposite sign in comparison to our approach. Thus, our value of  $m=5 \times 10^{11}$  m/F is of the same order of magnitude and sign as the estimates of Vendik et al. As can be seen from Fig. 5.11 our developed model can precisely describe the properties of the real device.

Using our model of the electrical tuning of the dc bias induced acoustic resonances together with experimental data on the field dependence of the resonance and antiresonance frequencies offers a way to directly evaluate the magnitude of the tensor components of  $m$ .

As mentioned above,  $k_{BST}^2$  was de-embedded by using it as a fitting parameter in Eq. (5.7). For the device design shown in Fig. 5.3a,  $k_{BST}^2$  was, within our accuracy, equal to  $k_{eff}^2$  indicating that the dc bias dependent properties of the BST layer are efficiently used in the device.

### 5.3.3 Effect of mechanical load on TFBAR characteristics

The effect of the mechanical load on the tuning performance of the BST TFBAR was studied theoretically and experimentally. For the experimental part, the mechanical load of the device shown in Fig. 5.3a was increased step-wise by evaporating 100 nm of SiO<sub>2</sub> on the backside of the TFBAR through the micromachined hole on the backside of the wafer as shown in Fig. 5.3b. A calibration was performed to ensure that exactly 100 nm SiO<sub>2</sub> are deposited by each step. After each evaporation step, the device was electrically characterized.

The increase in the mechanical load was modeled as described in Section 5.3.2 by increasing the thickness of the SiO<sub>2</sub> layer in the system. Since the SiO<sub>2</sub> layers in the structure were deposited by two different deposition methods (dry oxidation and evaporation), we could expect different acoustic properties of the different SiO<sub>2</sub> layers. For example, evaporated SiO<sub>2</sub> layers can exhibit a reduced elastic constant [181], which results in a reduced sound velocity of the layer. Thus, we modeled the SiO<sub>2</sub> layers deposited by dry oxidation and evaporation as two different layers with different mechanical properties. For the evaporated SiO<sub>2</sub>, a value of 4500 m/s for the sound velocity and  $9.9 \times 10^6$  kg/m<sup>2</sup>s for the mechanical impedance gave a good fit to our experimental data. The mechanical impedance of the evaporated SiO<sub>2</sub> layers was calculated with the sound velocity of 4500 m/s taking the theoretical density of the SiO<sub>2</sub> as 2201 kg/m<sup>3</sup>.

Figure 5.12 shows the tuning of the resonance frequency and the relative tunability  $n_r$  as functions of the dc electric field for the devices with SiO<sub>2</sub> layers which are 100 nm and 700 nm thick. As expected, the relative dielectric tunability of the material is not affected by the mechanical load. For the devices with the two different mechanical loads, it was  $\approx 50\%$  at a maximum dc electric field of 615 kV/cm. The small difference in the relative tunability of the two measurements can be attributed to a change in temperature between the measurements or small calibration errors. In contrast to the relative tunability, the

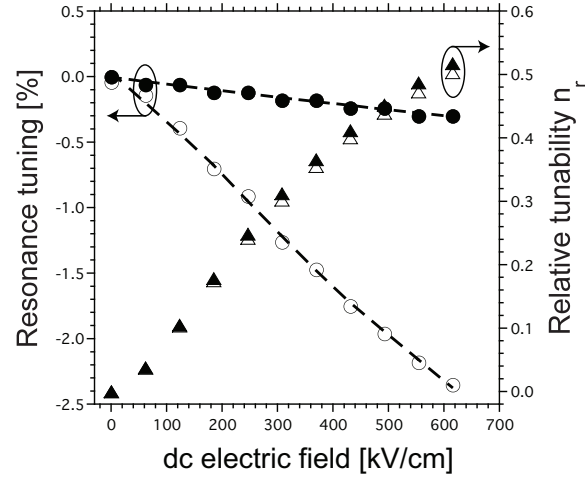


Figure 5.12: Dependence of the relative dielectric tunability  $n_r$  and the tuning of the resonance frequency on the dc electric field for BST TFBARs with 100 and 700 nm thick  $\text{SiO}_2$  layers. The relative tunabilities of the BST TFBAR with 100 nm  $\text{SiO}_2$  (open triangles) and with 700 nm  $\text{SiO}_2$  (filled triangles) are essentially the same at a given dc electric field. The tuning of the resonance frequency for the BST TFBAR with 100 nm  $\text{SiO}_2$  (open circles) is stronger than the tuning of the resonance frequency of the BST TFBAR with 700 nm  $\text{SiO}_2$  (filled circles).

## 5. FABRICATION, CHARACTERIZATION AND MODELING OF BST-BASED TFBARS

---

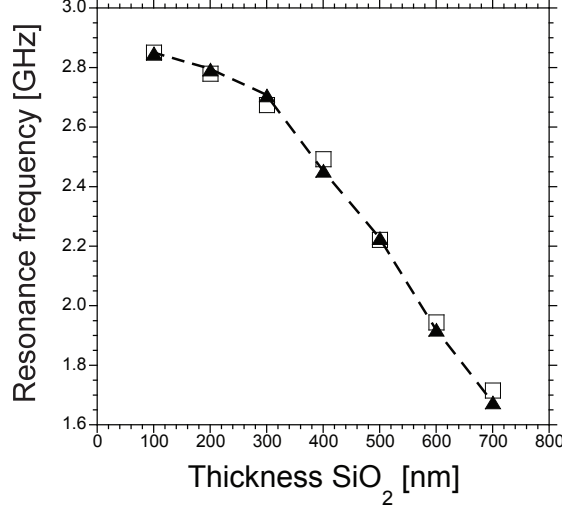


Figure 5.13: Modeled (open squares) and experimental (filled triangles) values of the resonance frequency at  $E_{dc}$  extrapolated to 0 kV/cm for different thicknesses of the SiO<sub>2</sub> layer attached to the BST TFBAR.

tuning of the resonance frequency is strongly reduced for the device with a 700 nm thick SiO<sub>2</sub> layer. From our theoretical analysis we expect that the magnitude of the intrinsic electromechanical coupling factor  $k_{BST}^2$  in the BST layer should be the same for both devices, since the layer shows the same relative tunability  $n_r$  [179]. Thus, we conclude that the mechanical load leads to a strong reduction of experimentally determined  $k_{eff}^2(exp)$  and also of the tuning of the acoustic resonances in the device.

Figure 5.13 shows the experimental and modeled results for the resonance frequency of the BST TFBAR with different SiO<sub>2</sub> thicknesses at a dc bias extrapolated to the value  $E_{dc}=0$  kV/cm. The modeled values fit the experimental values very well. The small differences between the experimental and modeled values can be due to inaccurate determination of the thicknesses of the different layers of the device as well as inaccurate material data used in the modeling.

Figure 5.14 illustrates the experimental and modeled data of the tuning of the resonance and antiresonance frequencies of the BST TFBAR with different SiO<sub>2</sub> thicknesses. Up to a thickness of 300 nm of SiO<sub>2</sub>,  $|n_{res}| \geq 2.0\%$  and  $|n_{ares}| \geq 0.5\%$ . For a SiO<sub>2</sub> thickness larger than 300 nm,  $n_{res}$  and  $n_{ares}$  are strongly reduced. We attribute this behavior with increasing mechanical load to two effects: First, the increase and asymmetric distribution of the mechanical load leads to a reduction in  $k_{eff}^2$ , which primarily reduces  $n_{res}$ . Second, the increase of the mechanical load leads to a reduced field-induced change of the sound velocity in the TFBAR structure for a given dc electric field, which manifests itself

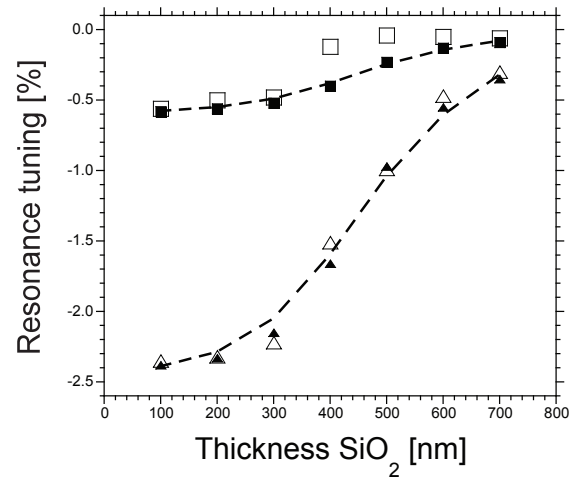


Figure 5.14: Modeled and experimental dependence of the tuning of resonance and antiresonance frequencies on the thickness of the SiO<sub>2</sub> layer. The experimental values for the tuning of the resonance and antiresonance frequencies are shown by (open triangles) and (open squares), respectively. The modeled values for the tuning of the resonance and antiresonance frequencies are shown by (filled triangles) and (filled squares), respectively.

## 5. FABRICATION, CHARACTERIZATION AND MODELING OF BST-BASED TFBARS

---

in a reduction of  $n_{ares}$ .

From the modeling,  $k_{BST}^2$  of the BST layer was determined to be 4.4% at a maximum dc electric field of 615 kV/cm. For a thickness of SiO<sub>2</sub> of up to 300 nm,  $k_{eff}^2(exp) \geq 4\%$ , which means that the effect of the mechanical load on  $k_{eff}^2(exp)$  is rather weak. We attribute this observation to a rather symmetrical distribution of the mechanical load via the following arguments. In this case, the maximum strain associated with the traveling acoustic wave of fundamental mode ( $\lambda/2$ ) occurs in the BST layer. This results in a strong coupling in the BST layer, and therefore in a large  $n_{res}$ . A further increase of the SiO<sub>2</sub> load, leads to an asymmetric distribution of the mechanical load. In this case, the point of maximum strain in the TFBAR structure is displaced and might not occur in the BST layer. In this case, the coupling in the BST layer is substantially reduced which leads to a reduced  $n_{res}$ .

The reduction of  $n_{ares}$  with increasing SiO<sub>2</sub> load is due to the reduced impact of the dc bias on the change of the sound velocity in the TFBAR structure. If we consider only the BST layer, the antiresonance frequency is given by:

$$f_{ares} = \frac{v_{BST}}{2t_{BST}} \quad (5.17)$$

The tuning of the antiresonance frequency is due to the dc bias dependence of the sound velocity of the BST thin film:

$$\frac{\Delta f_{ares}}{f_{ares}} = \frac{\Delta v_{BST}}{v_{BST}^0} \quad (5.18)$$

The layers loading the piezoactive BST layer do not show a dc bias dependence of the sound velocity. This means that with a mechanical load, one reduces the fraction of the traveling distance of the acoustic wave, where the sound velocity can be tuned. In this case the tuning of the antiresonance frequency  $\Delta f_{ares}/f_{ares}$  can be described as:

$$\frac{\Delta f_{ares}}{f_{ares}} = \frac{\Delta v_{BST}}{v_{BST}^0} \frac{\frac{t_{BST}}{v_{BST}^0}}{\frac{t_{BST}}{v_{BST}^0} + \frac{t_{load}}{v_{load}}} \quad (5.19)$$

where  $t_{load}$  and  $v_{load}$  correspond to the thickness and the sound velocity of the loading layer. Equation (5.19) shows that for a given  $\Delta v_{BST}$ , the tuning of the antiresonance frequency is reduced with increasing mechanical load. This explains our experimental and modeled results where we observed that the tuning of the antiresonance frequency reduces gradually with increasing mechanical load. For the maximum mechanical load we investigated, the tuning of the antiresonance frequency is smaller than 0.05%.

All in all, a qualitative difference in the impact of the progressive mechanical loading on the tuning of resonance and antiresonance frequencies is expected: the deterioration of the tuning of the latter with loading should be rather gradual, whereas, for the former, this effect should start slowly with a further acceleration.

The modeling enabled us to de-embed the intrinsic electromechanical properties of the BST layer without any mechanical load meaning a BST layer without electrodes and SiO<sub>2</sub> layer attached to it.

Comparing these parameters of the BST layer with those of the device with the smallest mechanical load (the device shown in Fig. 5.3a), we found that  $k_{BST}^2$  of the BST layer is equal, within our accuracy, to  $k_{eff}^2$  of the device. But the non-loaded BST layer exhibits a slightly enhanced tuning of both resonance and antiresonance frequencies in comparison to the device. The  $n_{res}$  and  $n_{ares}$  of the single BST layer were determined to be -2.5% and -0.7%, respectively, whereas the device with the weakest mechanical load (electrodes + 100 nm SiO<sub>2</sub>) exhibited  $n_{res}$  and  $n_{ares}$  of -2.4% and -0.6%, respectively. This means that the mechanical load of the device shown in Fig. 5.3a does not significantly reduce the tuning characteristics of the device and that the intrinsic field dependent electromechanical properties of the BST layer are efficiently used. The less sensitivity of  $k_{eff}^2$  on the minimal load in comparison to  $n_{res}$  and  $n_{ares}$  can be readily rationalized in the lines of the above discussion of the two kinds of the loading effect. Small and identical reductions of  $n_{res}$  and  $n_{ares}$  are due to the reduction of the tunability of the sound velocity given by Eq. (5.15), whereas the  $k_{eff}^2$  is virtually not affected, which agrees with the above remarks about the efficiency of the electromechanical coupling of the device.

## 5.4 Summary and Conclusions

In this chapter we presented the fabrication, characterization, and modeling of a tunable, non-hysteretic TFBAR based on a BST thin film.

Piezoelectricity is induced in the BST layer by a dc bias through the electrostrictive effect. The induced acoustic resonances can be tuned by the dc electric field. A tuning of -2.4% and -0.6% for the resonance and antiresonance frequencies, respectively, has been achieved at a dc electric field of 615 kV/cm. The tuning of the BST layer is non-hysteretic, which is an advantage over tunable TFBARs based on materials in the ferroelectric phase like PZT. The Q-factor of the device was about 200. Comparing the performance of our BST TFBAR with the performance of varactor-tuned TFBARs, our BST TFBAR showed a much stronger tuning of the resonance frequency. The antiresonance frequency of the BST TFBAR is also tunable, which is not possible in static TFBARs without additional components.

We also investigated experimentally and theoretically the effect of mechanical loading on the tuning of the resonance and antiresonance frequencies of the BST TFBAR. The combination of experimental and theoretical work allowed us to extract the intrinsic tuning properties of a non-loaded BST layer. We found that the tuning of both resonance and antiresonance frequencies are reduced by the mechanical load attached to the BST layer. The tuning of the antiresonance frequency is affected by the mechanical load via a reduction of the fraction of the traveling distance of the acoustic wave where the sound

## 5. FABRICATION, CHARACTERIZATION AND MODELING OF BST-BASED TFBARS

---

velocity is tuned. The tuning of the resonance frequency is affected by the mechanical load via a reduction of the effective electromechanical coupling in the device. It has been shown that, though the mechanical loading reduces the acoustical tunability of the TFBAR, the impact of the load of a thickness comparable to that of the BST layer can be rather mild when it is distributed around the BST layer in a rather symmetric way. The tuning properties of the BST TFBAR with the smallest mechanical load (as shown in Fig. 5.3a) we investigated, exhibited tuning characteristics which are very close to the intrinsic properties of the BST layer. All in all, we can say that using BST as an active material in TFBARs allows the development of tunable, non-hysteretic TFBARs of reduced size in comparison to typical devices based on AlN or ZnO thin films.



# Chapter 6

## Integration of micromachined coplanar capacitors on silicon

In this chapter we present the fabrication and characterization of a coplanar capacitor on silicon. Micromachining was used to reduce parasitic effects stemming from the substrate, which enhanced the performance of the device.

### 6.1 Introduction

Tunable BST thin film capacitors are typically fabricated in the parallel-plate geometry. In this geometry the dc electric field between the bottom and top electrode is efficiently applied to the BST layer in-between, which results in a good tunability of the device. But the parallel-plate geometry also has some drawbacks. First, the fabrication of the devices is rather complicated and involves several photolithography and etching processes. Second, the electrode contribution to the device losses is significant. A solution to this problem is to increase the thickness of the electrodes [21; 124]. In this case the sheet resistivity of the metal electrode decreases, which reduces the contribution to the loss tangent of the device. However, integration of a thick bottom electrode is challenging. The electrode material should be a very good conductor and be resistant to oxidation at high deposition temperatures. Noble metals like Au and Pt have a good resistance to oxidation, but are very expensive which is problematic when thick electrodes are needed. The high thickness of the electrode can also lead to a high roughness of the layer, which is not optimal for BST thin film growth.

An alternative approach to the parallel-plate capacitor is the coplanar capacitor design. Here, the BST thin film is deposited on a substrate and the dc electric field is applied between two metal electrodes on the top of the BST layer. The two metal electrodes are separated by a small gap typically below 10  $\mu\text{m}$ . The advantage of this device design is the simple fabrication (normally only one photolithography step is needed) and the less

## 6. INTEGRATION OF MICROMACHINED COPLANAR CAPACITORS ON SILICON

---

significant contribution of the electrodes to the loss tangent of the device. Disadvantages are the typically lower dc electric fields in the active area of the device in comparison to the parallel-plate geometry for a given dc bias voltage and a contribution of the non-tunable capacitance of the substrate to the capacitance of the device. This typically lowers the tunability of a capacitor in the coplanar geometry.

Tunable BST capacitors in the coplanar geometry are typically fabricated on single-crystal substrates. These substrates typically have a low permittivity which helps to concentrate the dc electric field in the BST layer and to reduce the contribution of the non-tunable substrate capacitance to the device. Moreover, a BST thin film of very high quality, even epitaxial film growth, can be achieved on single-crystal substrates. Disadvantages of these substrates are their small size, high cost, and the incompatibility with standard semiconductor process technology.

An alternative would be to use Si as a substrate. The reports on tunable BST coplanar capacitors on Si are very rare. The reasons are that BST reacts with Si at high temperatures so that appropriate buffer layers are needed. In addition, the electric field penetrates through the substrate, which leads to a contribution to the device losses due to the conductivity of the Si substrate. This loss contribution typically increases with decreasing frequency. This problem could be solved by depositing a rather thick layer of a material with low permittivity between the BST layer and the substrate. This layer could be  $\text{SiO}_2$ , for example. The problem here is that the deposited  $\text{SiO}_2$  is typically amorphous, which is not ideal for the nucleation of high quality BST in thin film form.

Having the above mentioned discussion in mind, we decided to use the possibilities of micromachining to fabricate coplanar BST capacitors on silicon. Our idea was to deposit a thin epitaxial seeding layer (in our case  $\text{Y}_{0.09}\text{Zr}_{0.91}\text{O}_{1.96}$  (YSZ)) on the Si substrate to avoid the reaction between Si and BST and to have a high quality surface for the nucleation of the BST thin film. The Si substrate was removed under the active area of the device with micromachining technology to avoid the parasitic contribution of the Si substrate to the loss tangent and the capacitance of the device.

In this chapter we report on the fabrication and electrical characterization of such a micromachined coplanar BST capacitor on Si. We prove that our developed concept works and compare the properties of the micromachined coplanar capacitor with a non-micromachined one (a coplanar capacitor with Si under the active area of the device). We show that the tunability and the loss tangent of the micromachined capacitor are improved in comparison to the non-micromachined capacitor. Since the properties of the BST thin film used in both types of devices are identical, the observed differences are purely due to device design. The use of micromachining technologies enabled a reduction of parasitics from the Si substrate.

## 6.2 Experimental details

### 6.2.1 Fabrication of the devices

The micromachined coplanar BST capacitors were integrated on high-resistive Si substrates. The same wafers as for the BST TFBARs were used for the fabrication of the devices (Fig. 6.1a). Through wet oxidation of the wafers, as described in Chapter 5.2.1.2,  $2.5\ \mu\text{m}$   $\text{SiO}_2$  were deposited on the wafer surfaces (Fig. 6.1b). The  $\text{SiO}_2$  layer on the top side of the wafer was removed in a BHF(7:1) solution. The  $\text{SiO}_2$  layer on the backside of the wafer was patterned as described in Chapter 5.2.1.3. With this process, rectangular openings of  $400\ \mu\text{m}$  and  $20\ \mu\text{m}$  edge length were etched into the  $\text{SiO}_2$  layer on the backside of the wafer (Fig. 6.1c). Then, the 4 inch wafer was cut into square-shaped samples of about 1.2 cm edge length to have a compatible substrate size for the PLD equipment. First, an epitaxial  $\text{Y}_2\text{O}_3$ -stabilized  $\text{ZrO}_2$  (YSZ) layer with a maximum thickness of 10 nm was deposited on the Si wafer (Fig. 6.1d). The YSZ layer was deposited at  $T=800\ ^\circ\text{C}$  at  $p(\text{O}_2)=5\times 10^{-4}$  Torr. The laser energy and the repetition rate were set to 220 mJ and 7 Hz, respectively. The YSZ layer was deposited as a template layer for the BST thin film growth. We expected that the BST thin film quality could be improved in comparison to a BST thin film deposited on amorphous  $\text{SiO}_2$ . After YSZ deposition, the substrate was annealed in flowing  $\text{O}_2$  in a tube furnace. The purpose of this annealing step is to oxidize the Si surface under the YSZ layer for the following reasons: First, the  $\text{SiO}_2$  served as an etch stop for the Bosch process used to liberate the membrane in the last fabrication step of the device. Second, the low permittivity of the  $\text{SiO}_2$  helped to concentrate the applied dc electric field in the active BST layer and therefore helped to reduce the effect of parasitics stemming from the Si substrate. The annealing was performed at  $T=1000\ ^\circ\text{C}$  for 5 h. This resulted in an estimated  $\text{SiO}_2$  thickness of  $250\ \mu\text{m}$ . The standard enthalpy of formation of  $\text{SiO}_2$  is  $-910.86\ \text{kJ/mol}$  [182]. The oxidation of the Si surface under the YSZ layer is possible due to the high oxygen conductivity of YSZ [183; 184; 185] and the thin layer thickness ( $t \leq 10\ \text{nm}$ ).

BST thin films of  $x=0.7$  composition were deposited on the substrate. This composition was chosen because of its higher permittivity at room temperature in comparison to the composition  $x=0.3$ , as shown in Chapter 4.3.2. The films were deposited with PLD at  $T=650\ ^\circ\text{C}$  and  $p(\text{O}_2)=5\times 10^{-4}$  Torr. The same laser conditions as described in Chapter 4.2.2 were used for the deposition. The BST thin film thickness was controlled to be about 550 nm. After deposition, the films were annealed at  $T=500\ ^\circ\text{C}$  in air for 1 h. The coplanar electrodes were deposited in 2 steps. First, a thin layer of Au/Ti was deposited by evaporation (Oerlikon Leybold Vacuum GmbH, LAB600H, Germany) and patterned by lift-off (Fig. 6.1g). An image reversal photoresist (Microchemicals, AZ1514E, Germany) with a thickness of about  $1.0\ \mu\text{m}$  was used for the lift-off. The AZ1514E photoresist enables the patterning of fine structures in the lower  $\mu\text{m}$ -range by a lift-off process. The layer thicknesses of Au and Ti were 200 and 30 nm, respectively. The Ti layer was

## 6. INTEGRATION OF MICROMACHINED COPLANAR CAPACITORS ON SILICON

---

deposited to improve adhesion of the Au layer on the BST surface. For the thin Au/Ti electrode the gap width was controlled to vary between 1.8 to 2.8  $\mu\text{m}$ . To reduce the loss contribution of the metal electrodes a thicker electrode stack of Au/Ti/Al/Ti was deposited on the thin Au/Ti electrode. The Au/Ti/Al/Ti layer stack was deposited by evaporation and patterned by lift-off (Futurrex Inc, NR7, USA) (Fig. 6.1h). The layer thicknesses of the electrode stack was Au(30 nm)/Ti(30 nm)/Al(1300 nm)/Ti(30 nm).

After deposition, the substrate was removed under the gap of the coplanar devices using the Bosch process as described in Chapter 5.2.1.7. An example of an optical micrograph of a typical coplanar device is shown in Fig. 6.2. The electrode width was varied between 200 to 300  $\mu\text{m}$ .

### 6.2.2 Electrical characterization

The coplanar capacitors were characterized as described in Chapter 5.2.2. The only difference in comparison to the characterization of the BST TFBARs was that G-S (Ground-Signal) probes were used for the measurements (Cascade Microtech, I40-GS-250), USA). The impedance  $Z$  of the capacitors was calculated with Eq. (5.2). The capacitance  $C$  and the loss tangent  $\tan\delta$  of the capacitors can be calculated from the impedance  $Z$ :

$$C = \frac{1}{2f\pi\text{Im}(Z)} \quad (6.1)$$

$$\tan\delta = \frac{\text{Re}(Z)}{\text{Im}(Z)} \quad (6.2)$$

where  $\text{Re}(Z)$ ,  $\text{Im}(Z)$ , and  $f$  are the real and the imaginary part of the measured impedance  $Z$ , and the frequency, respectively. The coplanar BST capacitors were characterized before and after removing the Si under the gap of the devices.

## 6.3 Results and Discussion

The epitaxial nature of the YSZ layer deposited on the Si substrate was studied by Reflection High Energy Electron Diffraction (RHEED). Details about the method are given in Chapter 7.2.2. Figure 6.3a shows the RHEED pattern after YSZ film deposition. The regular spotty pattern shows that the film grew epitaxially on the Si surface. Details about the epitaxial relationships are discussed in Chapter 7.3. After the annealing of the substrate as described in Section 6.2.1, the sample was again analyzed by RHEED. Figure 6.3b shows the RHEED pattern of the YSZ layer after the annealing step. The epitaxial nature of the YSZ layer was not affected by the annealing step. No indication of any degradation of the YSZ film quality could be detected, although the low intensity of the RHEED pattern indicates that the structural quality of the YSZ layer needs further improvement. Figure 6.4 shows the XRD pattern of the sample after BST thin film

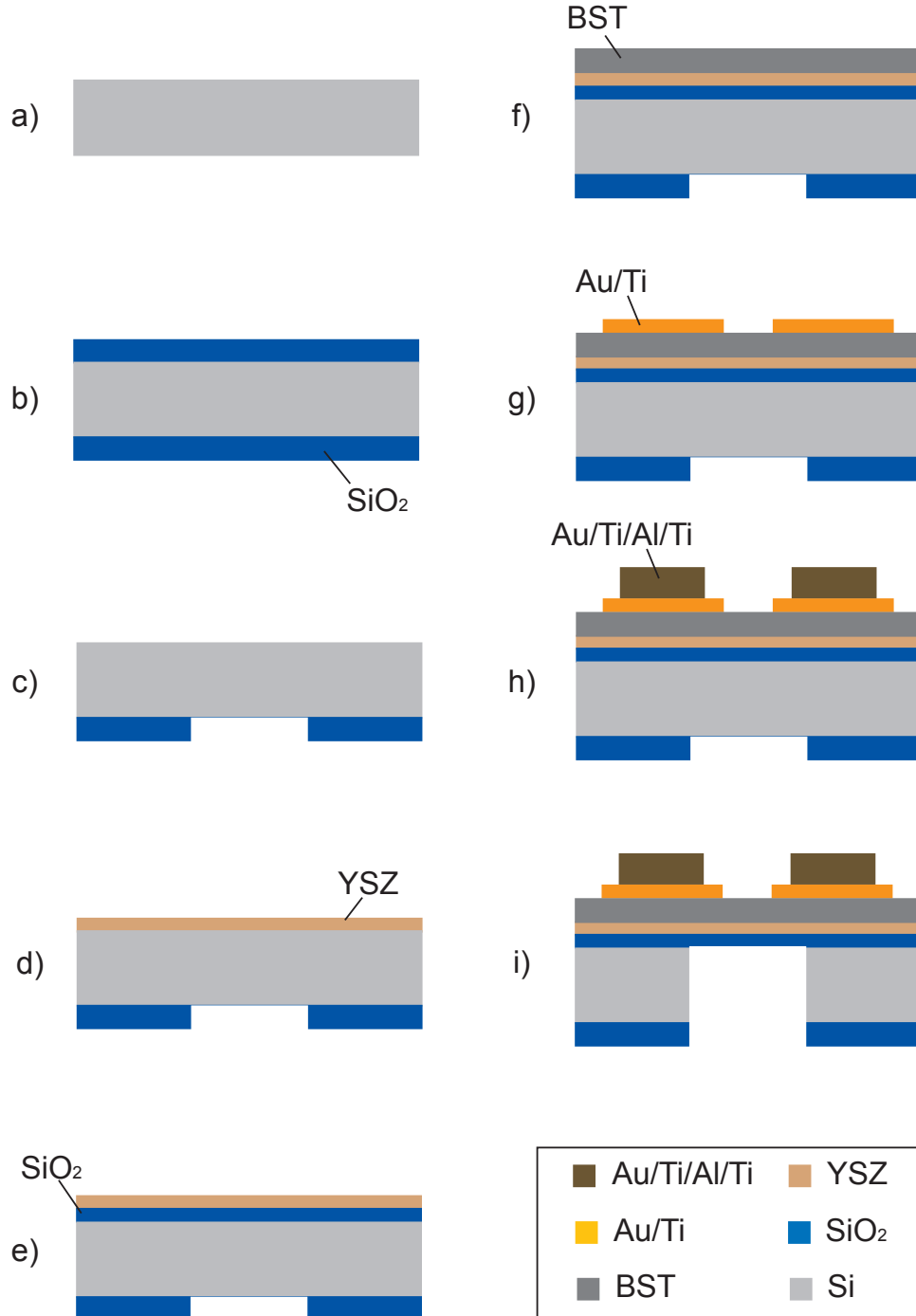


Figure 6.1: Process flow for the fabrication of the micromachined coplanar BST capacitor.

## 6. INTEGRATION OF MICROMACHINED COPLANAR CAPACITORS ON SILICON

---

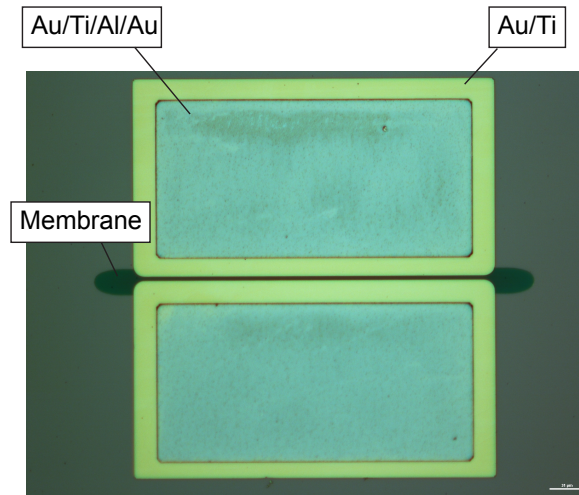
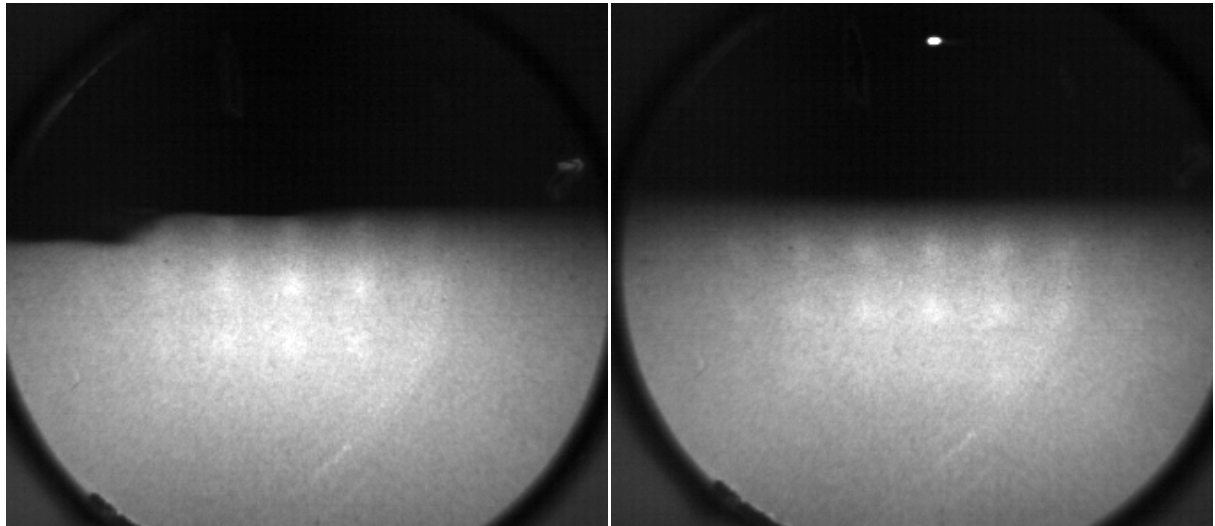


Figure 6.2: Example of an optical micrograph of a micromachined coplanar BST capacitor. The electrode gap of the capacitor is centered on the membrane.



(a) YSZ before annealing

(b) YSZ after annealing

Figure 6.3: RHEED pattern of the YSZ layer after film deposition (a) and after annealing the sample at  $T=1000$  °C for 5h in flowing O<sub>2</sub> (b).

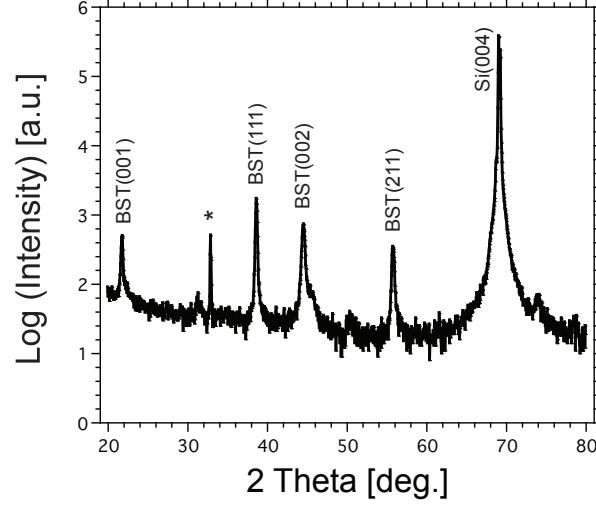


Figure 6.4: XRD pattern of the annealed YSZ/Si substrate after BST thin film deposition. The peak marked by the asterisk is the Si(002) peak of the Si substrate.

deposition. All the observed peaks could be attributed to crystalline phases. Only peaks of the BST thin film and the Si substrate were observed. Peaks of the YSZ layer were not detectable, which can be explained by the small thickness of the YSZ layer. The BST thin film showed peaks of the (001), (111), (002) and (211) family of lattice planes and is therefore polycrystalline. The (110) peak, which is normally the strongest peak in a randomly oriented bulk sample (see JCPDS file: 39-1395), was completely absent. This indicates that the BST thin film shows some kind of preferred orientation.

Figure 6.5 compares the frequency dependence of the capacitance of the micromachined and the non-micromachined BST capacitor. The data is shown for zero dc bias and at a dc electric field of 1100 kV/cm which corresponded to the maximum applied voltage. Both capacitors had the same dimensions. The gap width and the electrode width were 1.8  $\mu\text{m}$  and 300  $\mu\text{m}$ , respectively. For both devices a reduction of the capacitance with increasing dc bias was observed. The micromachined coplanar capacitor showed a weak frequency dependence of the capacitance. The capacitance decreased slightly with increasing frequency as also observed by Baniecki et al. [186]. The slightly higher capacitance of the device at low frequencies could also be due to some parasitic contributions from the substrate as discussed below. At high dc electric fields an acoustic resonance appeared at around 5 GHz. Unfortunately, the acoustic resonance could not be excited at lower dc electric fields. The reason for this is probably due to the device design. Apparently, the thickness to gap ratio of the device is not appropriate so that the energy of the acoustic wave is scattered away from the active area of the device. A reduction of the thickness and/or an increase of the gap width could help to improve the confinement of

## 6. INTEGRATION OF MICROMACHINED COPLANAR CAPACITORS ON SILICON

---

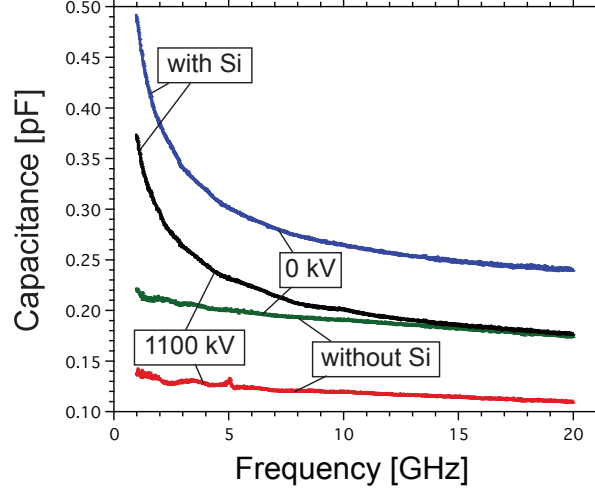


Figure 6.5: Comparison of the frequency dependence of the capacitance of a micromachined and a non-micromachined coplanar BST capacitor under zero and 1100 kV/cm dc electric field.

the energy of the wave in the active area. Detailed modeling of the structure would be necessary to draw more precise conclusions. Because of these reasons we could not study the effect of tuning of the acoustic resonances in the LFE mode as theoretically addressed in Chapter 3.

The capacitance of the non-micromachined coplanar capacitor was higher than the capacitance of the micromachined one, although all other device characteristics as well as the BST thin film properties were the same. The results can be explained by a contribution from the substrate to the capacitance of the device. Due the device design of the coplanar capacitor, the capacitances stemming from the different layers in the active area of the device are connected in parallel. Thus, these capacitances sum up. The capacitance of the micromachined  $C_{mm}$  and the non-micromachined  $C_{nmm}$  capacitors are given by:

$$C_{mm} = C_{BST} + C_{SiO_2} \quad (6.3)$$

$$C_{nmm} = C_{BST} + C_{SiO_2} + C_{Si} \quad (6.4)$$

where  $C_{BST}$ ,  $C_{SiO_2}$ , and  $C_{Si}$  are the contributions from the BST, the  $SiO_2$  and the Si substrate to the capacitance of the device. Here, we neglected the contribution from the YSZ layer. By applying a dc bias only  $C_{BST}$  is tuned. The tunability of the micromachined  $n_{mm}$  and the non-micromachined capacitor  $n_{nmm}$  can be described as:

$$n_{mm} = \frac{\Delta C_{BST}}{C_{mm}} \quad (6.5)$$



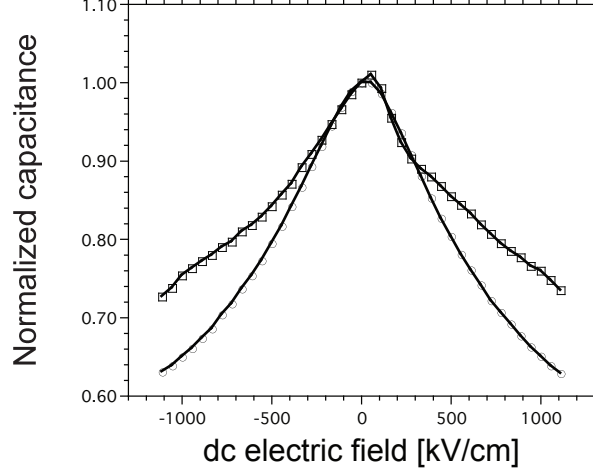


Figure 6.6: Comparison of the dc electric field dependence of the normalized capacitance of a micromachined (open circles) and non-micromachined (open squares) coplanar BST capacitor. The data was measured at 20 GHz.

$$n_{nm} = \frac{\Delta C_{BST}}{C_{nm}} \quad (6.6)$$

Since  $C_{mm} < C_{nm}$ ,  $n_{mm} > n_{nm}$ . That this is the case can be seen from Fig. 6.6. It shows the dependence of the normalized capacitance of the micromachined and non-micromachined capacitor on the applied dc electric field. As mentioned above, the micromachined capacitor clearly showed a stronger tuning than the non-micromachined capacitor. The tunability of the micromachined capacitor and the non-micromachined capacitor was 37% and 26%, respectively, for  $E_{dc}=1100$  kV/cm and a measurement frequency of 20 GHz.

The capacitance of the non-micromachined capacitor showed a strong increase at lower frequencies ( $f \leq 5$ GHz). This was also observed by Lan et al. for coplanar Ba(Zr<sub>0.25</sub>,Ti<sub>0.75</sub>)O<sub>3</sub> capacitors on high-resistive Si [187].

This observation might be explained by two effects. First, an increase in the permittivity of the Si substrate due to an increase of the complex conductivity of the substrate with decreasing frequency. Second, the presence of a conductive interfacial layer at the SiO<sub>2</sub>/Si interface leading to a reduced effective resistivity of the Si substrate.

Under an ac field the conductivity  $\sigma_{Si}$  of Si shows some dispersion and can be described as a complex quantity:

$$\sigma_{Si} = \sigma' + i\sigma'' \quad (6.7)$$

where  $\sigma'$  and  $\sigma''$  correspond to the real and imaginary parts of the conductivity. The

## 6. INTEGRATION OF MICROMACHINED COPLANAR CAPACITORS ON SILICON

---

complex conductivity adds to the permittivity of the intrinsic Si  $\varepsilon_{int}$  [188; 189]:

$$\varepsilon = \varepsilon_{int} + \frac{i\sigma_{Si}}{\omega\varepsilon_0} \quad (6.8)$$

where  $\omega$  and  $\varepsilon_0$  are the angular frequency and the vacuum permittivity, respectively. The contribution of the complex conductivity to the permittivity of intrinsic Si leads to a frequency dependence of the Si permittivity. The permittivity increases at lower frequencies, which results in an increase in the capacitance contributing to the capacitance of the device.

The other effect that might contribute to the strong increase in the capacitance of the device at low frequencies can be attributed to a conductive layer at the interface between SiO<sub>2</sub>/Si. It has been observed that the oxidation of a Si substrate leads to a layer of reduced resistivity (or increased conductivity) at the interface between the Si and the SiO<sub>2</sub> layer [190; 191]. The phenomenon is explained by positive oxygen charge carriers in the SiO<sub>2</sub> which lead to an attraction of negative charge carriers at the SiO<sub>2</sub>/Si interface [191]. The charge carriers at the interface increase the conductivity in that region, which can result in a reduction of the effective resistivity of the Si substrate [190]. Thus, the impact of the complex conductivity of the Si substrate on the frequency dependence of the non-micromachined capacitor becomes even more pronounced. In the micromachined capacitor this effect is not observed or, at least, is weakened since the substrate, and therefore also the SiO<sub>2</sub>/Si interface, was removed under the active area of the device. Nevertheless, a small contribution of the conductivity contribution is still possible through some conduction effect around the membrane of the device.

Figure 6.7 compares the loss tangent of the micromachined and the non-micromachined capacitor. The data shown was not de-embedded which complicates the discussion. The loss tangent of the micromachined capacitor increased slightly with frequency. Under dc bias, the loss tangent decreased, which can be explained by the reduced permittivity of the BST thin film [10]. At low frequencies the loss tangent showed an increase under dc bias. This increase can be explained by a contribution of dc leakage currents in the Si substrate at low frequencies to the loss tangent of the device. The observed effect was much weaker than for the non-micromachined capacitor, as discussed below, due to removing of the substrate from the active area of the device. The loss tangent of the non-micromachined capacitor was in general higher than the loss tangent of the micromachined capacitor. The increase in the loss tangent was due to a loss contribution of the Si substrate. As observed for the capacitance, the loss tangent increases with decreasing frequency due to the reasons mentioned above. Under dc bias the loss tangent of the non-micromachined capacitor increased. Again, this observation can be explained by a contribution of dc leakage currents in the Si substrate to the loss tangent of the device [190].

Figure 6.8 shows the capacitance and the loss tangent of the micromachined capacitor at 20 GHz. The device showed a relative tunability of 37% at a dc electric field of 1100 kV/cm. The loss tangent at zero dc bias was around 0.08 and decreased to about

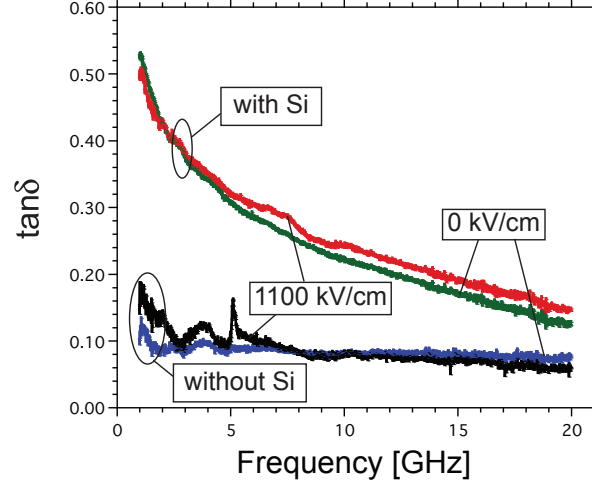


Figure 6.7: Comparison of the frequency dependence of the loss tangent of a micromachined and a non-micromachined coplanar BST capacitor at a dc electric field of 0 kV/cm and 1100 kV/cm, respectively.

0.06 under bias. The decrease in the loss tangent with increasing dc bias can be attributed to the reduction of the permittivity of the BST thin film under dc bias.

Calculation of the permittivity of the BST thin film from the capacitance of a coplanar capacitor is more complicated than for the parallel-plate capacitor. The complications are due to the electric field distribution between the ferroelectric layer, substrate, and air that has to be taken into account. The capacitance of the coplanar capacitor can be modeled with conformal mapping techniques. It can be calculated with the formula derived by Vendik et al. [192]:

$$C = \varepsilon_0 w \left[ \frac{2}{\pi} \ln \left( \frac{4l}{s} \right) + \frac{\varepsilon_3 - 1}{\pi} \ln \left( 16 \frac{t_3 + t_2}{\pi s} \right) + \frac{\varepsilon_2 - \varepsilon_3}{\frac{s}{h_2} + \frac{4}{\pi} \ln 2} \right] \quad (6.9)$$

where  $\varepsilon_0$ ,  $\varepsilon_2$ , and  $\varepsilon_3$  are the permittivity of vacuum, the ferroelectric film, and the substrate, respectively.  $t_2$  and  $t_3$  are the thickness of the ferroelectric film and the substrate, respectively, and  $w$ ,  $l$ , and  $s$  are the capacitor width, capacitor length, and the gap width, respectively. The permittivity of the BST thin film in the micromachined capacitor was calculated with Eq. (6.9) by solving it for the film permittivity  $\varepsilon_2$  and using the relevant dimensions and material properties of our device. The zero-bias permittivity of the BST layer was calculated to be 270 at room temperature. This is a rather low value considering the Ba-rich composition of our thin film as well as the rather large film thickness of 550 nm. We assume that the low permittivity is due to the bad crystalline quality of

## 6. INTEGRATION OF MICROMACHINED COPLANAR CAPACITORS ON SILICON

---

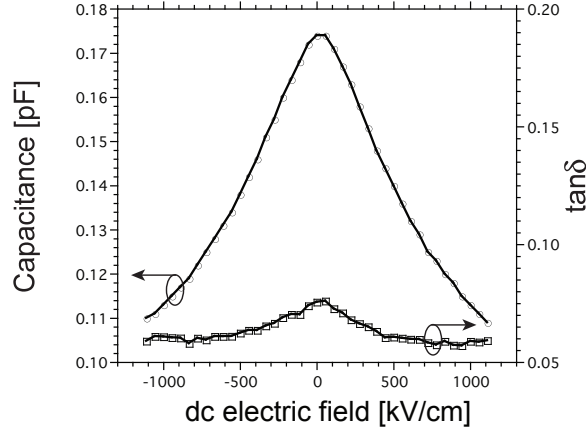


Figure 6.8: Electric field dependence of the capacitance and the loss tangent of the micromachined coplanar capacitor. The data shown was measured at 20 GHz.

our thin film, although it was deposited on an epitaxial YSZ seeding layer. As we demonstrated in Chapter 4.3.2, a BST thin film with the same composition, similar thickness, and deposited at  $T=600$  °C under the same  $p(O_2)$  on Pt showed a zero-bias permittivity of 390 at room temperature. This corresponds to an increase of almost 50%. For the moment we can not explain the low permittivity of the BST thin in the coplanar capacitor, but optimization of the growth conditions should be considered to improve the BST thin film quality. An improvement in the BST thin film quality would result in an increase in the permittivity and therefore also in the tunability of the micromachined coplanar capacitor.

### 6.4 Summary and Conclusions

In this chapter we reported on the fabrication and electrical characterization of coplanar BST thin film capacitors on Si. We introduced our concept of using micromachining technologies to reduce the effect of parasitic contributions from the substrate. We proved the feasibility of the approach by comparing the performance of a micromachined capacitor with a non-micromachined capacitor. For the same device dimensions, the micromachined capacitor exhibited a lower capacitance but higher tunability. The loss tangent of the micromachined capacitor was lower than the loss tangent of the non-micromachined one. The results can be explained by a reduction of the impact of parasitics from the Si substrate contributing to the properties of the device. This reduction was achieved by

removing the Si substrate from the active area of the device. The micromachined capacitor had a tunability of 37% at  $E_{dc}=1100$  kV/cm. The loss tangent at 20 GHz was 0.08 and 0.06 at zero and maximum dc bias, respectively. The results on the loss tangent were not de-embedded. The zero bias permittivity of the BST( $x=0.7$ ) thin film was 270 at room temperature. This low permittivity value resulted in a rather low value of the tunability. Improvements of the BST thin film quality should be considered to improve the properties of the BST thin film and thus, the performance of the device. The non-micromachined capacitor showed an appreciable increase in the capacitance and loss tangent at frequencies below 5 GHz. This phenomenon can be explained by a frequency dependent complex conductivity of the Si substrate which contributed to the capacitance of the device. Under dc bias the loss tangent of the non-micromachined capacitor increased, which is explained by a contribution of dc leakage currents to the loss tangent of the device.



# Chapter 7

## Integration of epitaxial BST thin films on silicon

In this chapter we present our study on the integration of epitaxial BST thin films on Si. Epitaxial BST thin films are of interest due to the possibility of enhancing the performance of tunable devices.

### 7.1 Introduction

Although epitaxial BST thin film growth has been demonstrated on a wide variety of lattice matched single-crystal substrates [57; 58; 59; 62], the integration of epitaxial BST thin films on Si is of great interest. Beside economic reasons, like low cost and industrial scale-up, the interest is also due to the potential to increase the functionality of devices by combining the properties of semiconductor and oxide materials.

For tunable applications, epitaxial BST thin films have the potential to outperform polycrystalline ones. The reasons are an enhanced tunability [193; 194] with potentially very low dielectric losses as observed for BST single crystals [12]. A drawback of epitaxial BST thin films against their polycrystalline counterparts is the large temperature dependence of the permittivity.

Epitaxial BST thin films are also of interest for tunable TFBARs for several reasons. Due to their enhanced tunability, an increase in the dc bias dependent electromechanical coupling factor  $k_{BST}^2$  of the BST layer is expected. Since  $k_{BST}^2$  controls the tuning of the resonance frequency, this would lead to an enhancement of the tuning range of the TFBAR as discussed in Chapter 3.

The better alignment of epitaxial BST thin films in the out-of-plane direction could also improve the performance of the tunable TFBARs for two reasons. First, since the sound velocity of the BST layer varies significantly with the crystal orientation as outlined in Chapter 5.3.2, one can expect that epitaxial thin films have a lower dispersion of the

## 7. INTEGRATION OF EPITAXIAL BST THIN FILMS ON SILICON

---

sound velocity of the acoustic wave. This could potentially lead to an improvement in the Q-factor of the device. Second, an enhancement of  $k_{BST}^2$  can be expected due to the better alignment of the crystals in the direction of the traveling acoustic wave. This has been demonstrated for AlN based resonators by Bjurström et al. [195]. They found that a better c-axis alignment of the AlN layer resulted in an increased electromechanical coupling factor for the device.

In this chapter we demonstrate the integration of epitaxial BST thin films on Si. The integration is achieved by using two different electrode / buffer layer structures, namely YBCO / CeO<sub>2</sub> / YSZ and TiN. The epitaxial relationship and the structural quality of the heterostructures are investigated. For the growth of epitaxial BST on TiN-buffered Si, the appropriate T-p(O<sub>2</sub>) conditions have been established.

### 7.2 Experimental details

In this section we report on the processing of epitaxial BST thin films on Si substrates as well as the methods used to characterize the multilayer structures.

#### 7.2.1 Processing of BST thin films and electrode/buffer layers

In this section we will give details about the growth conditions and other issues related to the integration of epitaxial BST thin films on Si substrates. We used Si(001) test wafers as substrates. Two different electrode / buffer layer systems were investigated.

##### 7.2.1.1 BST/YBCO/CeO<sub>2</sub>/YSZ/Si system

For this structure, no special preparation of the substrate, like removal of the native oxide layer on the Si surface, was needed. The Si substrate was only cleaned in isopropanol using ultrasound agitation. The deposition of the YSZ layer was performed at T=800 °C and at p(O<sub>2</sub>) ≤ 10<sup>-6</sup> Torr. Under these conditions, the native oxide on the Si surface is reduced and the YSZ layer can grow epitaxially [196]. Epitaxial YSZ growth has also been achieved by removing the native oxide on the Si wafer [197], but this typically involves the use of an hydrofluoric acid (HF) solution for etching the native oxide. During the growth of the YSZ layer, we observed the deposition of particulates which often occurs during the PLD process. To reduce the number of particulates we reduced the thickness of the YSZ layer down to about 5 nm, which reduced the probability of particulate deposition. Other methods like changing the laser conditions, polishing the target surface or using a shadow mask failed to significantly reduce the number of particulates.

The CeO<sub>2</sub> and the YBCO layer were grown at T=800 °C and p(O<sub>2</sub>) = 5×10<sup>-4</sup> Torr and T=730 °C and p(O<sub>2</sub>)=50 mTorr, respectively. During the growth of the YBCO layer we also observed the deposition of particulates like many others [198; 199]. Since the YBCO



layer should potentially be used as a bottom electrode, a reduction in the layer thickness as demonstrated for the YSZ layer was not possible. To reduce the number of particulates significantly the so-called off-axis geometry for the PLD process was used [200]. Here, the substrate was turned by  $90^\circ$  so that it was placed in the direction of the expanding plasma plume. The atoms, ions, and molecules of the ablated material are scattered by the  $O_2$  atoms of the background gas (high pressure!) and directed to the substrate surface where they are deposited. The large and heavy particulates are not affected by the background pressure and thus, are not deposited on the substrate surface.

The BST layer of  $x=0.3$  composition was deposited at  $T=750^\circ\text{C}$  and  $p(O_2)=50\text{ mTorr}$ . For all layers of the structure, the laser energy was set to 220 mJ, which resulted in an estimated energy density of about  $10\text{ J/cm}^2$ . The target to substrate distance was about 5 cm. The laser repetition rate was set to 5, 7, 7, and 7 Hz for the BST, YBCO,  $CeO_2$ , and YSZ layer, respectively.

### 7.2.1.2 BST/TiN/Si system

Prior to the deposition of the TiN layer, the native oxide on the Si substrate was removed by dipping the substrate into a 5% HF-solution for about 30 s. The TiN layer was deposited under Ultra High Vacuum (UHV) conditions at  $p(O_2) \leq 10^{-7}\text{ Torr}$ . The deposition temperature was varied from 700 to  $900^\circ\text{C}$  to study the effect of the growth temperature on the quality of the TiN layer.

The BST( $x=0.3$ ) thin films were deposited on the optimized TiN layer (grown at  $T=850^\circ\text{C}$  and  $p(O_2) \leq 10^{-7}\text{ Torr}$ ). The films were grown under wide temperature and  $p(O_2)$  conditions to find the optimum parameters for the epitaxial BST thin film growth.

The laser energy for the TiN and BST deposition was set to 220 mJ, which resulted in an estimated energy density of about  $10\text{ J/cm}^2$ . The target to substrate distance was about 5 cm. The laser repetition rate was set to 5 and 3 Hz for the BST and the TiN layer, respectively.

## 7.2.2 Structural characterization

The structural quality and the epitaxial relationship of the films were studied by various methods.

### X-ray diffraction analysis

The out-of-plane orientation of the multilayer structures was studied by XRD using the Bragg-Brentano geometry as outlined in Chapter 4. The structural quality of the different thin films was estimated by measuring rocking curves (so-called  $\omega$ -scans). The smaller the Full Width at Half Maximum (FWHM) of the rocking curve, the lower the degree of misalignment of the different grains of the films and thus, the better the structural quality

## 7. INTEGRATION OF EPITAXIAL BST THIN FILMS ON SILICON

---

of the films. The in-plane orientation of the thin films was studied by measuring  $\phi$ -scans using a 4-circle x-ray diffractometer (Seifert, ID3003, Netherlands).

### Reflection High Energy Electron Diffraction

Reflection High Energy Electron Diffraction (RHEED) was used to study the in-plane orientation of the thin films in-situ meaning during or after the film deposition without breaking the vacuum. Beside the determination of the in-plane orientation of the thin films, the method enables an estimation of the surface quality (mainly roughness) and can monitor the film growth in the sub-monolayer regime (RHEED oscillations).

In RHEED a high energy electron beam (35 keV for our setup) is directed on the sample at a grazing angle of about  $2^\circ$  or less. The electrons of the beam only penetrate the surface of the sample, where they are diffracted. The diffracted electrons are detected on a phosphor screen. The diffraction pattern detected on the phosphor screen is related to the reciprocal unit cell of the film. For a high quality epitaxial film with a low surface roughness each point in the reciprocal lattice is shown as a streak in the diffraction pattern. If the structural quality of the sample is less perfect and the film is rougher, each point in the reciprocal lattice is shown as a spot in the diffraction pattern.

### Transmission and Scanning Electron Microscopy

Transmission Electron Microscopy (TEM) was used to investigate the microstructure of cross-sections of the multilayer structures. Scanning Electron Microscopy (SEM) was used to investigate the microstructure of the films.

## 7.3 Results and Discussion

### BST/YBCO/CeO<sub>2</sub>/YSZ/Si system

Figure 7.1 shows a XRD  $\theta - 2\theta$ -scan of the BST / YBCO / CeO<sub>2</sub> / YSZ / Si multilayer structure. All peaks of the diffraction pattern could be attributed to crystalline phases. Peaks of the YSZ layer could not be detected because of the small thickness of the film. Only peaks of the (00l) family of lattice planes were observed for the different phases forming the structure. This indicates that all the layers of the structure were c-axis oriented in the out-of-plane direction (normal to the substrate).

Figure 7.2 shows RHEED patterns of all the phases of the multilayer structure. The RHEED patterns shown are for the incident electron beam of the RHEED gun being parallel to the Si[100] direction. Patterns taken along the Si[110] direction were also recorded, but are not shown here. For all phases a regular and periodical diffraction pattern was observed indicating a single in-plane orientation with respect to the other layers. The YSZ layer exhibited a diffraction pattern of weak intensity indicating that the

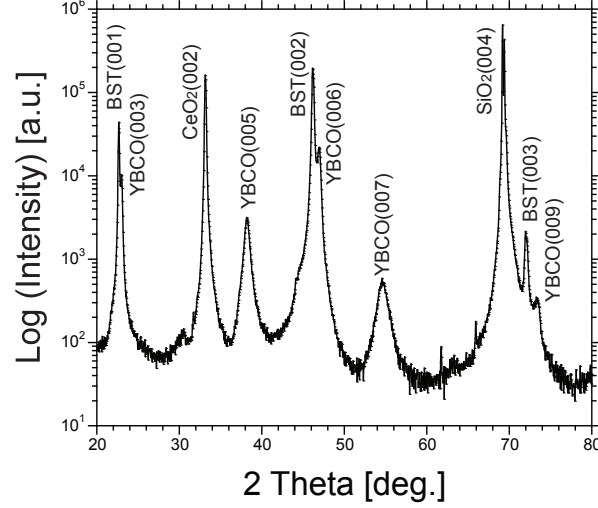


Figure 7.1: XRD  $\theta - 2\theta$ -scan of the BST / YBCO / CeO<sub>2</sub> / YSZ / Si multilayer structure. For the phases forming the structure only peaks of the (00l) family of lattice planes could be detected.

structural quality of the layer was rather poor. For the CeO<sub>2</sub> and the YBCO layer rather streaky RHEED patterns were observed, which means that the films had a rather low surface roughness. The BST thin film showed a rather spotty pattern meaning that the surface of the thin film was rougher than in the case of the CeO<sub>2</sub> and the YBCO layer.

In Fig. 7.3 XRD  $\phi$ -scans around Si(hhh) (Fig. 7.3a) and Si(hh0) (Fig. 7.3b) are shown. The in-plane orientation of the CeO<sub>2</sub> could not be detected with  $\phi$ -scans around Si(hh0) due to some peak overlapping. Therefore, additional scans around Si(hhh) were performed. The position of the diffraction peaks of the CeO<sub>2</sub> and the Si substrate coincided as shown in Fig. 7.3a. This indicates that the CeO<sub>2</sub> layer had the same in-plane orientation than the Si substrate.

The diffraction peaks of the  $\phi$ -scans of the YBCO and the BST layer are shifted by 45° with respect to the ones from the Si substrate as illustrated in Fig. 7.3b. This means that the unit cells of the YBCO and the BST layer are rotated in-plane by 45° with respect to the Si substrate.

The results shown above illustrate that all the layers forming the structure were grown epitaxially on the Si substrate. The in-plane and out-of-plane epitaxial relationship as found by means of XRD and RHEED analysis were:

- BST[110]||YBCO[110]||CeO<sub>2</sub>[100]||YSZ[100]||Si[100]
- BST(001)||YBCO(001)||CeO<sub>2</sub>(001)||YSZ(001)||Si(001)

## 7. INTEGRATION OF EPITAXIAL BST THIN FILMS ON SILICON

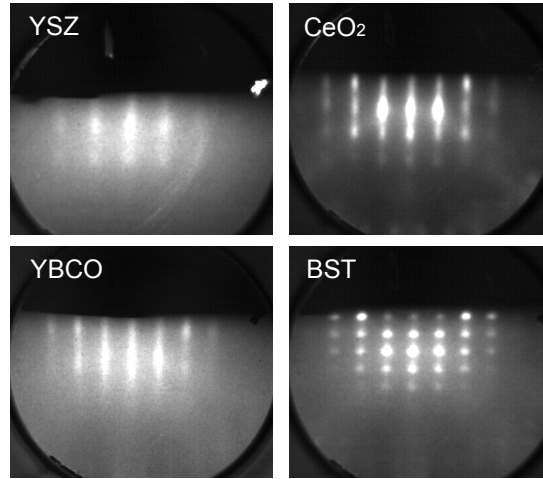


Figure 7.2: RHEED diffraction patterns of the different layers of the BST / YBCO / CeO<sub>2</sub> / YSZ / Si structure. The incident electron beam was parallel to Si[100].

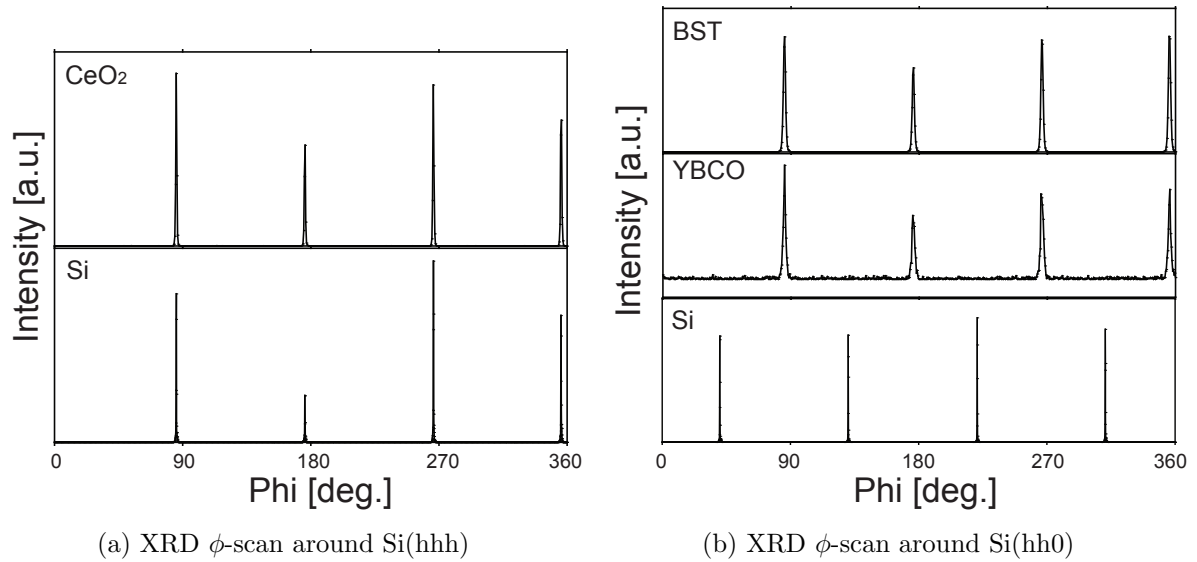


Figure 7.3: XRD  $\phi$ -scans taking around Si(hhh) (a) and Si(hh0) (b).

### 7.3 Results and Discussion

Table 7.1: Summary of growth conditions, epitaxial relationships, and film quality of the BST / YBCO / CeO<sub>2</sub> / YSZ and BST / TiN heterostructures deposited on Si substrates. The rocking curve of the YSZ film could not be measured due to too low intensity of the diffraction peak.

	BST/YBCO/CeO <sub>2</sub> /YSZ/Si	BST/TiN/Si
<b>Conditions</b>		
Temperature [°C]	750/730/800/800	max. 600/850
p(O <sub>2</sub> ) [Torr]	0.05/0.05/5 × 10 <sup>-4</sup> /≤ 10 <sup>-7</sup>	max. 5 × 10 <sup>-4</sup> /≤ 10 <sup>-7</sup>
<b>Epitaxy</b>		
Out-of-plane	(001)   (001)   (001)   (001)   (001)	(001)   (001)   (001)
In-plane	[110]   [110]   [100]   [100]   [100]	[100]   [100]   [100]
<b>Film quality</b>		
Rocking curve FWHM [deg.]	0.5/0.4/0.5/ - / -	2.2/1.0/ -

The structural quality of the different films of the multilayer structure was tested by measuring the FWHM of rocking curves. For the BST, YBCO, and CeO<sub>2</sub> layers the FWHM of the corresponding rocking curves were 0.5°, 0.4°, and 0.5°, respectively. This indicates a very good structural quality of the multilayer structure. The results for the BST / YBCO / CeO<sub>2</sub> / YSZ / Si structure are summarized in Tab. 7.1.

#### BST/TiN/Si system

For the integration of epitaxial BST on TiN-buffered Si we concentrated first on the optimization of the structural quality of the TiN layer. A high quality of the buffer layer is an important requirement for the growth of a high quality BST thin film on the Si substrate.

For the optimization of the TiN layer the deposition temperature of the layer was varied from 700 to 900 °C. The depositions were done under UHV conditions at pressures  $p \leq 10^{-7}$  Torr. Under all these conditions, the TiN layers were grown epitaxially on Si. The structural quality of the TiN layers was tested by comparing the FWHM of the rocking curves of the TiN(002) diffraction peak.

Figure 7.4 shows the dependence of the FWHM of the rocking curve of the TiN(002) diffraction peak on the deposition temperature. It can clearly be seen that an increase in the deposition temperature resulted in an improvement of the structural quality of the TiN film as indicated by the decrease in the FWHM of the rocking curve. The FWHM of the rocking curve for a film deposited at T=900 °C was 0.7°, whereas at T=700 °C the FWHM of the peak was 2.5°.

The improvement of the structural quality of the TiN thin film with increasing deposition temperature was also observed by comparing the relevant RHEED patterns. For

## 7. INTEGRATION OF EPITAXIAL BST THIN FILMS ON SILICON

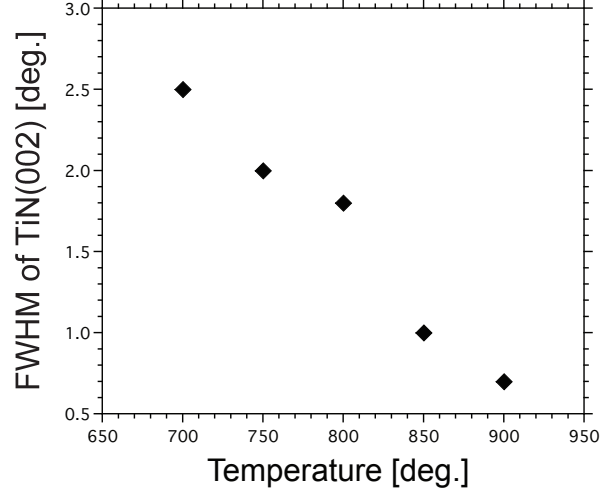


Figure 7.4: Dependence of the FWHM of the rocking curve of the TiN(002) diffraction peak on the deposition temperature of the TiN thin film. The FWHM decreased from 2.5° at a deposition temperature of 700 °C to 0.7° at a deposition temperature of 900 °C.

higher deposition temperatures the RHEED patterns became sharper with the diffraction spots being more intense. Fig. 7.5 compares the RHEED patterns of TiN films grown at 700 and 900 °C, where the improvement in the film quality can clearly be seen.

As mentioned above, all the TiN films were deposited under UHV conditions. The use of a N<sub>2</sub> background gas pressure was tested with the motivation to improve the TiN film quality further. Under N<sub>2</sub> gas pressure the TiN films grew polycrystalline with occasional secondary phases. Thus, the deposition of TiN under UHV conditions yielded the best structural quality of the films.

After the optimization of the TiN film quality we investigated the epitaxial growth of BST on the epitaxial TiN layer. Here, the possible oxidation of the TiN layer is of great concern since this would destroy the good lattice matching between the BST and the TiN layer. The BST thin films were deposited in a wide temperature (500 to 800 °C) and pressure range ( $p \leq 10^{-7}$  to 0.050 Torr). The TiN buffer layer was deposited at T=850 °C under UHV conditions. We chose this lower deposition temperature because of some limitations of our PLD system while still achieving a high quality TiN layer. Under these deposition conditions the FWHM of the rocking curve of the TiN(002) peak was 1° as illustrated in Fig. 7.4.

Figure 7.6 shows XRD  $\theta-2\theta$ -scans of the BST thin films deposited in UHV ( $p \leq 10^{-7}$  Torr) at 600 °C (b), 700 °C (c), and 800 °C (d). A XRD  $\theta-2\theta$ -scan of a BST film deposited at  $p(\text{O}_2) = 5 \times 10^{-4}$  Torr and T=600 °C is also shown (a). The corresponding RHEED patterns of the BST thin films deposited under the different conditions are shown in Fig. 7.7.

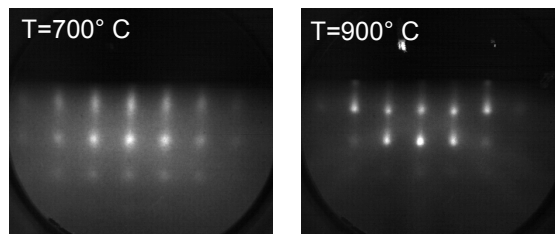


Figure 7.5: RHEED diffraction patterns of the TiN layers deposited at  $T=700\text{ }^{\circ}\text{C}$  and  $T=900\text{ }^{\circ}\text{C}$ . The incident electron beam was parallel to Si[100]. With increasing deposition temperature the RHEED patterns became sharper with more intense diffraction spots indicating an improvement in the structural quality.

The BST films deposited at  $600\text{ }^{\circ}\text{C}$  and  $700\text{ }^{\circ}\text{C}$  showed only peaks of the (00l) family of lattice planes for the BST and the TiN layer. Thus, the BST thin films grown under these conditions are c-axis oriented in the out-of-plane direction (normal to the substrate). For the BST thin film deposited at  $T=800\text{ }^{\circ}\text{C}$  under UHV, a small BST(110) peak was observed indicating that the film is not perfectly c-axis oriented in the out-of-plane direction, but still highly (00l) textured.

The corresponding RHEED images for the BST films are shown in Fig. 7.7. For the BST films deposited at  $T=600\text{ }^{\circ}\text{C}$  under UHV and  $p(\text{O}_2) = 5 \times 10^{-4}$  Torr, shown in (a) and (b), respectively, RHEED diffraction was observed. The regular diffraction pattern indicates that the films have a single in-plane orientation. Thus, the films grew epitaxially.

For the BST thin films deposited at  $700\text{ }^{\circ}\text{C}$  and  $800\text{ }^{\circ}\text{C}$  under UHV conditions, no RHEED diffraction was observed. Thus, the films do not have a single, but a random in-plane orientation with respect to the Si substrate. Therefore, we conclude that these films have highly c-axis orientated grains which are arbitrarily rotated in the in-plane dimension. Thus, the films are not of true epitaxial nature, but are polycrystalline.

Figure 7.8 shows the dependence of the crystalline nature of the BST thin films deposited on TiN-buffered Si on the deposition temperature and pressure. True epitaxial BST thin film growth was only observed in a narrow temperature range from  $550\text{ }^{\circ}\text{C}$  to  $600\text{ }^{\circ}\text{C}$  and for  $p(\text{O}_2) \leq 5 \times 10^{-4}$  Torr. Under all other conditions the BST thin film growth was polycrystalline.

To find out why the epitaxial growth of BST thin films on TiN-buffered Si occurred only in such narrow T-p( $\text{O}_2$ ) conditions, we investigated epitaxial and polycrystalline BST thin films by SEM and TEM.

Figure 7.9 shows SEM images of the surfaces of an epitaxial (Fig. 7.9a) and a polycrystalline (Fig. 7.9b) BST thin film. The epitaxial BST thin film was deposited at  $T=600\text{ }^{\circ}\text{C}$

## 7. INTEGRATION OF EPITAXIAL BST THIN FILMS ON SILICON

---

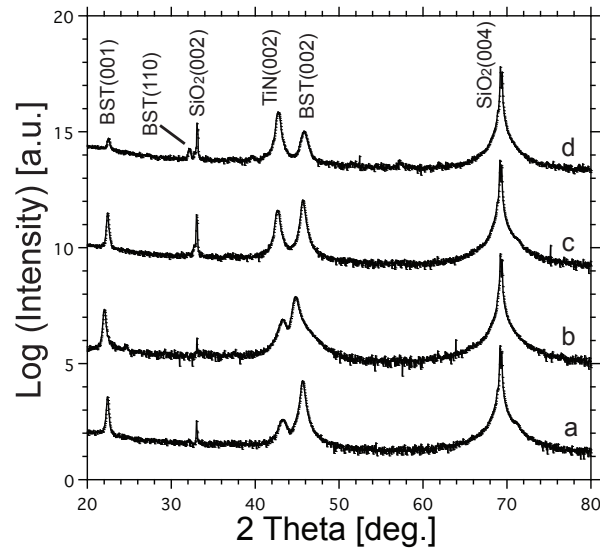


Figure 7.6: XRD  $\theta - 2\theta$ -scans of BST thin films deposited under different temperature and pressure conditions. The diffraction pattern of the BST thin film deposited at  $p=5 \times 10^{-4}$  Torr and  $T=600$  °C is labeled as (a). The diffraction patterns of the BST thin films deposited at  $p \leq 10^{-7}$  Torr and at 600 °C, 700 °C, and 800 °C are labeled as (b), (c), and (d), respectively.



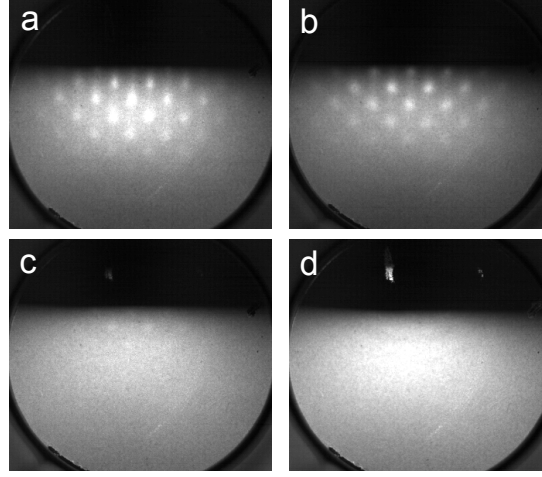


Figure 7.7: RHEED diffraction patterns for BST thin films deposited under different temperature and pressure conditions. The diffraction pattern of the BST thin film deposited at  $p=5 \times 10^{-4}$  Torr and  $T=600$  °C is labeled as (a). The diffraction patterns of the BST thin films deposited at  $p \leq 10^{-7}$  Torr and at 600 °C, 700 °C, and 800 °C are labeled as (b), (c), and (d), respectively. The labels are identical to Fig. 7.6 to allow direct comparison of the data.

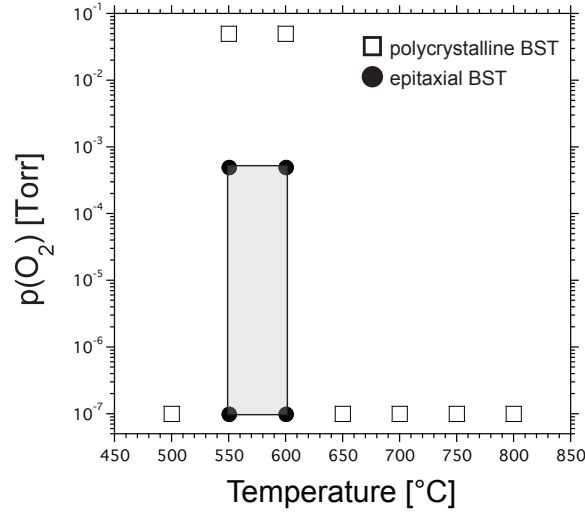


Figure 7.8: Dependence of the crystalline nature of the BST thin films deposited on TiN-buffered Si on the deposition temperature and pressure. Epitaxial BST thin film growth was only observed in a narrow temperature and pressure window.

## 7. INTEGRATION OF EPITAXIAL BST THIN FILMS ON SILICON

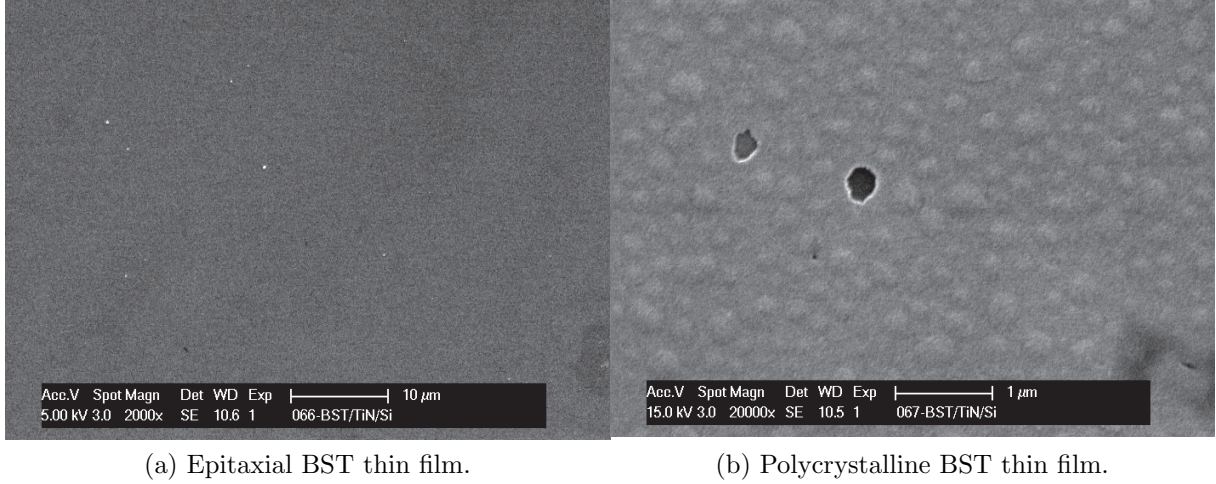


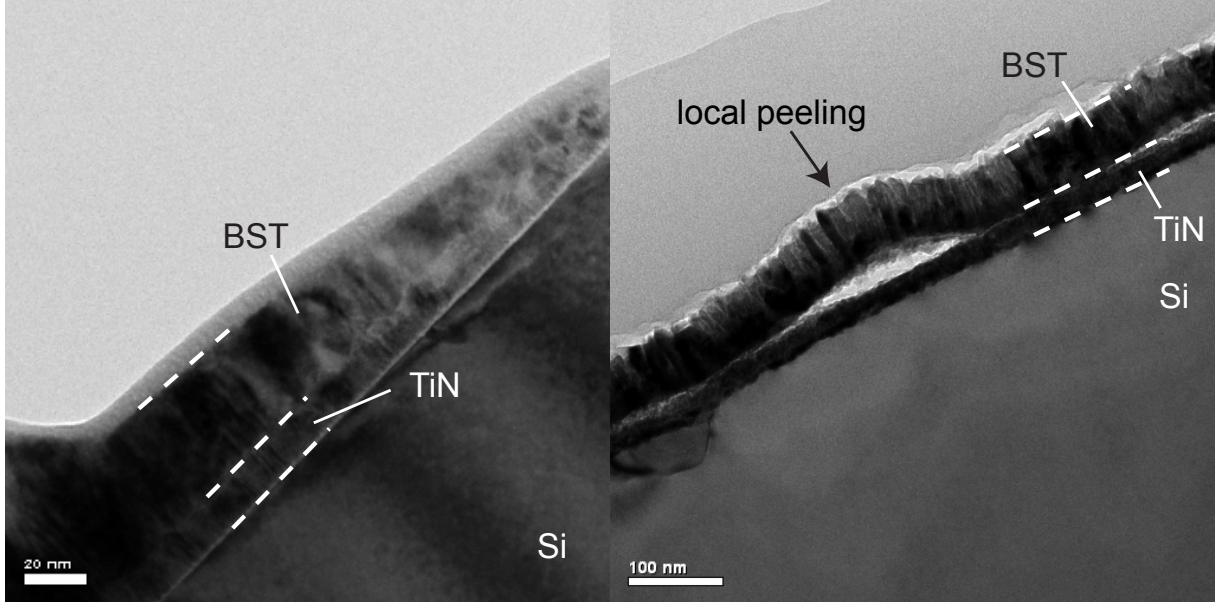
Figure 7.9: SEM images of the surface of BST thin films with epitaxial (a) and polycrystalline (b) structure. The epitaxial BST thin film shown in (a) was deposited at  $T=600\text{ }^{\circ}\text{C}$  and  $p(\text{O}_2) = 5 \times 10^{-4}$  Torr. The polycrystalline BST thin film shown in (b) was deposited at  $T=600\text{ }^{\circ}\text{C}$  and  $p(\text{O}_2) = 5 \times 10^{-2}$  Torr.

and  $p(\text{O}_2) = 5 \times 10^{-4}$  Torr and the polycrystalline BST thin film was deposited at  $T=600\text{ }^{\circ}\text{C}$  and  $p(\text{O}_2) = 5 \times 10^{-2}$  Torr. The surface of the epitaxial BST thin film was very smooth. No defects like pores, voids or cracks could be detected. The surface of the polycrystalline BST thin film was very rough. All over the samples bumps and voids of micrometer size were observed.

Figure 7.10 shows TEM cross sections of the epitaxial (Fig. 7.10a) and polycrystalline (Fig. 7.10b) BST thin film. The epitaxial thin film showed a coherent structure without any detectable defects. The interfaces between the different layers were smooth. The polycrystalline BST thin film showed localized peeling at the interface between the BST and the TiN layer. This localized peeling was observed as bumps on the surface of the film during the SEM investigation (see Fig. 7.9b). The localized peeling was observed all over the sample. We also found some reaction zones between the Si substrate and the TiN layer, but could not identify the nature of the phase. Chemical analysis of the TiN layer showed that there was some oxygen content which could not be quantified. The reaction zones at the TiN/Si interface might be due to a reaction of an oxidized TiN phase with the Si substrate [201].

We conclude that the deposition conditions for the polycrystalline BST thin film led to some oxidation of the TiN layer or, at least, of the surface of the TiN layer at the contact to the BST layer. The reaction between the TiN with  $\text{O}_2$  led to some outgassing of  $\text{N}_2$  according to the simplified reaction:





(a) Epitaxial BST thin film.

(b) Polycrystalline BST thin film.

Figure 7.10: TEM cross section images of BST thin films with epitaxial (a) and polycrystalline (b) structure. The epitaxial BST thin film shown in (a) was deposited at  $T=600\text{ }^{\circ}\text{C}$  and  $p(\text{O}_2) = 5 \times 10^{-4}\text{ Torr}$ . The polycrystalline BST thin film shown in (b) was deposited at  $T=600\text{ }^{\circ}\text{C}$  and  $p(\text{O}_2) = 5 \times 10^{-2}\text{ Torr}$ .

The Gibbs free energy change of the reaction shown in Eq. 7.1 under standard conditions is  $-33.15\text{ kJ/mol}$  [202]. The outgassing of the  $\text{N}_2$  may have led to the localized peeling of the BST thin films as well as to the formation of voids in the BST thin film. Thus, we conclude that an excessive deposition temperature and/or oxygen pressure during the BST thin film growth led to the oxidation of the entire TiN layer or the interface between the TiN and the BST layers. The oxidation resulted in the formation of voids in the BST films and caused a localized peeling of the film. Due to the oxidation the lattice match between the TiN and the BST thin film became unfavorable for the epitaxial film growth and the BST thin films grew polycrystalline, but were still highly  $c$ -axis textured. At low deposition temperatures ( $T < 550\text{ }^{\circ}\text{C}$ ) the interface between the BST and the TiN layers is expected to be stable. Since no epitaxial BST thin film growth was observed under these conditions, we attribute the polycrystalline nature of the BST film to the low surface mobility of the atoms under these conditions. The surface mobility of the atoms could be increased by increasing the laser energy making the epitaxial film growth eventually possible at temperatures of less than  $550\text{ }^{\circ}\text{C}$ .

An XRD  $\phi$ -scan of an epitaxial BST/TiN/Si heterostructure is shown in Fig. 7.11. The diffraction peaks of the BST and the TiN phase coincide with the peaks of the Si

## 7. INTEGRATION OF EPITAXIAL BST THIN FILMS ON SILICON

---

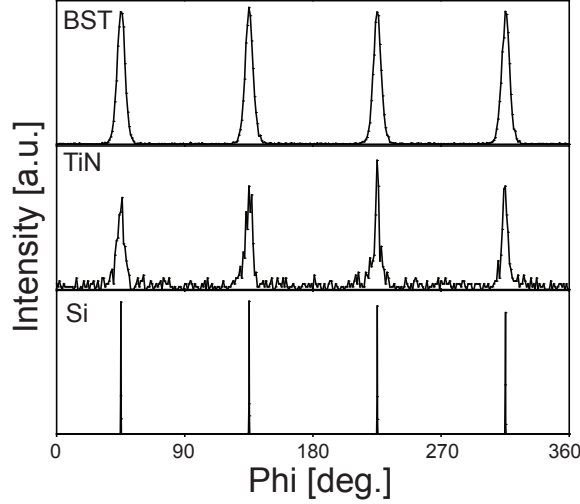


Figure 7.11: XRD  $\phi$ -scans around Si(hh0) for an epitaxial BST/TiN/Si heterostructure. The diffraction peaks of the BST and the TiN layer coincide with the peaks of the Si substrate indicating that the BST and the TiN films have the same in-plane orientation as the Si substrate.

substrate. Thus, we conclude that the BST and the TiN layer have the same in-plane orientation as the Si substrate. The in-plane and out-of-plane epitaxial relationship as found by means of XRD and RHEED analysis were:

- BST[100]||TiN[100]||Si[100]
- BST(001)||TiN(001)||Si(001)

The structural quality of the BST thin film was investigated by analyzing the FWHM of the rocking curve of the BST(002) diffraction peak. The FWHM of the rocking curve was  $2.2^\circ$  for the BST thin film deposited at  $T=600^\circ\text{C}$  and  $p(\text{O}_2) = 5 \times 10^{-4}$  Torr. As mentioned above, the growth conditions for the epitaxial BST thin films on TiN-buffered Si are rather limited. Therefore, we suggest that to improve the film quality an optimization of the laser conditions should be investigated. The results of the BST/TiN/Si structure are summarized in Tab. 7.1.

### Electrical characterization

Test capacitors based on the two heterostructures discussed above were electrically characterized. The performance of the devices was unsatisfactory. Potential reasons are discussed here.

For the BST / YBCO / CeO<sub>2</sub> / YSZ / Si heterostructure, we found the YBCO layer to be superconducting below temperatures of about 90 K before BST deposition. After the BST deposition, the electrical properties of the YBCO layer were degraded. A loss of the superconductivity and an apparent increase in the electrical resistivity at a given temperature were observed, which led to the deterioration of the capacitor performance. Potentially, there are two reasons for the observed degradation of the electrical properties of the YBCO layer. First, the BST deposition at an oxygen pressure of 0.050 Torr might have changed the oxygen concentration in the YBCO layer. Since the superconducting properties of the YBCO layer are very sensitive to the oxygen stoichiometry, a degradation of these properties might have been the result [203]. Post-annealing in air and or oxygen did not significantly improve the performance of the device and sometimes resulted in film cracking.

Second, some interdiffusion between the BST and the YBCO layer might have degraded the electrical properties of the YBCO layer. The YBCO layer was only 50 nm thick. A thicker layer could not be utilized because of film cracking. Film cracking occurred due to thermal stresses because of the large difference in the thermal expansion coefficient between Si and YBCO [203]. Since the YBCO layer is rather thin, some possible interdiffusion between BST and YBCO might have a large effect on the electrical performance of the YBCO layer.

The electrical properties of the BST/TiN/Si heterostructure were also found to be unsatisfactory. The capacitor based on this heterostructure showed a frequency dependence of the dielectric properties, which became more pronounced at higher temperatures, and it showed large dielectric losses under dc bias. The reasons for these observations might be associated with the performance of the BST and/or TiN layer. As discussed above, the deposition conditions for epitaxial BST on TiN-buffered Si are limited. In particular, the low oxygen pressures during the BST deposition might lead to oxygen vacancies in this layer. The oxygen vacancies can lead to an increase in the dc conduction of the BST layer [204]. This results in leakage currents under dc bias, which increases the loss tangent of the capacitor [204]. An oxygen or air anneal to reduce the number of oxygen vacancies in the BST layer would lead to an oxidation of the TiN layer and can therefore not be considered as a solution to the problem.

Another reason for the unsatisfactory electrical performance of the capacitor based on the BST/TiN/Si heterostructure might be associated with the electrical properties of the TiN layer. TiN is a good electrical conductor showing a low resistivity of about  $30 \pm 10 \mu\Omega\cdot\text{cm}$  for optimized films [205; 206]. The conductivity is strongly dependent on the stoichiometry and contamination of the films [206]. During BST deposition some, even small, amount of oxygen might have been incorporated into the TiN layer. This would strongly increase the resistivity of the TiN layer resulting in an unacceptable electrical performance of the device.

### 7.4 Summary and Conclusions

We investigated the possibilities to integrate epitaxial BST thin films on Si substrates. Two different electrode / buffer layer structures were investigated. Both structures, YBCO /  $\text{CeO}_2$  / YSZ / Si and TiN/Si, allowed the integration of epitaxial BST on Si.

The  $\text{CeO}_2$  and YSZ layers were grown with a cube-on-cube epitaxial relationship with respect to the substrate. The YBCO and BST layer were rotated in-plane by  $45^\circ$  with respect to the Si substrate. The different layers showed a good structural quality as indicated by the small FWHM of the corresponding rocking curves.

The BST and TiN films were grown with a cube-on-cube epitaxial relationship with respect to the substrate. The deposition conditions of the TiN layer were optimized to achieve a good structural quality. The conditions for epitaxial BST thin film growth on the optimized TiN layer was investigated. Epitaxial film growth was only observed in a narrow temperature and pressure range. At excessive deposition temperatures and/or pressures the oxidation of the TiN layer or of the BST/TiN interface occurred, which resulted in polycrystalline, but still highly (001) textured, BST film growth. The oxidation of the TiN layer probably led to an outgassing of  $\text{N}_2$  which resulted in the localized peeling of the BST thin film at the interface with the TiN layer. The structural quality of the epitaxial BST thin film needs further improvement, although the deposition conditions do not allow for great flexibility. The attempts for improving the structural quality should rather be focussed on optimization of other parameters like laser settings, for example.

The performance of capacitors based on the studied heterostructures exhibited unsatisfactory performance. Potential reasons are insufficient electrical properties of the TiN and YBCO electrodes as well as poor electrical properties of the BST layer due to the limited deposition conditions.

# Chapter 8

## Conclusions and outlook

This thesis addressed the integration of BST thin films on silicon substrates for tunable devices. A new type of tunable device, the tunable TFBAR, based on BST thin films has been realized. A theory of the electrical tuning of the dc bias induced acoustic resonances has been developed and successfully applied to model the tuning behavior of the fabricated TFBAR devices. Coplanar BST capacitors have been successfully implemented on Si. The use of micromachining technologies to remove parasitic effects improved the performance of these devices in comparison to non-micromachined devices. The integration of epitaxial BST thin films on silicon, being of potential interest for tunable capacitors and TFBARs, has been investigated.

We developed a theory describing the electrical tuning of dc bias induced acoustic resonances in paraelectric materials. The theory is based on the Landau free energy  $P$ -expansion and takes linear and non-linear electrostrictive effects as well as the background permittivity into account. The field dependent constitutive piezoelectric equations were derived first. With these equations we were able to model the tuning of the field induced acoustic resonances for two different excitation modes (TE and LFE modes), which correspond to two different resonator geometries. For the TE mode the theory predicts, in general, a stronger tuning of the resonance frequency in comparison to the antiresonance frequency. The resonance frequency always shifts to lower frequencies with increasing dc bias, whereas the antiresonance frequency can shift up or down with dc bias. For the LFE mode the antiresonance frequency shows a stronger tuning than the resonance frequency. Both frequencies can shift up, or down, or one up and one down depending on the sign and magnitude of the term  $\gamma_{lat}$ . Considering the case of high permittivity materials, we found that the dc-field induced electromechanical coupling factors and the relative tunability  $n_r$  exhibit the same dc electric field dependence. The derived equations for the tuning of the acoustic resonances in the two different geometries of excitation were used to illustrate the tuning behavior of resonators based on BST thin films, calculating the relevant parameters from literature data. It has been demonstrated that the adequate description of the field dependence of the induced acoustic resonances requires the con-

## 8. CONCLUSIONS AND OUTLOOK

---

stitutive equations derived from the  $P$ -expansion where the background permittivity and the nonlinear electrostriction (customarily neglected) are taken into account.

We successfully fabricated TFBARs based on BST thin films being in the paraelectric state. By applying a dc bias piezoelectricity is induced in the material. The device can therefore be switched on or off depending on whether the dc bias is applied or not. Due to the field dependent polarization  $P$  and permittivity  $\epsilon$  the resonance and antiresonance frequency could be tuned by the dc electric field. Both frequencies showed a tuning of -2.4% and -0.6%, respectively, at a dc electric field of 615 kV/cm. The tuning behavior was found to be non-hysteretic, which is an advantage over TFBARs based on tunable materials in the ferroelectric state. The  $k_{eff}^2$  increased up to 4.4% at the maximum dc electric field. The Q-factor of the device was about 200 and showed some variation with the dc bias. Parasitic resonances were observed under dc bias, especially under high fields in the real part of the impedance. The parasitic effects are most likely due to device design. A possible explanation might be laterally excited Lamb waves or the excitation of additional modes due to the in-series connection of two resonators. This issue remains a future task to be solved, in particular because the non-excitation of these parasitic resonances would enhance the performance of the devices.

The effect of mechanical loading on the tuning of the resonance and antiresonance frequencies of the BST TFBAR was addressed experimentally and theoretically. We found that an increase in the mechanical load reduces the tuning of the device. The reduction was explained by a reduction of the field dependence of  $k_{eff}^2$  and the sound velocity of the BST layer. The combination of experimental and theoretical work allowed us to extract the intrinsic tuning properties of a non-loaded BST layer. The tuning properties of the BST TFBAR with the smallest mechanical load we investigated, exhibited tuning characteristics close to the intrinsic properties of the BST layer. This means that the intrinsic field dependent electromechanical properties of the BST layer are efficiently used in this device. Our theory for the electrical tuning of dc bias induced acoustic resonances could be successfully applied to model the tuning behavior of the fabricated TFBARs. The parameters that could be measured in experiments were introduced in the model from the experimental data. The value of  $q$  was taken from literature data taking the (001)/(111) texture of our BST thin films into account. The modeling allowed the evaluation of the component of the tensor of non-linear electrostriction  $m$ . A value of  $m = 5 \times 10^{11}$  m/F gave the best fit to our data. This value is of the same order of magnitude than estimates from ab-initio calculations.

Coplanar capacitors were successfully fabricated on silicon. Micromachining technologies were used to remove the silicon substrate under the active area of the device reducing parasitic effects stemming from the substrate. The micromachined capacitor was compared to a non-micromachined capacitor. Both devices had the same device dimensions and the same BST film. The micromachined capacitor exhibited a higher tunability at lower capacitance and a lower loss tangent than the non-micromachined device. These results were interpreted in terms of reduced parasitic effects in the micromachined capaci-



---

tor. The micromachined capacitor had a tunability of 37% at  $E_{dc}=1100$  kV/cm. The loss tangent at 20 GHz was 0.08 and 0.06 at zero and maximum dc bias, respectively. The zero bias permittivity of the BST( $x=0.7$ ) thin film was 270 at room temperature. This low value of the permittivity indicates that the BST thin film was of poor quality. Improvement of the film quality should be considered in future work to improve the performance of the device. It would be interesting to compare the performance of a micromachined coplanar capacitor with that of a parallel-plate capacitor when both devices are based on BST thin films of comparable quality.

The integration of epitaxial BST thin films on silicon was investigated due to its potential importance for the improvement of the performance of tunable TFBARs and capacitors. Two different electrode/buffer layer structures were studied. With both structures (YBCO/CeO<sub>2</sub>/YSZ/Si and TiN/Si) epitaxial BST thin film growth was achieved. The CeO<sub>2</sub> and the YSZ layers were grown with a cube-on-cube epitaxial relationship on the silicon substrate. The YBCO and the BST layer showed a 45° rotation in the in-plane dimension in comparison to the substrate. All layers were purely c-axis aligned in the out-of-plane direction. The FWHM of the rocking curves of the BST, YBCO, and CeO<sub>2</sub> diffraction peaks were 0.5°, 0.4°, and 0.5°, respectively, indicating the good structural quality of the different layers.

The BST and the TiN layer were grown with a cube-on-cube epitaxial relationship on the Si substrate. First, the quality of the TiN layer was optimized. Best structural quality was achieved by depositing the layer under UHV conditions at high temperatures of 900 °C. The growth of epitaxial BST thin films on TiN-buffered Si was investigated by varying the deposition conditions in a wide temperature and pressure range. Epitaxial BST thin film growth was only possible under limited conditions of  $T=550$  to  $600$  °C and  $p(O_2) \leq 5 \times 10^{-4}$  Torr. At excessive deposition temperatures and/or oxygen pressures an oxidation of the TiN layer or the BST/TiN interface occurred, which resulted in polycrystalline, but still highly (001) textured, BST film growth. At too low deposition temperatures ( $T < 550$  °C) epitaxial BST thin film growth was also not possible, which can be explained by the low surface mobility of the atoms on the substrate surface. The oxidation of the TiN layer led to an outgassing of N<sub>2</sub>. This outgassing resulted in localized peeling of the BST layer on the interface with the TiN layer. The rocking curves FWHM of the BST and the TiN layer were 2.2° and 1.0°, respectively. To improve the structural quality of the BST layer further, the limitations of the deposition conditions do not offer great flexibility, so optimization of other parameters like laser settings should be considered.

Capacitors based on the two studied structures showed unsatisfactory performance. Potential reasons for these observation might be due to two factors. First, degraded electrical properties of the YBCO and TiN layers, which might be associated with the BST film deposition. Second, degraded electrical properties of the BST layer because of limitations in the deposition conditions. To improve the performance of the capacitors based on epitaxial BST thin films, the reasons for the degradation of the electrical properties of

## 8. CONCLUSIONS AND OUTLOOK

---

the YBCO layer during the BST deposition should be investigated. For the epitaxial BST film on TiN-buffered silicon an optimization of the laser parameters should be considered for the improvement of the structural quality of the BST film. Whether the electrical properties of the BST layer can be significantly improved, remains questionable because of the limited deposition conditions as mentioned above.

# Appendix A

## Calculation of relevant tensor components for BST thin films

The corresponding tensor components for the different BST compositions were calculated in virtual crystal approximation. Virtual crystal approximation is a method that assumes that the corresponding tensor components are linear functions of the composition between the end members of the solid solution. The values for  $q_{ij}$  for BST(x=0) and BST(x=1) were calculated as  $q_{ij} = Q_{ij}c_{ij}$  by taking the corresponding values for  $Q_{ij}$  and  $c_{ij}$  from Ref. [207], where  $Q_{ij}$  are the corresponding components of the tensor of linear electrostriction relating polarization to strain ( $u_{ij} = Q_{ijkl}P_kP_l$ ). The values of  $\beta_{ij}$  for BST(x=0) were taken from Ref. [208]. The values of  $\beta_{ij}$  for BST(x=1) were taken from Ref. [142] for T=298 K. To take the correct boundary conditions of mechanical clamping ( $u_{11} = u_{22} = u_{12} = u_{13} = u_{23} = 0$ ) into account the corresponding values of  $\beta_{ij}^\sigma$  for BST(x=0) and BST(x=1) were renormalized to  $\beta_{ij}^u$ , the values of the coefficients of dielectric non-linearity in the mixed mechanical boundary conditions typically occurring in thin films. The relations for the renormalization are given in Ref. [137].

The tensor components for different BST orientations were calculated by applying the corresponding transformation matrices of direction cosines which resulted in the following relations:

$$q_{33}^{(110)} = \frac{q_{33}}{2} + \frac{q_{31}}{2} + q_{44} \quad (\text{A.1})$$

$$q_{31}^{(110)} = \frac{q_{33}}{2} + \frac{q_{31}}{2} - q_{44} \quad (\text{A.2})$$

$$c_{33}^{(110)} = \frac{c_{33}}{2} + \frac{c_{31}}{2} + c_{44} \quad (\text{A.3})$$

## A. CALCULATION OF RELEVANT TENSOR COMPONENTS FOR BST THIN FILMS

---

$$\beta_{33}^{(110)} = \frac{\beta_{33}}{2} + \frac{\beta_{31}}{2} \quad (\text{A.4})$$

$$q_{33}^{(111)} = \frac{q_{33}}{3} + \frac{2q_{31}}{3} + \frac{4q_{44}}{3} \quad (\text{A.5})$$

$$q_{31}^{(111)} = \frac{q_{33}}{3} + \frac{2q_{31}}{3} - \frac{2q_{44}}{3} \quad (\text{A.6})$$

$$c_{33}^{(111)} = \frac{c_{33}}{3} + \frac{2c_{31}}{3} + \frac{4c_{44}}{3} \quad (\text{A.7})$$

$$\beta_{33}^{(111)} = \frac{\beta_{33}}{3} + \frac{2\beta_{31}}{3} \quad (\text{A.8})$$

When using Eqs. (A.4) and (A.8) to calculate the corresponding values of  $\beta_{ij}$  we neglect the impact of the elastic anisotropy on their renormalization.

# References

- [1] A. G. Fox. *Proceedings of the Institute of Radio Engineers*, 35:1489–1498, 1947.
- [2] F. Reggia et al. *Proceedings of the Institute of Radio Engineers*, 45:1510–1517, 1957.
- [3] R. K. Sorensen et al. *IEEE Microwave and Wireless Components Letters*, 14:25–27, 2004.
- [4] J. F. White. *IEEE Transactions on Microwave Theory and Techniques*, MT13:233, 1965.
- [5] A. Gopinath et al. *IEEE Transactions on Electron Devices*, 32:1272–1278, 1985.
- [6] J. J. Yao. *Journal of Micromechanics and Microengineering*, 10:R9–R38, 2000.
- [7] R. York et al. *Proceedings of the 12th IEEE International Symposium on Applications of Ferroelectrics*, 1:195–200, 2000.
- [8] X. X. Xi et al. *Journal of Electroceramics*, 4:393–405, 2000.
- [9] M. J. Lancaster et al. *Superconductor Science & Technology*, 11:1323–1334, 1998.
- [10] A. K. Tagantsev et al. *Journal of Electroceramics*, 11:5–66, 2003.
- [11] S. S. Gevorgian et al. *IEEE Transactions on Applied Superconductivity*, 7:2458–2461, 1997.
- [12] O. G. Vendik et al. *Journal of Superconductivity*, 12:325–338, 1999.
- [13] D. C. Dube et al. *Applied Physics Letters*, 74:3546–3548, 1999.
- [14] A. Vorobiev et al. *Applied Physics Letters*, 83:3144–3146, 2003.
- [15] S. Tappe et al. *Applied Physics Letters*, 85:624–626, 2004.
- [16] K. Morito et al. *Journal of Applied Physics*, 94:5199–5205, 2003.

## REFERENCES

---

- [17] S. Gevorgian et al. *Journal of Applied Physics*, 99:124112, 2006.
- [18] S. Gevorgian et al. Tuneable Resonator (Patent), Telefonaktiebolaget Lm Ericsson, United States Patent 20080055023, 2004.
- [19] G. A. Smolenskii et al. *Zhurnal Tekhnicheskoi Fiziki*, 24:1375–1386, 1954.
- [20] S. Ezhilvalavan et al. *Materials Chemistry and Physics*, 65:227–248, 2000.
- [21] A. Vorobiev et al. *Journal of Applied Physics*, 96:4642–4649, 2004.
- [22] J. Petzelt et al. *Physical Review B*, 64, 2001.
- [23] T. M. Shaw et al. *Applied Physics Letters*, 75:2129–2131, 1999.
- [24] C. B. Parker et al. *Applied Physics Letters*, 81:340–342, 2002.
- [25] Byoung Taek Lee et al. *Applied Physics Letters*, 77:124–126, 2000.
- [26] P. K. Larsen et al. *Journal of Applied Physics*, 76:2405–2413, 1994.
- [27] U. Ellerkmann et al. *Applied Physics Letters*, 85:4708–4710, 2004.
- [28] Hong-Cheng Li et al. *Applied Physics Letters*, 73:464–466, 1998.
- [29] L. J. Sinnamon et al. *Applied Physics Letters*, 78:1724–1726, 2001.
- [30] Sufi Zafar et al. *Applied Physics Letters*, 72:2820–2822, 1998.
- [31] C. Basceri et al. *Journal of Applied Physics*, 82:2497–2504, 1997.
- [32] C. T. Black et al. *IEEE Transactions on Electron Devices*, 46:776–780, 1999.
- [33] C. Zhou et al. *Journal of Applied Physics*, 82:3081–3088, 1997.
- [34] J. H. Haeni et al. *Nature*, 430:758–761, 2004.
- [35] N. A. Pertsev et al. *Journal of Applied Physics*, 85:1698–1701, 1999.
- [36] T. R. Taylor et al. *Applied Physics Letters*, 80:1978–1980, 2002.
- [37] A. Sharma et al. *Applied Physics Letters*, 85:985–987, 2004.
- [38] P. Padmini et al. *Applied Physics Letters*, 75:3186–3188, 1999.
- [39] X. H. Zhu et al. *Applied Physics A-Materials Science & Processing*, 80:591–595, 2005.

- [40] R. M. Waser. *Current Opinion in Solid State & Materials Science*, 1:706–714, 1996.
- [41] T. Hayashi et al. *Japanese Journal of Applied Physics Part 1-Regular Papers Short Notes & Review Papers*, 33:5277–5280, 1994.
- [42] D. Y. Noh et al. *Applied Physics Letters*, 72:2823–2825, 1998.
- [43] T. G. Kim et al. *Japanese Journal of Applied Physics Part 1-Regular Papers Short Notes & Review Papers*, 42:1315–1319, 2003.
- [44] X. H. Zhu et al. *Thin Solid Films*, 496:376–382, 2006.
- [45] M. C. Werner et al. *Applied Physics Letters*, 77:1209–1211, 2000.
- [46] R. Waser. *Integrated Ferroelectrics*, 15:39–51, 1997.
- [47] W. J. Lee et al. *Journal of Applied Physics*, 80:5891–5894, 1996.
- [48] T. Horikawa et al. *Japanese Journal of Applied Physics Part 1-Regular Papers Short Notes & Review Papers*, 32:4126–4130, 1993.
- [49] S. K. Streiffer et al. *Journal of Applied Physics*, 86:4565–4575, 1999.
- [50] S. Stemmer et al. *Applied Physics Letters*, 74:2432–2434, 1999.
- [51] S. Stemmer et al. *Interface Science*, 8:209–221, 2000.
- [52] S. Yamamichi et al. *Applied Physics Letters*, 64:1644–1646, 1994.
- [53] T. Kawahara et al. *Japanese Journal of Applied Physics Part 1-Regular Papers Short Notes & Review Papers*, 33:5129–5134, 1994.
- [54] C. Basceri et al. *Ferroelectric Thin Films VI*, 493:9–14, 1998.
- [55] Jaemo Im et al. *Applied Physics Letters*, 76:625–627, 2000.
- [56] B. S. Kang et al. *Applied Physics Letters*, 85:4702–4704, 2004.
- [57] T. Delage et al. *Thin Solid Films*, 453-454:279–284, 2004.
- [58] B. H. Park et al. *Applied Physics Letters*, 78:533–535, 2001.
- [59] C. L. Chen et al. *Integrated Ferroelectrics*, 42:165–172, 2002.
- [60] C. L. Canedy et al. *Applied Physics Letters*, 77:1695–1697, 2000.
- [61] W. K. Simon et al. *Journal of Applied Physics*, 97:103530–9, 2005.

## REFERENCES

---

- [62] W. T. Chang et al. *Integrated Ferroelectrics*, 77:173–187, 2005.
- [63] K. F. Astafiev et al. *Applied Physics Letters*, 84:2385–2387, 2004.
- [64] O. Nakagawara et al. *Journal of Applied Physics*, 78:7226–7230, 1995.
- [65] K. J. Hubbard et al. *Journal of Materials Research*, 11:2757–2776, 1996.
- [66] S. J. Jun et al. *Integrated Ferroelectrics*, 38:845–854, 2001.
- [67] Sungjin Jun et al. *Applied Physics Letters*, 78:2542–2544, 2001.
- [68] S. J. Jun et al. *Ferroelectrics*, 271:1611–1616, 2002.
- [69] M. N. K. Bhuiyan et al. *Applied Surface Science*, 216:590–595, 2003.
- [70] T. Tambo et al. *Japanese Journal of Applied Physics Part 1-Regular Papers Short Notes & Review Papers*, 37:4454–4459, 1998.
- [71] R. A. Mckee et al. *Applied Physics Letters*, 59:782–784, 1991.
- [72] Y. Z. Yoo et al. *Applied Physics Letters*, 82:4125–4127, 2003.
- [73] S. Xu et al. *Journal of Materials Science*, 33:1777–1782, 1998.
- [74] Tomoaki Yamada et al. *Applied Physics Letters*, 83:4815–4817, 2003.
- [75] M. Suzuki et al. *Materials Science and Engineering B*, 41:166–173, 1996.
- [76] R. Haakenaasen et al. *Applied Physics Letters*, 64:1573–1575, 1994.
- [77] C. A. Copetti et al. *Applied Physics Letters*, 63:1429–1431, 1993.
- [78] F. A. Miranda et al. *IEEE Transactions on Microwave Theory and Techniques*, 48:1181–1189, 2000.
- [79] J. RoldN et al. *Applied Surface Science*, 154-155:159–164, 2000.
- [80] T. Higuchi et al. *Japanese Journal of Applied Physics Part 2-Letters*, 41:L481–L483, 2002.
- [81] Y. J. Tian et al. *Journal of Superconductivity*, 11:713–717, 1998.
- [82] Naoki Wakiya et al. *Thin Solid Films*, 384:189–194, 2001.
- [83] Yu. A. Boikov et al. *Journal of Applied Physics*, 78:4591–4595, 1995.
- [84] J. Narayan et al. *Applied Physics Letters*, 61:1290–1292, 1992.



## REFERENCES

---

- [85] J. Narayan. *Metallurgical and Materials Transactions B-Process Metallurgy and Materials Processing Science*, 36:5–22, 2005.
- [86] J. Narayan et al. *Journal of Applied Physics*, 93:278–285, 2003.
- [87] R. D. Vispute et al. *Journal of Applied Physics*, 80:6720–6724, 1996.
- [88] W. B. Wu et al. *Thin Solid Films*, 360:103–106, 2000.
- [89] A. Tombak et al. *IEEE Transactions on Microwave Theory and Techniques*, 51:462–467, 2003.
- [90] A. Kozyrev et al. *Integrated Ferroelectrics*, 55:905–913, 2003.
- [91] A. Victor et al. *Proceedings IEEE Radio and Wireless Conference Rawcon: 2004*, pages 91–94, 2004.
- [92] B. Acikel et al. *IEEE Microwave and Wireless Components Letters*, 12:237–239, 2002.
- [93] R. E. Newnham et al. *Journal of Physical Chemistry B*, 101:10141–10150, 1997.
- [94] J. Kuwata et al. *Japanese Journal of Applied Physics*, 19:2099–2103, 1980.
- [95] D. Damjanovic. *Reports on Progress in Physics*, 61:1267–1324, 1998.
- [96] K. M. Lakin. *IEEE Transactions on Ultrasonics, Ferroelectrics and Frequency Control*, 52:707–716, 2005.
- [97] Y Satoh. *Japanese Journal of Applied Physics*, 44:2883–2894, 2005.
- [98] H. P. Loeb1 et al. *Materials Chemistry and Physics*, 79:143–146, 2003.
- [99] G. Ferblantier et al. *Sensors and Actuators A-Physical*, 122:184–188, 2005.
- [100] C. Zinck et al. *14th IEEE International Symposium on Applications of Ferroelectrics*, pages 29–32, 2004.
- [101] Q. X. Su et al. *IEEE Transactions on Microwave Theory and Techniques*, 49:769–778, 2001.
- [102] J. D. Larson et al. *Proceedings IEEE Ultrasonics Symposium 2004*, 1–3:173–177, 2004.
- [103] P. Muralt et al. *IEEE Ultrasonics Symposium 2005*, 1:315–320, 2005.
- [104] K. M. Lakin. *Proceedings IEEE Ultrasonics Symposium 1999*, 2:895–906, 1999.

## REFERENCES

---

- [105] H. Zhang et al. *Journal of Microelectromechanical Systems*, 14:699–706, 2005.
- [106] H. Zhang et al. *The 13th International Conference on Solid-State Sensors, Actuators and Microsystems 2005*, 1:1100–1101, 2005.
- [107] R. Gabl et al. *Proceedings IEEE Sensors 2003*, pages 1184–1188, 2003.
- [108] S. Horwitz et al. *IEEE Mtt-S International Microwave Symposium Digest 1992*, pages 165–168, 1992.
- [109] K. M. Lakin et al. *Proceedings IEEE Ultrasonics Symposium 1992*, 1:471–476, 1992.
- [110] K. M. Lakin et al. *IEEE Transactions on Microwave Theory and Techniques*, 41:2139–2146, 1993.
- [111] P. Bradley et al. *2001 IEEE Mtt-S International Microwave Symposium Digest*, 1-3:367–370, 2001.
- [112] R. C. Ruby et al. *IEEE Ultrasonics Symposium 2001*, 1:813–821, 2001.
- [113] J. D. Larson et al. *Proceedings IEEE Ultrasonics Symposium 1999*, pages 887–890, 1999.
- [114] H. Lakdawala et al. *Proceedings IEEE International Frequency Control Symposium 1998*, pages 831–835, 1998.
- [115] W. Pang et al. *Proceedings of the 2004 IEEE International Frequency Control Symposium and Exposition*, pages 22–26, 2005.
- [116] R. Ruby et al. *Proceedings 48th IEEE International Frequency Control Symposium 1994*, pages 135–138, 1994.
- [117] H. M. Lee et al. *Japanese Journal of Applied Physics Part 2-Letters*, 43:L85–L87, 2004.
- [118] R. Aigner et al. *IEEE Mtt-S International Microwave Symposium Digest 2005*, page 4, 2005.
- [119] Jong Jin Kim et al. *The 13th International Conference on Solid-State Sensors, Actuators and Microsystems 2005*, 1:1063–1066, 2005.
- [120] J. D. Jorgenson et al. Thin-film bulk acoustic resonator manufacturing method for wireless system, involves changing reactive tuning element connected to FBAR, to tune FBAR to desired resonant frequency (Patent), RF Micro Devices Inc, US2004014249-A1; US7101721-B2, 2002.

- 
- [121] Wanling Pan et al. *IEEE Ultrasonics Symposium 2005*, 3:1840–1843, 2005.
- [122] Roman Lanz. *Piezoelectric Thin Films for Bulk Wave Acoustic Resonator Applications: From Processing to Microwave Filters*. PhD thesis, Ecole Polytechnique Federale de Lausanne (EPFL), 2004.
- [123] W. Pang et al. *IEEE Mtt-S International Microwave Symposium 2005*, 1–4:1279–1282, 2005.
- [124] M. A. Dubois et al. *Applied Physics Letters*, 74:3032–3034, 1999.
- [125] J. Y. Park et al. *Microwave and Optical Technology Letters*, 48:2230–2233, 2006.
- [126] Z. Yan et al. *Applied Physics Letters*, 90:143503, 2007.
- [127] E. G. Erker et al. *IEEE Microwave and Guided Wave Letters*, 10:10–12, 2000.
- [128] T. Suzuki et al. *Integrated Ferroelectrics*, 76:47–57, 2005.
- [129] A. Vorobiev et al. *Thin Solid Films*, 515:6606–6610, 2007.
- [130] J. M. Pond et al. *Integrated Ferroelectrics*, 22:317–328, 1998.
- [131] O. G. Vendik et al. *Technical Physics Letters*, 25:702–704, 1999.
- [132] G. N. Saddik et al. *Applied Physics Letters*, 91:043501, 2007.
- [133] J. Berge et al. *IEEE Microwave and Wireless Components Letters*, 17:655–657, 2007.
- [134] X. Zhu et al. *IEEE/Mtt-S International Microwave Symposium 2007*, pages 671–674, 2007.
- [135] Irina B. Vendik et al. *Journal of Applied Physics*, 103:014107–6, 2008.
- [136] J. Hlinka et al. *Physical Review B*, 74:104104, 2006.
- [137] N. A. Pertsev et al. *Physical Review Letters*, 80:1988–1991, 1998.
- [138] A. K. Tagantsev et al. *Physical Review B*, 65:012104, 2002.
- [139] J. F. Rosenbaum. *Bulk Acoustic Wave Theory and Devices*. Artech House, Inc., 1988.
- [140] Guido Gerra. *Private communication*.
- [141] Y. L. Wang et al. *Physical Review B*, 73:132103, 2006.

## REFERENCES

---

- [142] Y. L. Wang et al. *Journal of Applied Physics*, 101:104115, 2007.
- [143] A. Noeth et al. *Journal of Applied Physics*, 102:114110, 2007.
- [144] V. G. Vaks. *Soviet Physics Jetp-Ussr*, 27:486, 1968.
- [145] D. B. Chrissey et al. *Pulsed Laser Deposition of Thin Films*. Wiley, New York, 1994.
- [146] T J Jackson et al. *Journal of Physics D: Applied Physics*, 27:1581–1594, 1994.
- [147] D. Dijkkamp et al. *Applied Physics Letters*, 51:619–621, 1987.
- [148] P. R. Willmott. *Progress in Surface Science*, 76:163–217, 2004.
- [149] R Ramesh et al. *Annual Review of Materials Science*, 25, 1995.
- [150] P. R. Willmott et al. *Rev. Mod. Phys.*, 72:315–328, 2000.
- [151] R. W. Dreyfus. *Journal of Applied Physics*, 69:1721–1729, 1991.
- [152] L. Wiedeman et al. *Journal of Applied Physics*, 70:4513–4523, 1991.
- [153] I. Weaver et al. *Journal of Applied Physics*, 79:7216–7222, 1996.
- [154] X. W. Sun et al. *Applied Physics Letters*, 68:2663–2665, 1996.
- [155] M. Kim et al. *Physica Status Solidi-Rapid Research Letters*, 2:13–15, 2008.
- [156] M. Yeadon et al. *Journal of Crystal Growth*, 172:145–155, 1997.
- [157] Y. Fukuda et al. *Japanese Journal of Applied Physics Part 2-Letters*, 36:L1514–L1516, 1997.
- [158] Z Ma. *IEEE Transactions on Electron Devices*, 45:1811–1816, 1998.
- [159] W. J. Lee et al. *Japanese Journal of Applied Physics Part 1-Regular Papers Short Notes & Review Papers*, 34:196–199, 1995.
- [160] Sean P. Keane et al. *Journal of Applied Physics*, 99:033521–10, 2006.
- [161] Guido W. Dietz et al. *Journal of Applied Physics*, 78:6113–6121, 1995.
- [162] J. Weber et al. *Sensors and Actuators A-Physical*, 128:84–88, 2006.
- [163] S. Rey-Mermet et al. *Sensors and Actuators B-Chemical*, 114:681–686, 2006.
- [164] B. P. Otis et al. *IEEE Journal of Solid-State Circuits*, 38:1271–1274, 2003.

## REFERENCES

---

- [165] K. Wang et al. *Proceedings IEEE Ultrasonics Symposium 2002*, 1:925–929, 2002.
- [166] T. Nishihara et al. *Proceedings IEEE Ultrasonics Symposium 2002*, 1:969–972, 2002.
- [167] R. Lanz et al. *IEEE Ultrasonics Symposium 2006*, pages 1481–1485, 2006.
- [168] Wei Pang et al. *Journal of Microelectromechanical Systems*, 16:1303–1313, 2007.
- [169] P. Bao et al. *Journal of Physics D-Applied Physics*, 41:063001, 2008.
- [170] Dongsu Kim et al. *IEEE Transactions on Microwave Theory and Techniques*, 50:2903–2909, 2002.
- [171] A. Noeth et al. *IEEE Transactions on Ultrasonics Ferroelectrics and Frequency Control*, 54:2487–2492, 2007.
- [172] F. Laermer et al. Process for anisotropic etching of structures in a semiconductor body comprises applying ion acceleration voltage between the plasma and the semiconductor body via an etching step lasting a prescribed period of time (Patent), Robert Bosch GmbH, DIIDW:2001017302, 2001.
- [173] Q. M. Wang et al. *Sensors and Actuators A-Physical*, 109:149–155, 2003.
- [174] J. Kaitila. *IEEE Ultrasonics Symposium 2007*, pages 120–129, 2007.
- [175] Tapani Makkonen. *Numerical Simulations of Microacoustic Resonators and Filters*. PhD thesis, Helsinki University of Technology, 2005.
- [176] J. Kaitila et al. *IEEE Ultrasonics Symposium 2003*, 1:84–87, 2003.
- [177] J. Conde et al. *IEEE Transactions on Ultrasonics, Ferroelectrics and Frequency Control*, 55:1373–1379, 2008.
- [178] M. Schreiter et al. *Journal of the European Ceramic Society*, 24:1589–1592, 2004.
- [179] A. Noeth et al. *submitted to Journal of Applied Physics*, 2008.
- [180] A. Devos et al. *Applied Physics Letters*, 86:211903, 2005.
- [181] Olaf Zywitzki et al. *Surface and Coatings Technology*, 133-134:555–560, 2000.
- [182] Jr. M. W. Chase. *NIST-JANAF Thermochemical Tables*. J. Phys. Chem. Ref. Data, Monograph 9, 1998.
- [183] P. S. Manning et al. *Solid State Ionics*, 100:1–10, 1997.
- [184] M. Kilo et al. *Physical Chemistry Chemical Physics*, 5:2219–2224, 2003.

## REFERENCES

---

- [185] G. Knoner et al. *Proceedings of the National Academy of Sciences of the United States of America*, 100:3870–3873, 2003.
- [186] J. D. Baniecki et al. *Applied Physics Letters*, 72:498–500, 1998.
- [187] Wen-An Lan et al. *Applied Physics Letters*, 89:022910–3, 2006.
- [188] Tae-In Jeon et al. *Physical Review Letters*, 78, 1997.
- [189] Tae-In Jeon et al. *Applied Physics Letters*, 72:2259–2261, 1998.
- [190] D. Lederer et al. *Proceedings IEEE International SOI Conference 2003*, pages 50–51, 2003.
- [191] Yunhong Wu et al. *Microwave and Guided Wave Letters, IEEE*, 9:10–12, 1999.
- [192] O. G. Vendik et al. *Technical Physics*, 44:349–355, 1999.
- [193] M. Izuha et al. *Japanese Journal of Applied Physics Part 1-Regular Papers Short Notes & Review Papers*, 36:5866–5869, 1997.
- [194] M. Izuha et al. *Solid State Ionics*, 108:99–104, 1998.
- [195] J. Bjurstrom et al. *IEEE Transactions on Ultrasonics Ferroelectrics and Frequency Control*, 51:1347–1353, 2004.
- [196] A. Bardal et al. *Journal of Applied Physics*, 75:2902–2910, 1994.
- [197] D. K. Fork et al. *Applied Physics Letters*, 57:1137–1139, 1990.
- [198] J. D. Suh et al. *Physica C*, 235:571–572, 1994.
- [199] J. Borck et al. *Physica C*, 213:145–150, 1993.
- [200] V. Boffa et al. *Physica C*, 276:218–224, 1997.
- [201] L. Q. Zhu et al. *Applied Physics Letters*, 91:172902–3, 2007.
- [202] M. Wittmer et al. *Journal of Applied Physics*, 52:6659–6664, 1981.
- [203] J. M. Qiao et al. *Materials Science & Engineering R-Reports*, 14:157–201, 1995.
- [204] Seong-Goo Kim et al. *Materials Letters*, 43:254–258, 2000.
- [205] H. Zafer Durusoy et al. *Vacuum*, 70:21–28, 2003.
- [206] N. Savvides et al. *Journal of Applied Physics*, 64:225–234, 1988.

## REFERENCES

---

- [207] Landolt-Börnstein. *Numerical Data and Functional Relationships in Science and Technology*. Springer, New York, 1981.
- [208] G. Rupprecht et al. *Physical Review*, 1:97, 1961.





# Curriculum vitae

**Andreas Nöth**

Date and place of birth: 11.October 1978 in Hammelburg (GER)

Nationality: German

---

## EMPLOYMENT

06/2005 - present	<b>EPF Lausanne, Ceramics Laboratory</b> (Switzerland) <ul style="list-style-type: none"><li>• Research assistant and PhD student</li></ul>
11/2004 - 05/2005	<b>Fraunhofer Institute for Silicate Research</b> (Germany) <ul style="list-style-type: none"><li>• Research assistant</li></ul>
08/2003 - 11/2003	<b>Schott AG</b> (Germany) <ul style="list-style-type: none"><li>• Internship</li></ul>
04/2003 - 06/2003	<b>Interdisciplinary Research Center in Materials Processing</b> (United Kingdom) <ul style="list-style-type: none"><li>• Internship</li></ul>
08/1998 - 09/1999	<b>Carl-von-Hess Hospital Hammelburg</b> (Germany) <ul style="list-style-type: none"><li>• Social services</li></ul>

## EDUCATION

11/1999 - 11/2004	<b>Julius-Maximilians Universität Würzburg</b> (Germany) <ul style="list-style-type: none"><li>• degree: Diploma in Mineralogy</li></ul>
11/1988 - 06/1998	<b>Frobenius-Gymnasium Hammelburg</b> (Germany) <ul style="list-style-type: none"><li>• degree: Abitur</li></ul>

## List of publications

- A. Noeth, T. Yamada, P. Muralt, A. K. Tagantsev, and N. Setter: “Tunable Thin Film Bulk Acoustic Wave Resonator based on  $\text{Ba}_x\text{Sr}_{1-x}\text{TiO}_3$  thin film”, IEEE Transactions on Ultrasonics, Ferroelectrics and Frequency Control, submitted.
- A. Noeth, T. Yamada, A. K. Tagantsev, and N. Setter: “Effect of mechanical loading on the tuning of acoustic resonances in  $\text{Ba}_x\text{Sr}_{1-x}\text{TiO}_3$  thin films”, Journal of Electroceramics, accepted.
- A. Noeth, T. Yamada, A. K. Tagantsev, and N. Setter: “Electrical tuning of dc bias induced acoustic resonances in paraelectric thin films”, Journal of Applied Physics, 104, 094102 (2008).
- A. Noeth, T. Yamada, V. O. Sherman, P. Muralt, A. K. Tagantsev, and N. Setter: “Tuning of direct current bias-induced resonances in micromachined  $\text{Ba}_{0.3}\text{Sr}_{0.7}\text{TiO}_3$  thin-film capacitors”, Journal of Applied Physics 102, 114110 (2007).
- A. Noeth, T. Yamada, V. O. Sherman, P. Muralt, A. K. Tagantsev, and N. Setter: “DC bias-dependent shift of the resonance frequencies in BST thin film membranes”, IEEE Transactions on Ultrasonics, Ferroelectrics and Frequency Control 54, 2487 (2007).
- A. Noeth, T. Yamada, V. O. Sherman, P. Muralt, A. K. Tagantsev, and N. Setter: “DC bias-dependent shift of the resonance frequencies in BST thin film membranes”, Proc. IEEE 16th International Symposium on the Applications of Ferroelectrics, 236 (2007).
- T. Yamada, V. O. Sherman, A. Nöth, P. Muralt, A. K. Tagantsev, N. Setter: “Epitaxial/amorphous  $\text{Ba}_{0.3}\text{Sr}_{0.7}\text{TiO}_3$  Film Composite Structure for Tunable Application”, Applied Physics Letters, 032905 (2006).
- T. Yamada, V.O. Sherman, A. Nöth, P. Muralt, A.K. Tagantsev, and N. Setter: “Self-selective Epitaxial Growth of BST Films: toward Nanocomposite Structure for Microwave Tunable Device”, Mater. Res. Soc. Symp. Proc., 928, 0928-GG01-03 (2006).
- T. Yamada, V.O. Sherman, A. Nöth, P. Muralt, A.K. Tagantsev, and N. Setter: “Tunable Ferroelectric Thin Films with Enhanced Responses through Nano-structural Control”, Proc. IEEE 16th International Symposium on the Applications of Ferroelectrics, 29B-TF6-I1 (2007).

- V.O. Sherman, T. Yamada, A. Nöth, N. Setter, M. Mandeljc, B. Malic, M. Kosec, and M. Vukadinovic: “Microwave Phase Shifters Based on Sol- Gel Derived  $\text{Ba}_{0.3}\text{Sr}_{0.7}\text{TiO}_3$  Ferroelectric Thin Films”, Proc. of 37th European Microwave Conference 1295-1298 (2007).
- T. Yamada, C.S. Sandu, V.O. Sherman, A. Nöth, P. Muralt, A.K. Tagantsev, and N. Setter: “Self-Assembled Perovskite-Fluorite Oblique Nanostructures for Adaptive (Tunable) Electronics”, Advanced Materials (2007), in press.

